Universität Münster

Alexander Marco Tiekötter

Investigating J/ψ production as a function of multiplicity in pp collisions at $\sqrt{s} = 13.6$ TeV

2025

living.knowledge



Investigating J/ψ production as a function of multiplicity in pp collisions at $\sqrt{s} = 13.6$ TeV

Master thesis
submitted to the

University of Münster
Institute for Nuclear Physics

by
Alexander Marco Tiekötter

July 2025

First examiner:	Anton Andronic
Second examiner:	Christian Klein-Bösing
Day of submission:	Friday 11th July, 2025

Abstract

Quantum Chromodynamics (QCD) processes both involve hard- and soft-scale components. Investigating the interplay between these processes can lead to interesting new insights on particle production and strengthen the understanding of the strong interaction. One way to do so is to analyze the production of charmonium, which is primarily driven by hard-scale perturbative Quantum Chromodynamics (pQCD) processes as a function of the charged-particle multiplicity, which originates primarily from soft processes. High multiplicity proton-proton collisions are of particular interest, because of the increased chances for mechanisms like multi-parton interactions and saturation effects to occur, which may be linked to the emergence of collective behavior in small system collisions.

This thesis aims to contribute to the research effort made in this direction by investigating the self-normalized inclusive J/ψ yield at mid-rapidity as a function of the self-normalized charged-particle multiplicity in $|\eta| < 0.8$ with the A Large Ion Collider Experiment (ALICE) at the Large Hadron Collider (LHC). The analysis was performed in pp collisions at $\sqrt{s} = 13.6\,\mathrm{TeV}$ for a p_{T} integrated J/ψ production as well as J/ψ with low-, mid-, and high transverse momentum. The multiplicity was estimated using two different track-types: Global tracks and Primary Vertex (PV) contributors.

A stronger-than-linear increase of the self-normalized J/ψ yield with the self-normalized charged-particle multiplicity was observed for both estimators in all selected bins of the transverse momentum. With increasing p_{T}, the slope of the stronger-than-linear becomes larger. All results are qualitatively in agreement with measurements from previous experiments and theoretical model predictions.

Zusammenfassung

Prozesse der Quantenchromodynamik (QCD) beinhalten sowohl Komponenten auf harten als auch auf weichen Skalen. Die Untersuchung des Zusammenspiels dieser Prozesse kann zu neuen, aufschlussreichen Erkenntnissen über die Teilchenproduktion führen und das Verständnis der starken Wechselwirkung vertiefen. Eine Möglichkeit, dieses Zusammenspiel zu analysieren, besteht in der Untersuchung der Produktion von Quarkonium, welche hauptsächlich durch harte Prozesse der perturbativen QCD (pQCD) dominiert wird, in Abhängigkeit von der geladenen Teilchenmultiplizität, die primär aus weichen Prozessen hervorgeht. Insbesondere Proton-Proton-Kollisionen mit vielen erzeugten Teilchen sind von Interesse, da in diesen vermehrt Mechanismen wie Multi-Parton-Wechselwirkungen und Sättigungseffekte auftreten können, die möglicherweise mit dem Auftreten kollektiven Verhaltens in Kollisionen kleiner Systeme in Verbindung stehen.
Diese Arbeit leistet einen Beitrag zu den laufenden Forschungsbemühungen in diesem Bereich durch die Untersuchung der selbst-normalisierten, inklusiven J/ψ-Erzeugung bei mittlerer Rapidität als Funktion der selbst-normalisierten geladenen Teilchenmultiplizität in $|\eta| < 0,8$ mit dem ALICE-Experiment am LHC. Die Analyse wurde für Proton-Proton-Kollisionen bei $\sqrt{s} = 13.6\,\mathrm{TeV}$ sowohl für die p_T-integrierte J/ψ-Produktion als auch für J/ψ mit niedrigem, mittlerem und hohem transversalem Impuls durchgeführt. Die Multiplizität wurde mittels zweier verschiedener Track-Typen bestimmt: Global tracks und PV contributor.
Für beide Track-Typen wurde in allen gewählten p_T-Intervallen ein nicht-linearer Anstieg des selbst-normalisierten J/ψ-Ertrags mit der selbst-normalisierten geladenen Teilchenmultiplizität beobachtet. Mit zunehmendem p_T nimmt die Steigung dieses Anstiegs weiter zu. Alle Ergebnisse stehen qualitativ im Einklang mit Messungen vorheriger Experimente sowie mit theoretischen Modellvorhersagen.

Acknowledgement

I would like to use this opportunity to thank everyone that supported me throughout this thesis. I am very grateful to Prof. Anton Andronic and Prof. Christian Klein-Bösing for the opportunity to work in their research group on such an interesting topic and for all the assistance they provided me.
I would also like to thank the members of the research group at the Institute for Nuclear Physics at the University of Münster for all the support, fruitful discussions a very enjoyable work atmosphere. In particular, I want to thank Gauthier Legras, Tabea Eder, Archita Dash, and Yuan Zhang for their time to answer my questions and their advices. Furthermore, I want to thank Prof. Zebo Tang for the opportunity to work in his group during the international summer research program at the University of Science and Technology of China.
Finally, I would like to thank my parents, Heike Tiekötter and Marco Tiekötter, for the ongoing emotional and financial support during my whole study, without that I would not have been able to accomplish this work.

List of abbreviations

SM Standard Model

EM Electromagnetic

QFT Quantum Field Theory

QED Quantum Electrodynamics

QCD Quantum Chromodynamics

pQCD perturbative Quantum Chromodynamics

lQCD lattice Quantum Chromodynamics

QGP Quark-Gluon-Plasma

EFT Effective Field Theory

ALICE A Large Ion Collider Experiment

CERN European Organization for Nuclear Research

RHIC Relativistic Heavy Ion Collider

PS Proton Synchroton

SPS Super Proton Synchroton

FAIR Facility for Antiproton and Ion Research

CBM Compressed Baryonic Matter

LHC Large Hadron Collider

PDF Parton Distribution Functions

DIS Deep Inelastic Scattering

SLAC Stanford Linear Accelerator Center

NRQCD Non-Relativistic Quantum Chromodynamics

NLO next-to-leading order

CEM Color Evaporation Model

ICEM Improved Color Evaporation Model

CSM Color Singlet Model

LDME long-distance matrix element

CGC Color Glass Condensate

BSM Beyond Standard Model

PDG Particle Data Group

LEP Large Electron-Positron Collider

MPI Multi-Parton Interaction

CR Color Reconnection

OZI Okubo-Zweig-Iizuka

ATLAS A Toroidal LHC Apparatus

CMS Compact Muon Solenoid

LHCb Large Hadron Collider beauty

TOTEM Total Elastic and diffractive cross section measurement

LHCf Large Hadron Collider forward

MoEDAL Monopole and Exotics Detector at the LHC

ITS Inner Tracking System

SPD Silicon Pixel Detector

TPC Time Projection Chamber

TRD Transition Radiation Detector

TOF Time-of-flight Detector

EMCal Electromagnetic Calorimeter

PHOS Photon Spectrometer

DCal Di-jet Calorimeter

HMPID High Momentum Particle Identification

FIT	Fast Interaction Trigger
ZDC	Zero Degree Calorimeter
AD	ALICE Diffractive Detector
MCH	Muon Tracking Chamber
MFT	Muon Forward Tracker
MID	Muon Identifier
PID	Particle Identification
ACORDE	ALICE Cosmic Rays Detector
MAP	Monolithic Active Pixel Sensor
IB	Inner Barrel
OB	Outer Barrel
PV	Primary Vertex
GEM	Gas Electron Multiplier
FEC	Front-End Cards
MRPC	Multigap Resistive Plate Chamber
FLP	First-level processor
HBF	Heart Beat Frame
STF	Sub-Time Frame
TF	Time Frame
ROF	Read-out Frame
BC	Bunch Crossing
PWG	Physics Working Group
PAG	Physics Analysis Group
MC	Monte Carlo
DQ	Di-Quark
MB	Minimum Bias
DCA	Distance of Closest Approach

Contents

1 Introduction **1**

2 Theoretical Background **3**
2.1 The Standard Model . . . 3
2.2 Quantum Chromodynamics . . . 5
2.3 Hadron-Hadron Collisions . . . 8
2.4 Quark-Gluon-Plasma . . . 11
2.5 Interaction of Charged Particles with Matter . . . 16

3 Charmonium Production in Proton-Proton Collisions **19**
3.1 Prompt and Non-Prompt Charmonium Production . . . 19
3.2 Theoretical Models of the Multiplicity Dependence . . . 23
3.3 Experimental Status of Charmonium Production as a Function of Multiplicity . . . 29

4 Experimental Setup and Methods **31**
4.1 The Large Hadron Collider . . . 31
4.2 A Large Ion Collider Experiment . . . 32
4.2.1 Inner Tracking System . . . 33
4.2.2 Time Projection Chamber . . . 34
4.2.3 Time-of-Flight Detector . . . 34
4.2.4 Fast Interaction Trigger . . . 35
4.3 Tracking and Vertex Reconstruction . . . 35
4.4 Track to Collision Association . . . 36
4.5 Particle Identification . . . 38
4.6 Analysis Software . . . 39

5 Analysis of Multiplicity Dependence of J/ψ Production **41**
5.1 Analysis Strategy . . . 41
5.2 Event Selection Criteria . . . 44
5.3 Track Selection Criteria . . . 50
5.4 Event-Level Corrections . . . 51
5.5 Multiplicity Estimation . . . 52
5.5.1 Estimator Distributions . . . 52

5.5.2 Bayesian Unfolding of Spectra 56
5.5.3 Distributions in Multiplicity Bins 57
5.6 J/ψ Signal Extraction 60
5.6.1 Electron Selection Cuts 62
5.6.2 Invariant Mass Distributions 64
5.6.3 Statistical Uncertainties 68

6 Results **71**
6.1 Inclusive J/ψ Production versus Charged Particle Multiplicity 71
6.2 Comparison with previously published Results 74
6.3 Comparison with Theoretical Models 77

7 Summary and Outlook **79**

A Appendix **81**
A.1 Track Selection Criteria Distributions 81
A.2 Track-to-Particle Correlations for different $n\sigma$ 82
A.3 Independent Event Cut Efficiencies 83
A.4 Global Track Invariant Mass Distributions 84
A.5 PV Contributors Invariant Mass Distributions 92
A.6 Results for Different Production Years 100

Bibliography **101**

1 Introduction

Under extreme conditions, matter is no longer confined to hadrons but instead transitions into a loosely bound collection of quasi-free quarks and gluons, called the Quark-Gluon-Plasma (QGP). In the early moments of the Big Bang, the universe was sufficiently hot and dense for a brief period to exist entirely in this QGP phase. Today, only cores of super-dense neutron stars naturally produce such state of matter.

On earth, humanity can reproduce a QGP with the help of particle accelerators like the LHC and specialized experiments like ALICE by colliding heavy nuclei. However, it is yet unknown whether the QGP may also be created in smaller collision systems, which is a key open question in today's research of the strong interaction.

Earlier studies revealed that in high-multiplicity proton-proton collisions, effects appear that may be attributed to a QGP. Such collisions at LHC energies reach amounts of produced particles that are comparable to less central Pb–Pb collisions. They are associated with the appearance of multiple hard and soft scatterings within a single collision, called Multi-Parton Interaction (MPI). Thus, a dense partonic environment is created that enables the possibility of Color Reconnection (CR) that reflect QGP-like recombinations in dense pp collisions. A promising probe for investigations related to this is the study of the self-normalized J/ψ yield as a function of the self-normalized charged-particle multiplicity. This observable depends on the hard perturbative production mechanisms of the $c\bar{c}$ states as well as the soft-scale hadronization mechanisms, allowing for the study of the interplay between the two scales and may help to disentangle whether the QGP formation is driven by multiplicity or the collision system itself. Measurements performed by several collaborations like ALICE, **PHENIX**, and **STAR** demonstrated a stronger-than-linear increase of the J/ψ yield with multiplicity when both observables were measured in the same rapidity region. It was found that the increase is stronger with higher transverse momentum of the charmonium [1].

This thesis acts as a follow-up to these measurements by employing the upgraded ALICE detector in LHC run 3 at the currently largest center-of-mass energy of $\sqrt{s} = 13.6\,\mathrm{TeV}$. The self-normalized J/ψ yield will be extracted in the e^+e^- decay channel as a function of the self-normalized charged-particle multiplicity at mid-rapidity for p_T integrated J/ψ as well as in three p_T bins with $p_\mathrm{T} < 4\,\mathrm{GeV/c}$, $4 < p_\mathrm{T} < 8\,\mathrm{GeV/c}$, and $p_\mathrm{T} > 8\,\mathrm{GeV/c}$. It is aimed to show the stronger-than-linear increase of the J/ψ yield in the mentioned p_T bins and reduce the amount of statistical uncertainties compared to previous results. Such results may help to constraint theoretical models.

This thesis is structured as follows: Chapter 2 provides an overview of the theory of QCD physics to place the analysis on a solid foundation. The production mechanisms of charmonium and their dependency on the event multiplicity are given in chapter 3. Afterward, the detector setup and experimental methods are explained in chapter 4. The general analysis procedure is described in chapter 5 and results are presented in chapter 6 and summarized in chapter 7, with an outlook on further proceedings to this analysis. As well, AI tools for grammar and spell checking were utilized during the preparation of this thesis.

2 Theoretical Background

This chapter discusses the necessary theoretical background for understanding quarkonium production and its context in QCD. A brief overview of the standard model of particle physics and the related collider and QGP physics is provided.

2.1 The Standard Model

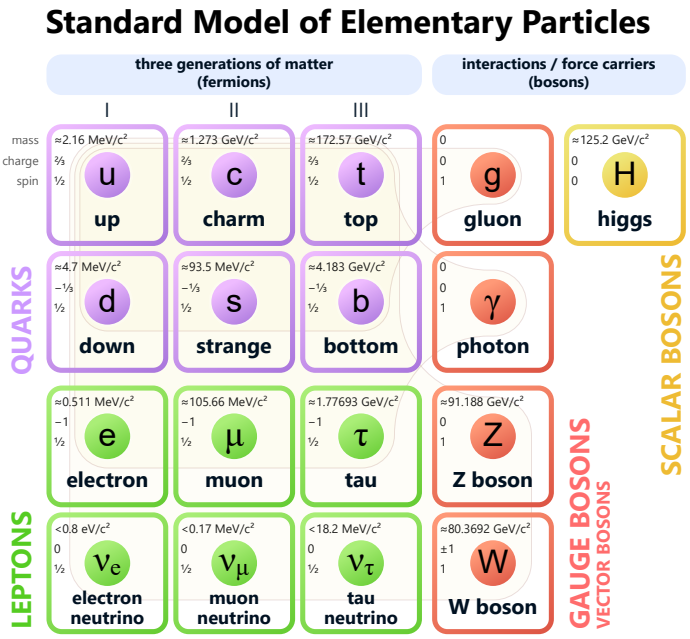


Figure 2.1: The standard model of particle physics listing all fundamental particles known up to date with their properties. [2]

Matter in the universe is composed of several fundamental particles called fermions. They interact via four fundamental forces: The Electromagnetic (EM) force, strong force, weak force, and gravity. Aside from gravity, where it is currently unknown, all forces are mediated via gauge bosons. Photons are responsible for the EM interaction, gluons for the strong force and $W^{\pm}$ and Z bosons for the weak force. Within the scales covered by particle physics, gravity can be neglected. Forces act on fermions and couple to the charge they carry. Coupling is described by

so-called coupling constants, often denoted as α, that provide a measure for the strength of the interaction. The EM interaction has a coupling constant of $\alpha_{\text{em}} \approx 1/137$. Photons are massless and do not carry any charge, leading to an infinite range of the interaction. Gluons are also massless but carry the charge of their interaction, which effectively reduces their range. The bosons of the weak interaction are massive, which limits the range of the interaction. All particles have an antiparticle that carries the same mass, but inverted charge and quantum numbers.
Fermions can be further classified into three generations, with each generation containing two quarks and two leptons. Quarks[1] participate in the strong interaction and carry color-charge as well as the electromagnetic charge. The group of leptons consists of electrons, muons, and tauons, all of which carry electromagnetic charges, and their corresponding neutrinos, which are neutral particles. Fermions participate in the weak interaction and carry a weak hypercharge. Quarks of the first and second generations have comparable masses, while the third generation exhibits significantly larger masses. A similar hierarchy is also apparent for charged leptons. Neutrinos are considered as massless, although it is evident that neutrinos carry a nonvanishing rest mass [3].
This picture of the theoretical background is called the Standard Model (SM) of particle physics. It is a Quantum Field Theory (QFT) that can be mathematically described by a Lagrangian $\mathcal{L}_{\text{SM}}$, from which equations of motions can be derived via Euler-Lagrange-Equations. A QFT describes the physics as a gauge field, and the observed particles are excitations of their corresponding fields, providing an elegant description of the physical effects of particles and antiparticles. Figure 2.1 shows this scene comprehensively in a single picture with all particle properties. The SM Lagrangian [4] is given by the following equation:

$$\mathcal{L}_{\text{SM}} = -\frac{1}{4}F_{\mu\nu}F^{\mu\nu} + i\bar{\psi}\gamma^{\mu}D_{\mu}\psi + \text{h.c.} + \psi_i y_{ij}\psi_j\phi + \text{h.c.} + |D_{\mu}\phi|^2 - V(\phi). \tag{2.1}$$

Here, $F_{\mu\nu}$ is the field strength tensor, ψ the fermion field, D_{μ} the covariant derivative, γ^{μ} are the Dirac gamma matrices and ϕ is the scalar Higgs field, y_{ij} denotes the Yukawa coupling matrix and $V(\phi)$ is the Higgs potential. The summation convention is used in this equation, as well as natural units. $-\frac{1}{4}F_{\mu\nu}F^{\mu\nu}$ describes the interaction of the gauge bosons. The interactions between fermions and gauge bosons are described by the second term $i\bar{\psi}\gamma^{\mu}D_{\mu}\psi + \text{h.c.}$, which is also the Lagrangian of the Dirac equation. All remaining terms belong to the Higgs mechanism, which gives the particles their mass via the interaction with the Higgs field. In the absence of any excitations (i.e., particles), the field is in the vacuum state and the expectation value of that field vanishes. The Higgs mechanism relies on the assumption that a field with a non-vanishing vacuum expectation value exists, where the quarks, charged leptons, and gauge bosons of the weak interaction couple to. This non-vanishing vacuum expectation value leads to the observed particle mass.
The standard model does not include all our current knowledge about particle physics. Observations of the orbital velocity of stars in galaxies provide evidence of the existence of a large

[1] Quarks were first introduced in 1964 by Murray Gell-Mann and George Zweig independently.

amount of mass around galaxies [5]. Stars in the outer regions of the galaxy move with a higher relative velocity than the predicted velocity, but the visible mass cannot explain this discrepancy. One approach to resolve this issue is to predict a new type of particle that is not part of the SM so far.[2]

2.2 Quantum Chromodynamics

QCD[3] is a QFT that describes the behavior of the observed strong force between quarks q and gluons g. *Color* is the charge of the strong interaction[4] and appears in three variants: red, blue, and green. Antiparticles carry the corresponding anticolor: antired, antiblue, and antigreen[5]. The appearance of three types of colors is represented by a SU(3) group structure of the interaction. Quarks carry two distinct colors, and gluons carry a color and its anticolor. In this fact lies one significant difference between the strong and the EM force: The interaction charge is carried by the exchange boson itself. Therefore, gluons can participate in the interaction similarly to quarks. Mathematically, this results in an additional interaction term in the Lagrangian theory, which is given by [6]

$$\mathcal{L}_{\text{QCD}} = -\frac{1}{4} F^a_{\mu\nu} F^{a\mu\nu} + \bar{\psi}_j (i\gamma^\mu D_\mu - m_j)\psi_j + g_s f^{abc} A^b_\mu A^c_\nu. \tag{2.2}$$

Here, $F^a_{\mu\nu}$ denotes the gluon field strength tensor, with $\mu, \nu = 0 \dots 3$ representing spacetime indices and $a = 1 \dots 8$ representing the color index. $\bar{\psi}_j (i\gamma^\mu D_\mu - m_j)\psi_j$, similar to equation (2.1), is the interaction term for the quarks. The covariant derivative is defined via $D_\mu = \partial_\mu - i g_s T^a A^a_\mu$ with T^a being the eight generators of the SU(3) group and A^a_μ the eight gluon fields, where index $j = 1, \dots 6$ runs over all quark types. $g_s f^{abc} A^b_\mu A^c_\nu$ last term in the equation describes the gluon self-interaction with the structure constants f^{abc} of the SU(3) group. This complicated mathematical structure arises because the SU(3) group is non-abelian, meaning that the generators of the group do not commute. An important effect of this structure is the short range of the interaction and the confinement into color neutral particles, called hadrons. The former refers to being in a color singlet state. Physically, this corresponds to a potential between two quarks that increases linearly with a larger distance between them. This can be pictured with a *flux tube*, which arises between the quarks, as shown in figure 2.2. When the potential energy is above the threshold to create new $q\bar{q}$ states, it becomes energetically favorable to break the flux tube and create new particles that conserve the quantum numbers of the state before the string breaking. This process is called hadronization.

Increasing energy with distance corresponds to an increasing interaction coupling. This is denoted as running coupling and is mathematically put in place by $\alpha_s = \alpha_s(Q^2)$ being a function of

[2] Candidate particles for dark matter are so-called Weakly Interacting Massive Particles (WIMPs) or the hypothetical Axions. Other types of neutrinos are also discussed as candidates.

[3] Chromo comes from the Greek word $\chi\rho\tilde{\omega}\mu\alpha$, which translates to color.

[4] The name color for the charge is misleading and must not be confused with optical color. Quarks and gluons do not have a color in the optical sense.

[5] Sometimes the anticolors are denoted as cyan, magenta, and yellow.

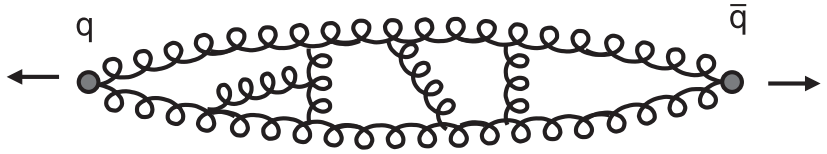


Figure 2.2: Schematic view of a color flux tube between a $q\bar{q}$ pair. Curled lines denote gluons that exhibit self-interaction. [7, p. 249]

the momentum transfer Q^2 of the interaction. In first order of perturbation theory, the following expression is found for the coupling constant [8, 9]

$$\alpha_s(Q^2) \approx \frac{4\pi}{\beta_0 \ln\left(\frac{Q^2}{\Lambda^2_{\mathrm{QCD}}}\right)}. \tag{2.3}$$

Here, $\beta_0 = \frac{11}{3}n_c - \frac{2}{3}n_f$ is the first-order term in the perturbation series of the QCD β function, n_c denotes the number of colors, n_f the number of flavors at the momentum scale. $\Lambda_{\mathrm{QCD}} \approx 200\,\mathrm{MeV}$ is a constant called QCD scale parameter and describes a threshold up to which perturbative methods are reasonable approximations. Its value depends on the renormalization[6] scheme. However, when the process occurs at higher energies (or equivalently smaller distances), the coupling constant decreases. This process is called asymptotic freedom. A further effect of this behavior is the emergence of a new state of matter, called QGP, which will be discussed in section 2.4. Latest experimental results and theoretical predictions of the strong coupling constant are shown in figure 2.3. Due to confinement, only color-neutral configurations of hadrons appear in nature. These are either mesons, which are built of quarks and antiquarks, or baryons, made of three quarks or antiquarks. Combinations with more quarks, such as tetra- or pentaquarks, as well as combinations of gluons (glueballs) are also theoretically possible and were denoted as exotic mesons. Evidence for their existence was found in earlier reviews [10, 11]. Quarks and Gluons are collectively called partons[7]. Hadrons, as spatially extended structures, are composed of partons, and their structure has an eminent influence on the interactions in QCD. This structure can be quantified by Parton Distribution Functions (PDF's) $xf(x, Q^2)$, where x is the momentum fraction of the parton and Q^2 is the momentum transfer. Those PDF's are probability density functions that describe the probability density of a parton carrying a specific momentum fraction of the hadron. The momentum transfer also determines the resolution of the PDF: the lower the Q^2 is, the more low-momentum partons can be distinguished. In particular, gluons appear at low momentum fractions with an order of magnitude higher probability density than other partons. Figure 2.4 shows pictures of the proton PDF at a momentum transfer of $Q^2 = 10\,\mathrm{GeV}^2$ and $10^4\,\mathrm{GeV}^2$, where the valence quarks are denoted with the subscript v and the others are sea-quarks.

[6] In renormalization, parameters of the theory will be redefined with respect to an energy scale. This removes terms that diverge under integration when calculations are performed.

[7] This name was historically proposed by Richard Feynman as the main component of the hadrons. Instead, the name quarks had prevailed itself over Feynman's proposal.

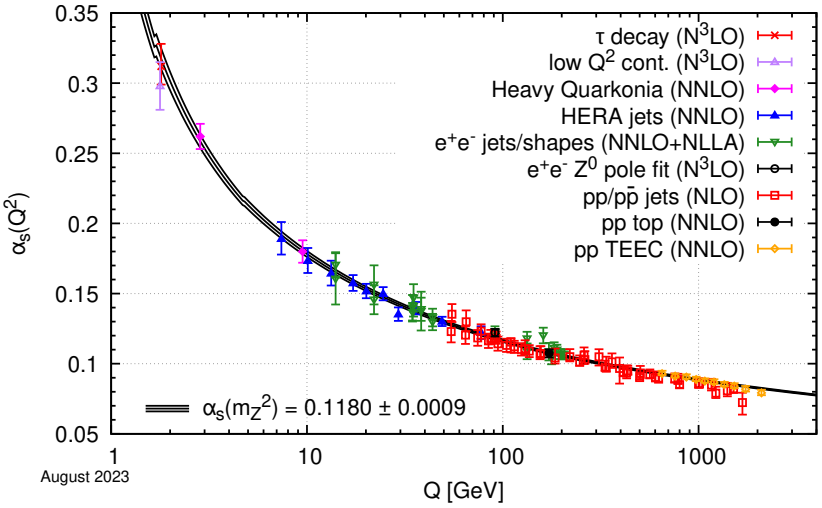


Figure 2.3: The QCD running coupling constant α_s as a function of the energy scale Q determined with various methods compared to the current Particle Data Group (PDG) average $\alpha_s(m_Z^2)$. [12]

Experimentally, PDF's can be investigated by Deep Inelastic Scattering (DIS), where a lepton is scattered off a proton, providing insights into the momentum transfer dynamics of the collision. Measured quantities are the structure functions from which one obtains parameterized PDF's that are then evolved in the momentum transfer Q^2 according to the DGLAP equations [13, 14, 15].

QCD is a non-abelian and non-linear theory, which results in many equations that cannot be solved analytically. At high-energy transfers, approximately when the condition $Q^2 > \Lambda^2_{\text{QCD}}$ is fulfilled, the coupling between quarks is sufficiently weak such that perturbation theory can be applied. This regime is denoted as pQCD or hard QCD. When the condition is not fulfilled and the momentum transfer is below the pQCD threshold, the regime is called soft QCD and only computer simulations are applicable to perform calculations. These simulations rely on the discretization of the four-dimensional space-time into a 4D-lattice, hence the name lattice Quantum Chromodynamics (lQCD). The lattice sites play the role of quarks, and the edges the role of the gluons. This method requires a vast amount of computing power, making it suitable only when high-performance computing farms are available. For the final result, the continuum limit of the distinct lattice is taken. At non-vanishing baryochemical potential, lQCD cannot be applied. In these cases, Effective Field Theories (EFT's) or potential methods[8] have to be used.

[8] Effective Field Theories are simplified models of full theories at specific energy scales. Potential Methods on the other hand approximate theories by finding potentials that describe the system on the desired energy scale, and use e.g., the Hamilton formalism to yield solutions.

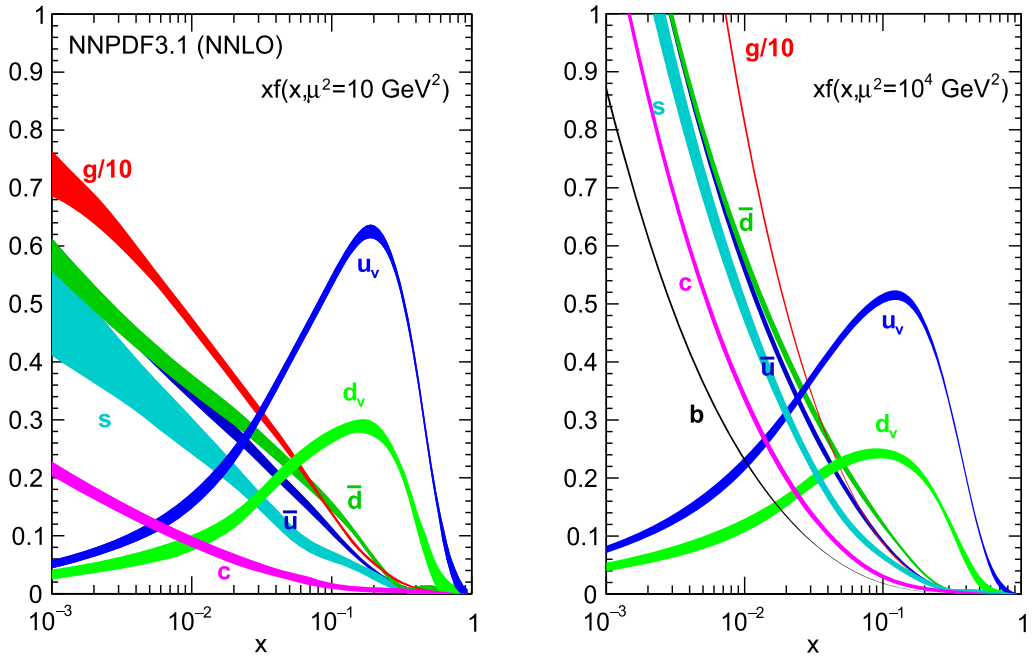


Figure 2.4: Parton Distribution Functions of protons at energy scales of (a) $10\,\mathrm{GeV}$ and (b) $10^4\,\mathrm{GeV}$. In both cases, the gluon PDF is scaled by a factor of $1/10$ to reach the same range as the other PDF's for visual comparison. [16]

2.3 Hadron-Hadron Collisions

Experimental access to QCD processes can be gained by colliding hadrons in processes like pp, $\mathrm{p\bar{p}}$, p–A, or A–A collisions, where p refers to protons and A is a placeholder for possible heavier elements with mass number A. An example of a pp collision is shown in figure 2.5. Interactions in such collisions produce new particles that traverse a detection system. Measuring their properties provides insights into the processes that occurred during the collision (also called event). Kinematics of hadron-hadron collisions are quantified by two variables. The transverse momentum p_T is defined as the momentum fraction transverse to the beam direction (typically the z-axis)

$$p_\mathrm{T} = \sqrt{p_x^2 + p_y^2}. \tag{2.4}$$

Here, p_x and p_y are the first and second Cartesian coordinates of the three-momentum vector $\vec{p} = (p_x, p_y, p_z)$. The longitudinal part of the momentum vector is p_z, such that $p = \sqrt{p_\mathrm{T}^2 + p_z^2}$. As second kinematic variable, the rapidity y is used, which is a measure of the velocity of the particle. It is defined via

$$y = \frac{1}{2} \ln\left(\frac{E + p_z}{E - p_Z}\right). \tag{2.5}$$

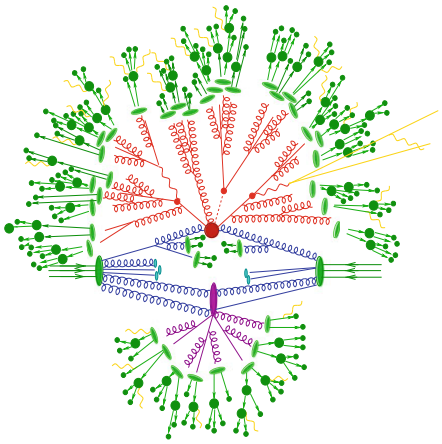


Figure 2.5: Schematic picture of a proton-proton collision with several partonic processes and electromagnetic interactions. [17]

E is the particle energy. Using rapidity as a kinematic variable has the advantage that differences in rapidity are invariant under Lorentz transformations and are thus suitable for calculations in a relativistic environment [7]. For highly energetic particles, the mass is usually negligible compared to the energy. This results in the rapidity being only dependent on the polar angle θ between the particle and the longitudinal axis, because $p_z \approx E\cos(\theta)$. The rapidity y is then approximately equal to another quantity called the pseudorapidity η with

$$y \approx \eta = -\ln\left(\tan\left(\frac{\theta}{2}\right)\right). \tag{2.6}$$

Particle production in hadron-hadron collisions is a statistical process. One cannot calculate with absolute certainty that a process will occur under given conditions. Instead, only probabilities for certain processes are accessible quantities. Experimentally, those probabilities are encoded in differential cross-sections $\mathrm{d}\sigma$ that can be determined in a mathematical framework in QFT that is based on perturbation theory. For pp collisions, one finds the following expression for the total hadronic cross-section for a process $AB \to X$ under the condition that $Q \gg \Lambda_{\mathrm{QCD}}$ [12]:

$$\mathrm{d}\sigma^{AB\to X}\left(Q^2\right) = \sum_{i,j,X'} f_i^A(Q^2) \otimes \mathrm{d}\hat{\sigma}^{ij\to X'}\left(Q^2\right) \otimes f_j^B(Q^2) + \mathcal{O}(1/Q^2). \tag{2.7}$$

A is the projectile proton and B the target proton, with $f_{i/j}^{A,B}$ being the corresponding PDF's. The sum runs over all possible partons i and j involved at the given momentum scale Q^2 as well as over all possible final states X' and $\mathrm{d}\hat{\sigma}$ is the hard partonic scattering cross-section, calculable via pQCD. Expressing equation (2.7) in this way is called collinear factorization. To abstract from this formalism from pp collisions to heavy-ion collisions, different models are available. A very successful approach is to treat AA collisions as an independent sum of pp collisions.

Distributions of the above discussed kinematic variables and cross-sections build the experimental foundation of investigations of QCD processes. A fundamental and experimentally easily accessible quantity, though theoretically very hard to describe[9], is the number of produced charged-particles N_{ch} in a collision. The number of charged-particles in an event is counted and filled into a histogram, which is then divided by the number of events, leading to a probability distribution $P(N_{\mathrm{ch}})$ that tells the probability of finding an event with N_{ch} particles with the probability $P(N_{\mathrm{ch}})$. It was proposed by Richard Feynman, that particle production becomes independent of collision energy. However, observations at the Relativistic Heavy Ion Collider (RHIC) showed that the proposed behavior is violated [18]. The mean multiplicity $\langle N_{\mathrm{ch}} \rangle$ was found to scale logarithmically with the collision energy $\langle N_{\mathrm{ch}} \rangle \propto \ln(\sqrt{s})$. The proportionality implies that the rapidity density $\mathrm{d}N_{\mathrm{ch}} / \mathrm{d}y$ is constant because y scales with the same logarithmic rule. This behavior was also not observed. Later, a similar concept called KNO scaling was proposed, where the multiplicity distributions, normalized to the average number of particles $P(N_{\mathrm{ch}}) / \langle N_{\mathrm{ch}} \rangle$ is independent of the collision energy. KNO scaling succeeds at energies below $\sqrt{s} \approx 200\,\mathrm{GeV}$, whereas it is violated for higher energies. Such a violation is expected to result from the occurrence of multiple partonic interactions in the collision.
In addition to the charged-particle multiplicity, the distribution of transverse momentum provides important insights into the dynamics of a collision. The probability of producing a particle with three momentum p can be expressed as follows:

$$E\frac{\mathrm{d}^3\sigma}{\mathrm{d}p^3} = \frac{1}{2\pi p_{\mathrm{T}}}\frac{\mathrm{d}^2\sigma}{\mathrm{d}p_{\mathrm{T}}\,\mathrm{d}y}. \tag{2.8}$$

The azimuthal part of the cross-section is integrated over the full angle. To convert a cross-section to a probability distribution $\mathrm{d}^2N_{\mathrm{ch}}/\,\mathrm{d}p_{\mathrm{T}}\,\mathrm{d}y$, one has to multiply equation (2.8) with the total inelastic cross-section σ_{INEL}

$$\frac{\sigma_{\mathrm{INEL}}}{2\pi p_{\mathrm{T}}}\frac{\mathrm{d}^2\sigma}{\mathrm{d}p_{\mathrm{T}}\,\mathrm{d}y} = \frac{1}{2\pi p_{\mathrm{T}}}\frac{\mathrm{d}^2N_{\mathrm{ch}}}{\mathrm{d}p_{\mathrm{T}}\,\mathrm{d}y} \tag{2.9}$$

This transverse momentum distribution provides insight into several effects that arise from QCD and will be discussed in section 2.4. Throughout the collision, the matter passes through different stages. Initially, the state of the collision is primarily determined by the hadron PDF's before the collision. When sufficient energy densities are reached, a QGP forms after about $1\,\mathrm{fm/c}$. After the fireball cools down, the hadronization process occurs where most of the particles are formed and hadronic rescattering processes take place until the freeze-out is reached. This is pictured in figure 2.6. Typically, a time of about $10\,\mathrm{fm/c}$ has passed. Particles created during the process can be investigated using a detector. The physical processes behind the QGP and how to identify whether it has been created will be discussed in the next section.

[9] The reason for this is that the production of particles is mainly driven by soft processes that cannot be evaluated with perturbative methods.

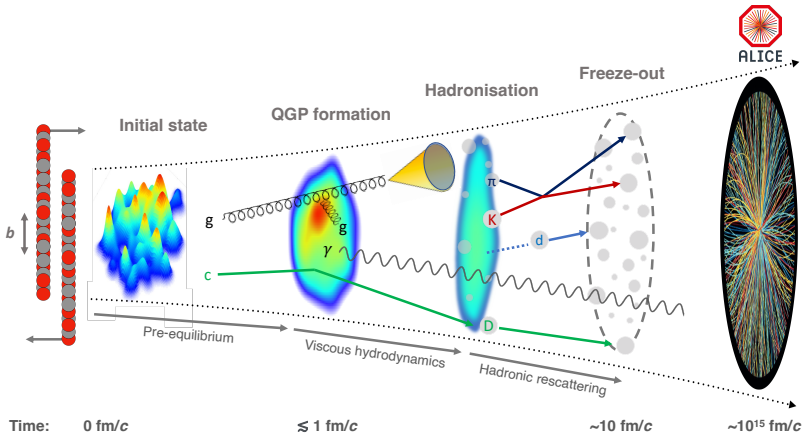


Figure 2.6: Evolution of a heavy-ion collision with an impact parameter b in the ALICE detector with the corresponding timescale, ranging from $0\,\mathrm{fm/c}$ to $1 \cdot 10^{15}\,\mathrm{fm/c}$.[19]

2.4 Quark-Gluon-Plasma

The previously described behavior of QCD matter at high-energy transfers has an important consequence, considering that in the early universe, the density, and temperature had to be high enough to reduce the coupling between strongly interacting particles down to a level where the quarks and gluons behave as quasi-free particles. Possibilities for the existence of such a state of matter were first theorized in 1975 by John C. Collins and M.J. Perry in their work [20] and independently by Cabibbo and Parisi in [21]. They proposed that in the super-dense cores of neutron stars, the matter exhibits a phase transition from regular nuclear matter into an asymptotically free state of quarks and gluons. Already in 1977 Edward Shuryak proposed the theory that the universe was also in this kind of state just moments after the big bang [22]. This new state of matter was then QGP [23].
Creating this type of matter experimentally is only possible under extreme conditions. The use of heavy-ion collisions as a tool to create a QGP and study its properties is currently the only available option. Measurements performed by the NA50 experiment at the Super Proton Synchroton (SPS) that was operated by the European Organization for Nuclear Research (CERN) indicated first QGP-like structures in the year 1994. CERN announced that a new state of matter was found in collisions of lead ions just six years later. To create a QGP, certain conditions must be satisfied. The system's temperature must surpass a critical threshold of $T_c \approx 150\,\mathrm{MeV}$ to $160\,\mathrm{MeV}$[10], beyond which quark and gluon confinement is lifted. A temperature this high can only be reached

[10] The temperature is given in energy units per Boltzmann constant k_B. A critical temperature of $150\,\mathrm{MeV}$ corresponds to approximately $1.8 \cdot 10^{12}\,\mathrm{K}$.

with a certain energy density ε above a critical value of $\varepsilon_c \approx 0.3\,\mathrm{GeV\,fm^{-3}}$ to $0.4\,\mathrm{GeV\,fm^{-3}}$, depending on the precise definition of T_c [24]. The energy density is generally given by the Bjorken formula

$$\varepsilon_{\mathrm{Bj}} = \frac{1}{S_\perp \tau} \frac{\mathrm{d}E_\mathrm{T}}{\mathrm{d}\eta}\Big|_{\eta=0}. \tag{2.10}$$

Where $S_\perp$ is the transverse overlap area of both nuclei and τ is the formation time of the medium. The value $\mathrm{d}E_\mathrm{T} / \mathrm{d}\eta$ corresponds to the transverse energy per pseudorapidity and is an experimentally available quantity.

To achieve these critical values, it is required to have a system that is large enough. Typically, heavier elements such as gold or lead have a sufficiently high volume. In central Pb–Pb collisions at $\sqrt{s_\mathrm{NN}} = 2.76\,\mathrm{TeV}$ performed at the LHC, the ALICE collaboration measured an energy density up to $12.3 \pm 1.0\,\mathrm{GeV\,fm^{-3}}$ [25, 26]. Via the concept of the grandcanonical ensemble, the temperature of a system is related to a quantity called the chemical potential μ[11]. One finds via lQCD calculations that the phase transition from regular matter to a QGP can happen at different temperatures, depending on the value of the baryochemical potential μ_B of the system. The baryochemical potential is a special kind of chemical potential that is related to the matter-antimatter asymmetry and baryon number of the systems. It provides a measure of how the energy of the system changes when the number of baryons is varied. In the schematic representation shown in figure 2.7, known as the QCD phase diagram, matter exists in a confined (hadronic) state below the transition line $T = T(\mu_B)$. A phase transition to the QGP occurs. Depending on the value of μ_B, different types are possible. For values of $\mu_B \approx 0$, a crossover-type phase transition is expected, indicating that there is no sharp boundary between two phases but rather a smooth transition. This condition was probably fulfilled in the early universe, and it is currently studied in the LHC at CERN. For intermediate values between $\mu_B \approx 100\,\mathrm{MeV}$ to $500\,\mathrm{MeV}$ a critical point is expected where the phase transition type changes and becomes first-order type. This means that the order parameter is not continuos anymore and experiences a jump. [12] To date, it is not known whether a critical point exists. Experiments like the future Compressed Baryonic Matter (CBM) experiment at the Facility for Antiproton and Ion Research (FAIR) complex will evaluate other regions of the QCD phase diagram to answer this question. To experimentally identify a QGP, different probes are available. A recently published review [24] describes the signatures in detail. A short overview will be provided here. Historically, one of the first proposed signatures was the measurement of an energy density and temperature above the critical values, but it is not sufficient to identify whether the QGP was really created. With time moving on, more and more signatures were proposed. The increased production of antibaryons containing strange quarks was an early prediction as a signature for creating deconfined matter. Strange particles are rarely created in regular nuclear matter interactions due to the larger

[11] It has to be noted that in statistical physics, systems with the order of 10^{22} particles or more are the subject of interest, while in QCD one typically deals with a few hundreds up to a few thousand. Despite this drastic difference in numbers, the statistical approach is still very successful.

[12] The order parameter of QCD matter is the so-called Polyakov loop P. This is a theoretical quantity that measures whether quarks are deconfined or not.

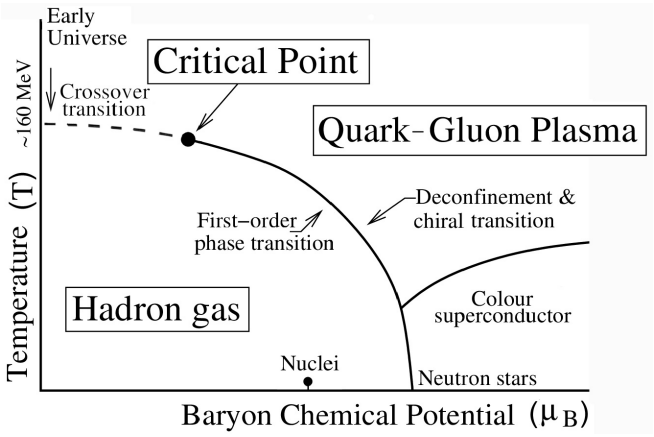


Figure 2.7: Sketch of the QCD phase diagram with the temperature T as a function of the barychemical potential μ_B with notations on different phases of QCD matter. [27]

energy production threshold than up and down quarks. When the partons in the QGP reach thermal equilibrium, deconfined thermal[13] gluons can interact more easily with one another. This results in an enhanced yield of baryons containing strange quarks, which cannot be produced without the hot QGP phase.

With sufficiently high energies, also heavier quarks like the charm c, bottom b, and top t can be produced. The c and b quarks can form special kinds of mesons, called quarkonia[14], where they bind with their corresponding antiparticle to form a positronium-like structure. The $c\bar{c}$ states are called charmonium and $b\bar{b}$ states bottomonium. Detecting a J/ψ meson ($c\bar{c}$ state with quantum numbers $J^{PC} = 1^{--}$) in 1974 by Burton Richter and Samuel Ting led to a November revolution in particle physics, where many new mesons were found[15]. Later, the J/ψ became an interesting subject in QGP studies. Due to the charm quark, the constituents of the J/ψ must be created in the initial collision. The binding energy of the J/ψ within heavy-ion collisions is in the range of $600\,\mathrm{MeV}$ to $700\,\mathrm{MeV}$, depending on the coupling between the quarks [28]. Because they carry a large mass compared to the other quarks, they move in a non-relativistic regime and exhibit the potential of the form

$$V(r) = -\frac{\alpha_S}{r} + \kappa r. \tag{2.11}$$

This potential is named the Cornell-Potential and is shown in figure 2.8. α_S is the strong coupling constant at the given momentum transfer and $\kappa \approx 1.0\,\mathrm{GeV\,fm^{-1}}$ is the string-tension [7]. One notices that the first term $-\alpha_S/r$ corresponds to a coulomb-like repelling force, while the term κr leads to an increase in energy above a certain distance. However, in a QGP the J/ψ meson

[13] Thermal in this sense means that the energy distribution in the deconfined matter does not change anymore.
[14] Top quarks are in general not able to bind into quarkonium states, because their lifetime is shorter than the hadronization time of the bound state.
[15] The group of Richter named the new particle ψ, while the group of Ting proposed the name J. This led to the confusing and unique double-name of the particle.

exhibits color screening[16] due to the free moving color charges around the particle. Because

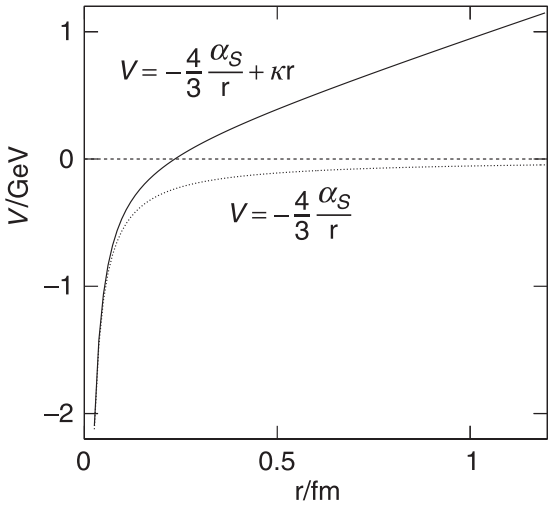


Figure 2.8: The QCD potential between two heavy quarks with comparison to the Quantum Electrodynamics (QED) potential. Adopted from [7]

of the interactions of the quasi-free quarks and gluons, the effective binding force between the c and $\bar{c}$ quarks are decreased exponentially [29]. This process is also called J/ψ melting and can be measured by determining the nuclear modification factor $R_{\mathrm{AA}}(J/\psi)$, which is defined as the ratio of the J/ψ transverse momentum spectrum in heavy-ion collisions to the one in pp collisions, where the pp spectrum is scaled by the number of binary nucleon-nucleon collisions N_{coll}, determined with the Glauber model [30]:

$$R_{\mathrm{AA}}(J/\psi) = \frac{1}{N_{\mathrm{coll}}} \frac{\mathrm{d}N^{\mathrm{AA}}_{J/\psi} / \mathrm{d}y}{\mathrm{d}N^{\mathrm{pp}}_{J/\psi} / \mathrm{d}y}. \tag{2.12}$$

The experimental results on the R_{AA} of J/ψ mesons are shown in figure 2.9. A value of $R_{\mathrm{AA}} < 1$ value indicates suppression of the J/ψ yield. Measurements performed in previous experiments agree with this theory and show similar results for bottomonium.
When particles traverse the hot, deconfined medium, they interact with the surrounding charges and begin to radiate gluon bremsstrahlung. When particle jets[17] move through the QGP, their constituents lose energy by the bremsstrahlung process. On average, after moving the path length L, a high-energy parton loses the energy $\Delta E \approx \hat{q}L^2$, where $\hat{q}$ is the transport coefficient defined by $\hat{q} = \mathrm{d}\left\langle p_{\mathrm{T}}^2 \right\rangle / \mathrm{d}L$. Measuring the charged-particle yield $\mathrm{d}N_{\mathrm{ch}} / \mathrm{d}\eta$ in heavy-ion collisions and pp collisions and calculating the nuclear modification factor provides insides into jet quenching.

[16] A similar mechanism exists in classical electrodynamics, called Debye-screening.
[17] Jets are collimated sprays of partons, created by other partons when they scatter off other particles. The partons start to radiate more quarks and gluons, which hadronize and are correlated with each other.

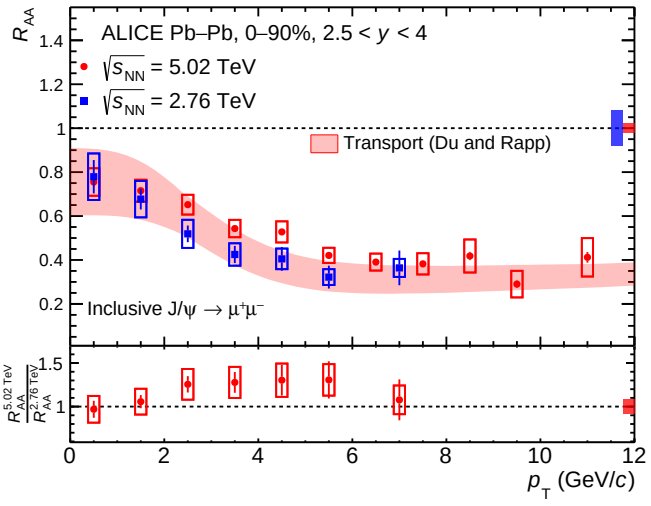


Figure 2.9: Nuclear modification factor of inclusive J/ψ mesons, reconstructed in the $\mu^+\mu^-$ decay channel at forward rapidity in Pb–Pb collisions at $\sqrt{s_{\mathrm{NN}}} = 2.76\,\mathrm{TeV}$ and $\sqrt{s_{\mathrm{NN}}} = 5.02\,\mathrm{TeV}$ as a function of p_{T} compared to predictions from the Transport Model. [31]

Although the QGP is defined as a state of deconfined matter and the Quarks and Gluons are asymptotically free, they are still loosely coupled by the strong force of the other charges around them. This rest-interaction results in new phenomena that cannot be explained without the picture of the QGP. The motion of the particles starts to show collective behavior, meaning that their movement is correlated instead of independent to each other, resulting in the medium behaving like a perfect relativistic fluid with low viscosity[18]. QGP as a name has a historical background, today it is known that the medium behaves more like a fluid rather than a plasma. Such perfect-fluid-like behavior is accompanied by several hydrodynamic effects. Due to a non-vanishing pressure gradient in the medium, the particles are pushed outwards in the radial direction. An outcome of this radial flow effect is an increase in the average transverse momentum $\langle p_{\mathrm{T}} \rangle$. Another type of flow is the elliptic flow, which is caused by the spatial anisotropy that non-central collisions exhibit. It can be quantified by the second Fourier coefficient v_2 of the azimuthal momentum distribution $v_2 = \langle \cos(2\phi) \rangle$, where ϕ is the azimuthal angle of the particles. The flow effect results in measurable long-range correlations, revealing an unexpected ridge in the two-particle correlation function. Particles are created together in the medium and are separated by radial flow, indicating a collective behavior that would not be possible without a QGP.
Generally, the previously described phenomena were not observed in pp collisions. However, in the current generation of particle accelerators, pp collisions can reach multiplicities similar to those in heavy-ion collisions. Investigations of such high-multiplicity pp collisions showed that

[18] This is in contrast to the name Quark-Gluon-**Plasma**, which indicates a medium of free moving and loosely interacting particles.

collective effects generally occur from a thermalized QCD medium. The emergence of long-range correlations was already observed in 2010 by the CMS collaboration [32]. Abundant production of strange particles as a function of the charged-particle density, which fits results from p–A and A–A collisions, was then found by the ALICE collaboration in 2017 [33]. The interpretation of these results is far from clear. Two possible explanations are currently discussed, one of which relates the uprising collective phenomena to the same effects as in nucleus-nucleus collisions. The other explanation relies on the assumption that a proton-proton collision is more than the sum of the independent parton-parton interactions. Strangeness enhancement may also be explained within the rope hadronization model [34], where overlapping color strings may shove each other and fuse into ropes. This has a notable effect on the hadronization procedure in pp collisions. Collective effects may be associated to a concept called CR [35], where strings in the initial state are rearranged. Saturation effects in the initial state or interference effects of the parton wave functions may also cause the flow-like effects [36, 37]. This topic is still under theoretical investigation and is important for the future understanding of QCD and heavy-ion collisions.

2.5 Interaction of Charged Particles with Matter

Particle detection relies on the interaction between the particles of interest and the detector material. Among the various interaction types, the EM interaction is the most favorable because of its long-range nature. When charged particles traverse a medium, they interact with the surrounding atoms. On this scale, the atoms do not appear neutral anymore. Instead, the interactions occur by ionizing the surrounding atoms, meaning they deposit a certain amount of energy in the detector. This energy loss can be quantified using the Bethe-Bloch-Equation. Different forms of the equation exist for different energy scales and types of particles. At an intermediate energy scale ($0.1 < \beta\gamma < 1000$), relativistic heavy charged particles deposit an average energy loss $-E$ per unit length x according to [12]

$$\left\langle -\frac{\mathrm{d}E}{\mathrm{d}x} \right\rangle = \frac{Z}{A}\frac{Kz^2}{\beta^2}\left[\frac{1}{2}\ln\left(\frac{2m_e c^2\beta^2\gamma^2 W_{\mathrm{max}}}{I^2}\right) - \beta^2 - \frac{\delta(\beta\gamma)}{2}\right]. \tag{2.13}$$

Here, z is the charge number of the incident particles, Z and A are the atomic number and atomic mass of the detection material, $\beta = v/c$ is the velocity of the particle, and γ is the Lorentz factor. All remaining constants are material-specific types and are discussed in [12].
The description above relies on the assumption that the incident particles are considered to be heavy charged particles. To describe the energy loss of electrons in a medium, modifications have to be made to equation (2.13). One has to consider Møller-Scattering[19] between the incident electrons and the shell electrons of the absorber. The cross-section of Møller-Scattering

[19] Møller-Scattering is the name for the QED process of $e^- e^- \rightarrow e^- e^-$ scattering

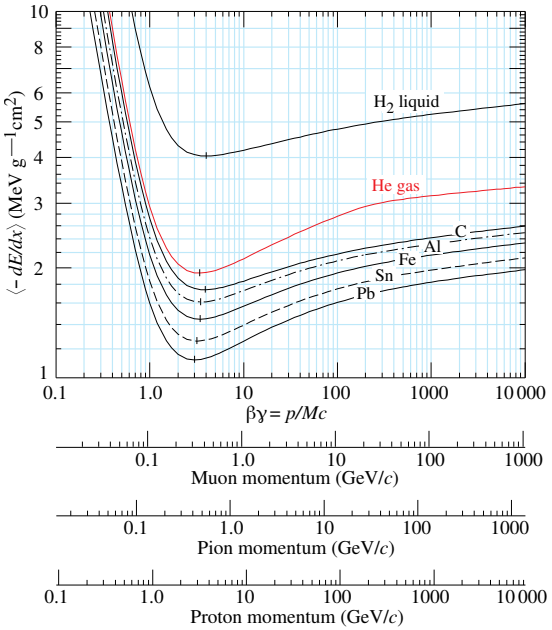


Figure 2.10: Average energy-loss per unit length of muons, pions, and protons in different stopping materials.[12]

is proportional to the inverse square of the energy $\sigma \propto E^{-2}$. Also, the maximum energy transfer W_{max} has to be modified because an electron can transfer much more of its total energy to the scattering partner than a heavy particle can do. Because of the inverse square law for the Møller cross-section, other processes become more significant at higher energies. Above a certain threshold of approximately $800/Z\,\text{MeV}$ [12], the electrons start to radiate bremsstrahlung, which becomes the dominant energy loss mechanism.

Charmonium Production in Proton-Proton Collisions

3

The following chapter first provides an overview of current theories of charmonium production mechanisms for prompt- and non-prompt charmonium. This discussion is extended by describing the multiplicity dependence of charmonium production and is concluded by an overview of the current experimental status on this topic.

3.1 Prompt and Non-Prompt Charmonium Production

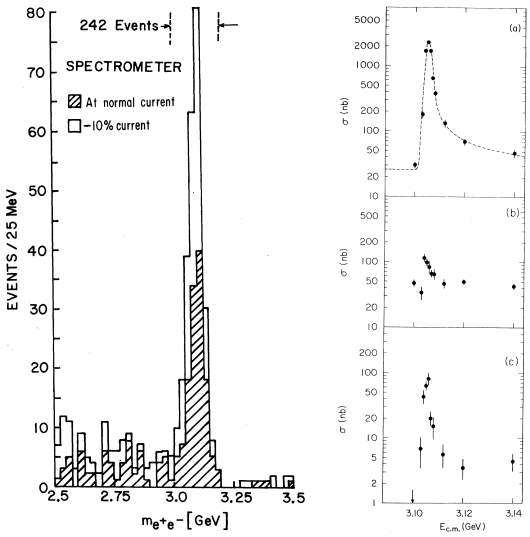


Figure 3.1: Left: Invariant mass distribution of the J/ψ resonance from 242 p–Be events, reconstructed via the e^+e^- decay channel at Brookhaven National Laboratory. [38] Right: Cross-section $e^+e^- \rightarrow$ hadrons with the J/ψ detected at the Stanford Linear Accelerator Center (SLAC). [39]

During the early stages of the development of the standard model, only three light quarks u, d, and s were proposed. Although major successes in the description of particle production were achieved, the introduction of a fourth quark, the charm c, enabled more accurate theoretical predictions of the known meson masses at the time. Additional experimental lack of evidence for previously predicted flavor-changing neutral currents in weak interactions led to the establishment of the GIM-mechanism in 1970 by Glashow, Iliopoulos, and Maiani, as it is described

in [40]. By introducing a fourth, significantly heavier quark, the GIM-mechanism can describe the observed suppression of certain decay modes of K mesons. In 1974, the desired charm quark was then found almost simultaneously by the two independent groups of Burton Richter at the SLAC and Samuel Ting at the Brookhaven National Laboratory. Both groups measured the signal of a meson with a mass and lifetime corresponding to a $c\bar{c}$ state, called a charmonium. Richter's group named the new particle ψ meson and Tings group named it J. Officially, the particle was then named J/ψ meson. The J/ψ has a mass of $m_{J/\psi} = 3096.600 \pm 0.006\,\mathrm{MeV/c^2}$ with a narrow decay width of $\Gamma_{J/\psi} = 92.9 \pm 2.8\,\mathrm{keV/c^2}$ [12] and the quantum numbers of the photon, with $J^{PC} = 1^{--}$. Such a narrow width, corresponding to a long lifetime[1], arises from the decay mechanics of the J/ψ. Its mass is below the open charm threshold of $m_{D^0} \approx 3739\,\mathrm{MeV/c^2}$ and thus a strong decay into D^0 mesons is not allowed. Since color-charge is a conserved quantity, a decay into one gluon is not possible. Two-gluon decays are forbidden due to parity conservation. Only strong decays involving at least three gluons are allowed for which the Okubo-Zweig-Iizuka (OZI) mechanism has to be considered, which states that decays with disconnected quark lines are suppressed. This indicates that the electromagnetic decay modes are compatible with the strong modes, having a branching ratio of $\Gamma_1(J/\psi \to \text{hadrons})/\Gamma = 87.7 \pm 0.5\,\%$ while the modes with electron or muon final states have branching ratios of

$$\Gamma_5(J/\psi \to e^+e^-)/\Gamma = 5.971 \pm 0.032\,\% \quad \text{and} \quad \Gamma_7(J/\psi \to \mu^+\mu^-)/\Gamma = 5.961 \pm 0.033\,\%.$$

Discovering the J/ψ and a fourth quark flavor provided strong evidence for the quark model and triggered many other important discoveries in particle physics, now known as the November revolution.

Just days after the discovery of the J/ψ, a radial excitation state called $\psi(2S)$[2] was found. It has a mass of $m_{\psi(2S)} = 3686.093 \pm 0.034\,\mathrm{MeV/c^2}$ and a decay width of $\Gamma_{\psi(2S)} = 286 \pm 16\,\mathrm{keV/c^2}$ with similar decay modes to the J/ψ meson, with an additional $\tau^+\tau^-$ channel[3]. Since the properties are similar to the J/ψ, the $\psi(2S)$ is more sensitive to the conditions created in a QGP, because it is less tightly bound. The $J^{PC} = 0^{-+}$ ground state of the charmonium family is the η_c meson.

Several charmonium production mechanisms in hadronic collisions exist. Without any further classification, measurements of all charmonium signals are called *inclusive*. It comprises three main components

- Non-Prompt J/ψ: Higher-mass b-hadrons can decay via weak interactions into states containing J/ψ, such as $B \to J/\psi + X$. B mesons are long-living particles that travel distances of about $500\,\mu\mathrm{m}$ before decaying. This long lifetime can be used to reject J/ψ candidates that were not produced in the initial collision and thus do not carry information

[1] *Long* has not to be taken literally in this sense. Other heavy mesons decay primarily via the strong interaction with a lifetime of the order $10^{-23}\,\mathrm{s}$, but the electromagnetic decay mode of the J/ψ is comparable to the strong mode, which increases its lifetime significantly.

[2] In general, the S-Wave states of this quarkonium family are denoted with $\psi(nS)$ with $\psi(1S) = J/\psi$.

[3] The production threshold for a $\tau^+\tau^-$ state lies at $2 \cdot m_\tau \approx 3553.72\,\mathrm{MeV/c^2}$, which is more than the J/ψ mass.

about the processes that occurred there. Particles that were not produced via weak decays are referred to as prompt.

- ▷ Feed-down from higher charmonium states: Higher charmonium states can decay into J/ψ, e.g., via $\chi_c \to J/\psi + \gamma$ or $\psi(2S) \to J/\psi + \pi^0 + \pi^0$. Feed-down contributions are considered as part of the prompt productions, because the lifetime of the higher charmonium states is not large enough to distinguish between directly produced J/ψ and those from higher state decays.

- ▷ Directly produced particles (Prompt): Gluon fusion processes predominantly drive the production of charmonium. They originate from the initial collision and carry the desired information of the relevant processes.

Prompt production mechanisms involve distinct energy scales. Because of the heavy quark mass of $m \approx 1.5\,\mathrm{GeV/c^2}$ and the typical momentum scale of $mv \approx 0.9\,\mathrm{GeV}$, the hadronization process into quarkonium can be treated non-relativistically. In contrast, the production of $c\bar{c}$ pairs can be accurately described via perturbation theory [41] by considering up to next-to-leading order (NLO) contributions. This separation of $c\bar{c}$ production and binding into a quarkonium state is called the factorization approach. Several models are currently available that predict quarkonium production cross-sections through various scenarios.

Color Evaporation Model

In the Color Evaporation Model (CEM), [42] one assumes that any heavy-quark pair with a mass below the open-heavy-quark threshold M_D has a certain probability of binding into a quarkonium state. This probability is independent of the initial state of the $Q\bar{Q}$ pair and is physically processed by emitting an infrared gluon, which carries any remaining color charge and hence *evaporate* the color. The production cross-section of a quarkonium state H in this scenario is given by

$$\frac{\mathrm{d}^3\sigma(H)}{\mathrm{d}P^3} = F_H \int_{2M_c}^{2m_D} \mathrm{d}M \, \frac{\mathrm{d}\sigma_{c\bar{c}}}{\mathrm{d}M \, \mathrm{d}^3P}. \tag{3.1}$$

F_H is called *hadronization factor* and is assumed to be universal among all possible kinematic and spin configurations of the quarkonium H, a strong predictive power of the CEM.
Further developments consider that cross-sections of different quarkonia do not show the same p_T dependence. The improved model places a constraint, where the invariant mass of intermediate $Q\bar{Q}$ states have to be larger than the mass of the produced quarkonium. Additionally, a momentum shift of the $Q\bar{Q}$ pair with respect to the quarkonium is introduced. It is named Improved Color Evaporation Model (ICEM) and provides a better description of J/ψ yields than the previous model [43].

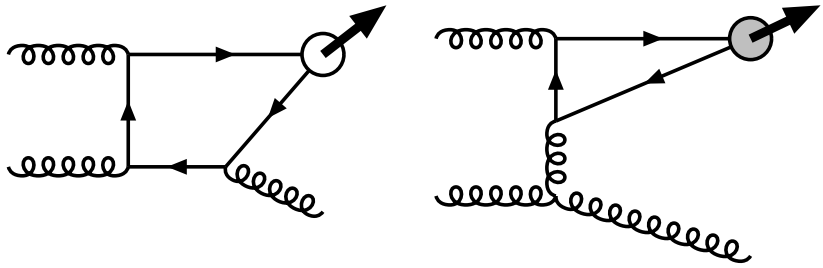


Figure 3.2: Left: Direct color singlet production of a J/ψ, Right: Color octet production diagram. [44]

Color Singlet Production

The Color Singlet Model (CSM) employs a perturbative approach to compute the cross-section of interactions that produce $Q\bar{Q}$ pairs. While the heavy quark pair can be produced in a singlet or octet configuration, this model only considers the production of color singlet states. At the LHC, these productions are mainly driven by gluon fusion, where the lowest-order contributions are shown in figure 3.2.
Transitions from a $c\bar{c}$ pair into quarkonium happen basically instantaneous and only depend on the radial wave function $R(0)$ for S-wave states like $\psi(nS)$ at the origin. The value of the wave-function can be extracted by measuring the branching ratio of a J/ψ decay into leptons, because $\Gamma(J/\psi \to e^+e^-) \propto |R(0)|^2$.
At lower collision energies, the CSM demonstrates good agreement with the measured data, but at higher energies, it underestimates the production cross-sections at high p_T.

Non-Relativistic QCD

To overcome the issues of the CSM, one must include color octet production mechanisms. This is naturally done in the NRQCD effective field theory, in which all relevant energy scales are factorized. Production cross-sections for producing a quarkonium H in this scenario only depend on the probability to create a heavy-quark pair with the quantum state $k = {}^{2S+1}L_j^{[c]}$. The cross-section can be written as follows:

$$\mathrm{d}\sigma\left(H\right) = \sum_k \mathrm{d}\sigma_k \left\langle \mathcal{O}_k^H \right\rangle . \tag{3.2}$$

Here, $\mathrm{d}\sigma_k$ is the pQCD cross-section and $\left\langle \mathcal{O}_k^H \right\rangle$ is the probability that a $Q\bar{Q}$ binds into a colorless quarkonium state. The transition probabilities $\left\langle \mathcal{O}_k^H \right\rangle$ are called *long-distance matrix elements (LDMEs)* and are assumed to be universal among all production processes. This universality allows the experimental determination of values and predictions for other collision energies or systems. Numerical values for LDMEs can be extracted e.g., from fits to experimental measurements of charmonium cross-sections or scaling of transverse momentum distributions. By

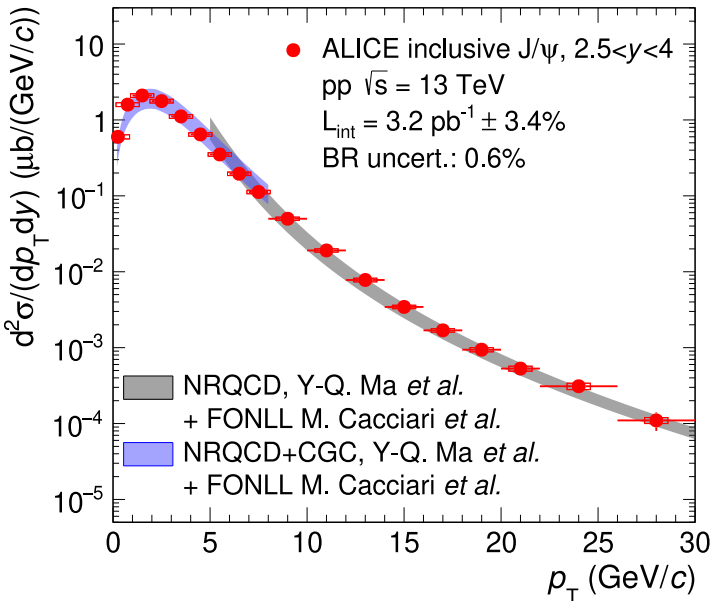


Figure 3.3: Production cross-section of inclusive J/ψ mesons at forward rapidity in pp collisions at $\sqrt{s} = 13\,\mathrm{TeV}$ as a function of transverse momentum, compared to predictions from Non-Relativistic Quantum Chromodynamics (NRQCD) and NRQCD + Color Glass Condensate (CGC) EFT's. [45]

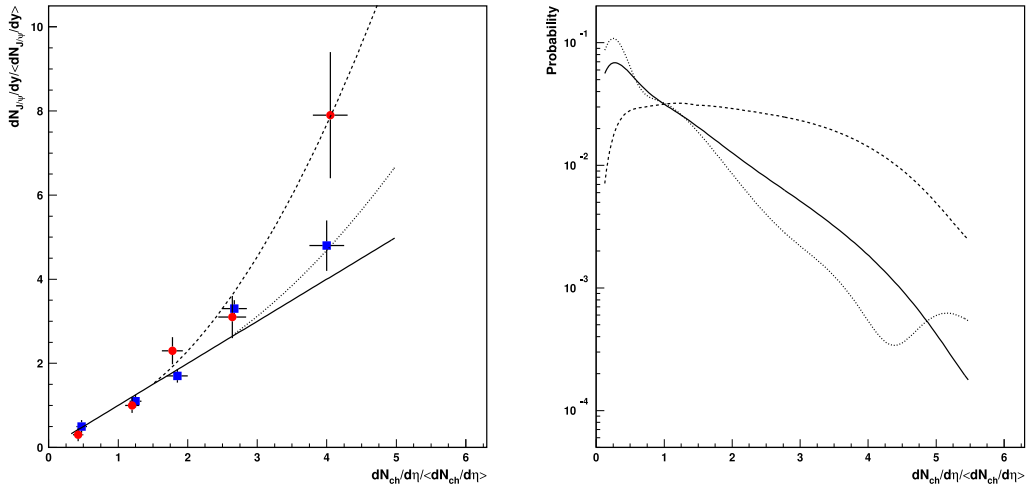
considering only $k = {}^{2S+1}L_j^{[1]}$, the CSM is reproduced. In all color octet configurations, a transition into colorless J/ψ states occur via the emission of a bremsstrahlung gluon. Figure 3.3 shows the production cross-section of J/ψ measured by ALICE in comparison to predictions from NRQCD.

3.2 Theoretical Models of the Multiplicity Dependence

In a naive interpretation of pp collisions as a sum of independent partonic scatterings one would expect a linear dependence between the number of produced J/ψ as a function of charged-particle multiplicity to increase. However, these expectations seemingly only hold for low-multiplicity events. As discussed in the next section 3.3, previous experimental results hint at a nonlinear behavior of the J/ψ yield as a function of multiplicity. This chapter discusses some currently available models for describing this nonlinear behavior.

Percolation Model

Production of particles in *pp* collisions is mainly driven by breaking color strings. In the *percolation model*, one assumes that these strings have a finite, non-zero, transverse size. Their effective number is reduced in regions with high string density compared to regions with low density. Since the production of particles like J/ψ is dominated by gluon fusion processes,



(a) (b)

Figure 3.4: (a) Self-normalized J/ψ yield as a function of the self-normalized multiplicity. The dashed line is the prediction of the percolation model in $|y| < 0.9$ and the dotted line in $2.5 < y < 4$ compared to measurements of the ALICE collaboration. (b) Minimum-bias $P(N_{\text{ch}})$ distribution from experimental data (solid line) compared to the percolation model (dashed line) and PYTHIA (dotted line). [46]

which can be effectively modeled as color strings, the number of produced J/ψ mesons $N_{J/\psi}$ is directly proportional to the number of strings N_S. However, the number of charged particles produced per unit pseudorapidity region, $\mathrm{d}N_{\text{ch}} / \mathrm{d}\eta$, depends linearly on N_S but experiences damping, described by a factor $F(\rho)$, due to the surrounding color charges. Here, $\rho = \frac{N_S \sigma_0}{\sigma}$ is the string density as a function of N_S, the transverse area of a string σ_0 and the transverse area of the collision σ. With μ_1 being the average number of charged-particles produced by one string, the multiplicity can be expressed as follows:

$$\mathrm{d}N_{\text{ch}} / \mathrm{d}\eta = F(\rho) N_S \mu_1, \quad \text{where} \quad F(\rho) = \sqrt{\frac{1 - e^{-\rho}}{\rho}}. \tag{3.3}$$

Considering the relative value of $N_{J/\psi}$ and N_S and divide them by their averages over a significant number of events, where $n_{J/\psi} = \mathrm{d}N_{J/\psi} / \mathrm{d}y \,/\, \langle \mathrm{d}N_{J/\psi} / \mathrm{d}y \rangle$ and $n_s = N_S / \langle N_S \rangle$, one finds the equation $n_{J/\psi} = n_s$. Combining the above equations by plugging in the expressions for $F(\rho)$ as well as $\langle \rho \rangle = n_{J/\psi} \cdot \rho$, gives a functional dependence of the self-normalized J/ψ yield and the self-normalized charged-particle yield

$$n_{\text{ch}} = n_{J/\psi}^{1/2} \left[\frac{1 - \exp\left(-n_{J/\psi} \langle \rho \rangle\right)}{1 - \exp(-\langle \rho \rangle)} \right]^{1/2}. \tag{3.4}$$

For lower multiplicities, the string density is small and the expression can be approximated as $n_{\mathrm{ch}} = n_{J/\psi}$, thus showing a linear dependency. At higher multiplicities, where $\langle\rho\rangle \gg 1$, the bracket can be approximated as $\langle\rho\rangle^{-1/2}$ which leads to $n_{J/\psi} = \langle\rho\rangle\, n_{\mathrm{ch}}^2$, and thus a quadratic dependency. Combining these equations yields

$$n_{J/\psi} = (1 - \langle\rho\rangle) n_{\mathrm{ch}} + \langle\rho\rangle\, n_{\mathrm{ch}}^2. \tag{3.5}$$

An accurate description of the increase of J/ψ production as a function of multiplicity is provided by the percolation model, as it can be seen in figure 3.4 (a). The model was introduced by E.G. Ferreiro and C. Pajares for J/ψ in 2012 in [46] and for open charm hadrons in 2015 in [47].

Higher Fock States Model

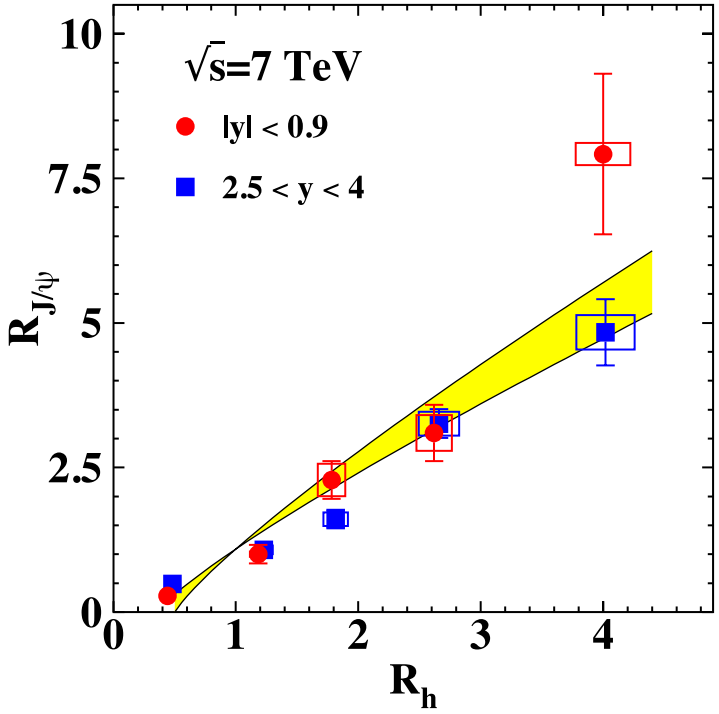


Figure 3.5: Prediction of the multiplicity dependence of J/ψ production from the Higher Fock States Model compared to data from ALICE at mid- and forward rapidity at $\sqrt{s} = 7\,\mathrm{TeV}$. [48]

In p–A collisions, the proton interacts multiple times with nucleons inside a nucleus with mass number A. Each of these interactions involves gluon exchange, resulting in a gluon-rich proton configuration that enhances the likelihood of gluon fusion processes. The higher Fock states model constructs a relation between p–A and pp collisions. In the latter case, rare events occur with a substantial amount of charged-particles produced, several times higher than the average multiplicity. These events are attributed to protons whose wave function includes components

with a large amount of gluons, the *higher Fock states*. Additional gluons lead to more charged final-state particles and an extended amount of charmonium.
To capture this mathematically, one first defines the ratio of the average hadron multiplicities per rapidity in p–A, as well as in pp collisions as $R_h^{pA} \equiv \left\langle \mathrm{d}N_h^{pA} / \mathrm{d}y \right\rangle / \langle \mathrm{d}N_h^{pp} / \mathrm{d}y \rangle$. This ratio scales with the number of collisions N_{coll}[4] like $R_h^{pA} = 1+\beta(N_{\text{coll}}-1)$. The parameter β considers the difference from solely N_{coll} scaling due to cold nuclear matter effects. On the other hand, the ratio of the average J/ψ yield $R_{J/\psi}^{pA} = \left\langle \mathrm{d}N_{J/\psi}^{pA} / \mathrm{d}y \right\rangle / \left\langle \mathrm{d}N_{J/\psi}^{pp} / \mathrm{d}y \right\rangle$ scales as a function of N_{coll} like $R_{J/\psi}^{pA} = N_{\text{coll}} A^{\alpha-1}$, with α being a parameter that depends on the collision energy and the rapidity. Within a geometrical approach, N_{coll} can be approximated by the geometric cross-section of inelastic pp collisions $\sigma_{\text{inel}}^{pp}$ as $N_{\text{coll}} \approx \sigma_{\text{inel}}^{pp} A^{1/3} / \pi r_0^2$. Combining these equations leads to the following:

$$R_{J/\psi}^{pA} = \left(\frac{R_h^{pA} - 1}{\beta} + 1 \right)^{3\alpha-2} \left(\frac{\sigma_{\text{inel}}^{pp}}{\pi r_0^2} \right)^{3(1-\alpha)} . \tag{3.6}$$

The higher Fock states model now relates this equation, which was derived for p–A collisions, to the case of high-multiplicity and minimum-bias pp collisions

$$R_h^{pA} \leftrightarrow R_h^{pp} \equiv \mathrm{d}N_h^{pp} / \mathrm{d}y / \langle \mathrm{d}N_h^{pp} / \mathrm{d}y \rangle$$
$$R_{J/\psi}^{pA} \leftrightarrow R_{J/\psi}^{pp} \equiv \mathrm{d}N_{J/\psi}^{pp} / \mathrm{d}y / \left\langle \mathrm{d}N_{J/\psi}^{pp} / \mathrm{d}y \right\rangle$$

This model [48] created by B. Z. Kopeliovich, H. J. Pirner, I. K. Potashnikova, K.Reygers and I. Schmidt showed good agreement between the prediction and the data, as shown in figure 3.5.

Color Glass Condensate

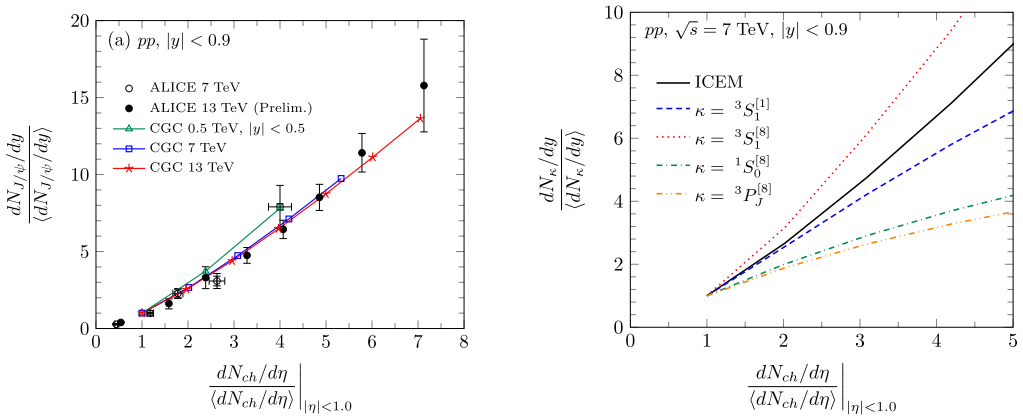
The outcome of an event depends heavily on the incoming protons' initial state before the collision. At LHC energies, this initial state can be described by an EFT, called the CGC. Looking at the PDF, introduced in chapter 2, one finds that the gluons dominate the proton composition at small-x. This is caused by a process called gluon splitting, where a single gluon can radiate one or more gluons, increasing its number rapidly. Gluon splitting itself is a consequence of the gluon self-interaction in QCD and occurs when the proton is probed, where the virtual gluons in this splitting process become observable particles. At a certain number, the amount of gluons does not increase further, and they start to overlap in the phase space[5], which is finite. Overlapping gluons recombine via inverse gluon splitting. This natural limit to the number of gluons in the initial state of the protons is called *gluon saturation*. At a certain saturation scale Q_s, the number of gluons does not increase anymore, but only their density becomes larger.

[4] This *number of collisions* has to be taken in the sense of produced parton showers by the partonic interactions of the proton components with the nucleus.
[5] The phase space is spanned over several observables, primarily the Bjorken-x, transverse momentum p_{T}, spatial separation r and rapidity y.

As described in section 3.1, the main production mechanism for J/ψ is via the $gg \to J/\psi + X$ process. In the CGC approach, the cross-section can be described in pp collisions via [49]

$$\mathrm{d}\sigma_k \propto \int \mathrm{d}x_1\, \mathrm{d}x_2\, f_g(x_1, Q^2) f_g(x_2, Q^2)\, \mathrm{d}\sigma^k_{gg\to c\bar{c}}\,. \tag{3.7}$$

Here, $f_g(x_i, Q^2)$ is the gluon PDF of the respective proton $i = 1, 2$ at the momentum scale Q^2 and x_i is the momentum transfer integrated over the entire phase space. The $\mathrm{d}\sigma^k_{gg\to c\bar{c}}$ are the values of the pQCD cross-sections for the color singlet and octet productions. To calculate the entire J/ψ cross-section, this expression for $\mathrm{d}\sigma_k$ can be used as an input for models that describe the production of charmonium states like NRQCD or the ICEM. Both approaches agree well with the currently available data, as shown in figure 3.6. Within the CGC + NRQCD approach, the different production channels show a versatile multiplicity dependency, which provides the possibility to extract the LDMEs from such multiplicity measurements of J/ψ production. This model was introduced 2018 by Ma, Tribedy, Venugopalan, and Watanabe in [50].



(a) (b)

Figure 3.6: (a) Model prediction of full CGC + ICEM at $\sqrt{s} = 0.5\,\mathrm{TeV},\ 7\,\mathrm{TeV}$ and $13\,\mathrm{TeV}$ in mid-rapidity compared to data from the ALICE experiment at $7\,\mathrm{TeV}$ and $13\,\mathrm{TeV}$ (b) Multiplicity dependence of different production channels and the pure ICEM model. [50]

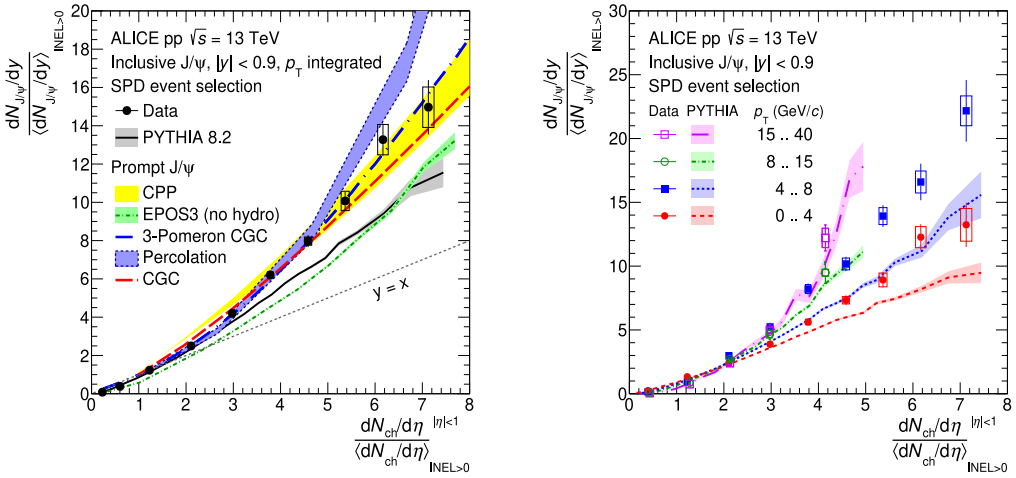
PYTHIA Event Generator

The *PYTHIA* model is historically based on the Lund string model [51] which describes hadronization of partons after a high-energetic particle collision. This model is implemented in a general purpose Monte-Carlo event generator with the same name, originally developed at the University of Lund [52]. In its current version 8.3, PYTHIA implements a complex physical behavior that can treat various processes, from basic hadronization to Beyond Standard Model (BSM) physics. To generate events, PYTHIA relies on both well-understood theoretical derivations of processes and phenomenological models with free parameters, which must be chosen via comparison with

data. These parameters are set in a so-called *tune*, which the user can choose from a wide variety of available tunes. The default is called *Monash 2013* and uses data from HEP-DATA and the PDG, produced by experiments like Large Electron-Positron Collider (LEP), the Tevatron, and LHC to generate minimum-bias events for general purpose studies in particle physics.
An event is generated in a time-ordered way from processes with the shortest timescale, or largest energy, to longer timescales. A collision begins with the initial hard scattering of two partons from the incoming hadrons into outgoing particles. The selection of these partons is based of the PDF's of the collision partners, and kinematics are based on calculations from perturbation theory. From such hard scatterings, short-lived resonances like the Z or $W^{\pm}$ bosons or the top quark may occur, which will decay first. Initial-state radiation, composed of quarks and gluons, is emitted prior to the scattering process and modifies the resulting kinematics. Similarly, the final state radiation emitted by the outgoing partons of the hard scattering can lead to jets. Both types of radiation are collectively referred to as parton showers and constitute an additional source of heavy-flavored $Q\bar{Q}$ pairs in PYTHIA. Within this model, the partons may interact with each other several times, which are commonly named as MPI. Some partons may remain in a colored state after the interaction when they did not participate in the interaction. These are called beam remnants and may form hadrons or serve as endpoints of strings in the upcoming reconnection process. In the event, strings are rearranged between the partons, which reduces the total string length and total multiplicity, because the abundance of particles is created via the string breaking mechanism in the Lund string model. This rearrangement is called CR.
In general, the production of quarkonium in PYTHIA is governed by the NRQCD framework. Additional quarkonium may be produced via CR of remnant quarks in the beam. Creating heavy-quark pairs via string breaking is theoretically possible but strongly suppressed and thus neglected in PYTHIA. However, charmonium states may have been produced via the reconnection of formerly independent c and $\bar{c}$ quarks with very short string lengths. When this string length is too short, the potential energy is not large enough to produce new $q\bar{q}$ pairs and instead the heavy quark pair directly hadronizes into a quarkonium. This production mechanism is named *cluster collapse*.
First, the stronger-than-linear increase of the J/ψ yield with the event multiplicity was assumed to be attributed to a combination of MPI and CR and auto-correlation effects. Auto-correlation in this sense means, that an artificial correlation between the J/ψ yield and the multiplicity arises. Several causes can lead to the observed auto-correlation effects. The first reason is that the J/ψ were reconstructed via their decay into e^+e^- pairs, which means that two additional charged-particles may enter the multiplicity. Additionally, when a $c\bar{c}$ pair is created in the color-octet channel, the hadronization requires the emission of an additional gluon, which may produce charged particles. For a J/ψ produced via cluster collapse, the individual c ($\bar{c}$) quarks were initially produced with other charm quarks, which may be rearranged into charged hadrons and thus enter the multiplicity. Lastly, although the decays of beauty hadrons may produce J/ψ, but often other particles that decay further into more charged-hadrons.

Removing the auto-correlation in PYTHIA by measuring the multiplicity in different azimuthal regions to the J/ψ shows that the auto-correlations are the only cause for the stronger-than-linear increase the J/ψ yield with multiplicity [53]. MPI and CR cannot be the cause of the increase in PYTHIA.

3.3 Experimental Status of Charmonium Production as a Function of Multiplicity



(a) (b)

Figure 3.7: (a) Multiplicity dependence of inclusive J/ψ production at mid-rapidity in pp collisions at $\sqrt{s} = 13\,\mathrm{TeV}$ in comparison to several theoretical predictions. (b) Multiplicity dependence of J/ψ production in four p_T bins in comparison to predictions from PYTHIA8.3. [1]

The first measurements of the event-activity dependencies of charm production were performed by the NA27 at CERN and published in 1988 [54]. The average charged-particle multiplicity in events with open charm hadrons[6] was found to be $20\,\%$ larger than in events without. Additionally, the shape of the $P(N_\mathrm{ch})$ distribution becomes narrower when only considering events with open charm hadrons. The ALICE collaboration performed first such measurements in pp collisions at $\sqrt{s} = 7\,\mathrm{TeV}$ for J/ψ produced at forward ($2.5 < y < 4.0$) and mid-rapidity ($|y| < 0.9$) and later at mid-rapidity at $\sqrt{s} = 13\,\mathrm{TeV}$, with the latter results shown in figure 3.7 (a). The self-normalized J/ψ yield increases stronger-than-linear when the signal and multiplicity are measured at mid- and forward rapidity, respectively, in the same region. In contrast to that, figure 3.8 shows that a linear increase is observed at $\sqrt{s} = 5.02\,\mathrm{TeV}$, when the J/ψ signal is measured in mid-rapidity and the multiplicity in the forward rapidity range (blue boxes). At $\sqrt{s} = 13\,\mathrm{TeV}$, a

[6] Particles that contain a charm quark and have a non-zero net charmness are called open charm. For examples, the D^0 meson with the quark content $c\bar{u}$ as the lightest open-charm hadron. Charmonium, like the J/ψ, are called hidden charm, because they have zero charmness, albeit being composed only of charm quarks.

slightly stronger-than-linear increase is observed when the J/ψ signal is measured in the $\mu^+\mu^-$ decay channel at forward rapidity and the multiplicity is measured in mid-rapidity (green boxes) [55]. Previously, measurements in the different rapidity regions showed a different multiplicity

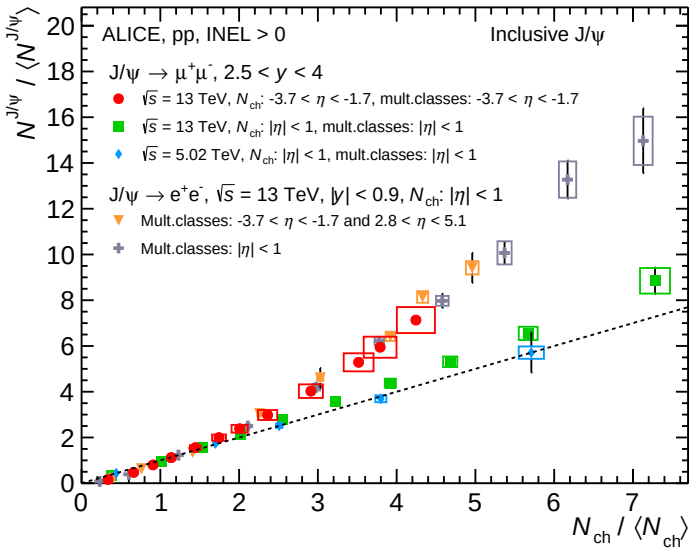


Figure 3.8: Multiplicity dependence of J/ψ production in pp collisions at $\sqrt{s} = 13\,\mathrm{TeV}$ for the $\mu^+\mu^-$ decay channel with multiplicity estimators in different regions of rapidity. [55]

dependence. This could now be attributed to the effect of autocorrelations in the regions. In figure 3.8, no significant difference in the dependence in the rapidity channels is observed anymore. In these measurements, the decay daughters (here the $\mu^+\mu^-$ pair) are removed from the multiplicity estimation, thus removing a large fraction of the auto-correlations.

To experimentally subtract the auto-correlation effects, it was proposed in [53] to measure the multiplicity in different azimuthal regions with respect to the J/ψ flight direction. In this study, it was found that the stronger-than-linear increase is entirely attributed to the auto-correlations effects. PYTHIA 8 does not include any additional effects, such as overlapping strings or a CGC.

At the time of writing this thesis, the ALICE collaboration is performing an analysis that disentangles the prompt and non-prompt components of J/ψ production and performs the experimental study within the azimuthal regions as described in [53]. Preliminary results of this analysis are shown in chapter 6.

Earlier analyses also investigated the p_T dependence of the inclusive J/ψ yield versus multiplicity. The increase is stronger with higher p_T, see figure 3.7 (b). This effect can be attributed to an increased chance for MPI with higher p_T.

4 Experimental Setup and Methods

This chapter describes the utilized experimental apparatus, starting with the LHC and followed by the ALICE detector, and its sub-detectors. An elucidation of the most important experimental methods concerned with this analysis concludes the chapter.

4.1 The Large Hadron Collider

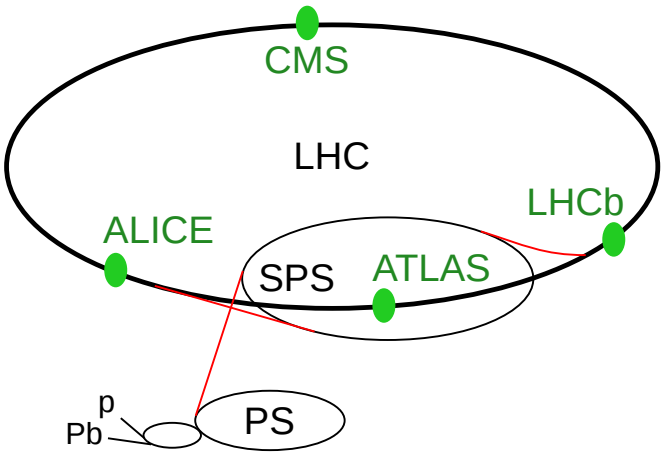


Figure 4.1: Accelerator complex at CERN showing the LHC, the pre-accelerators Proton Synchroton (PS) and SPS and the four main experiments. Adopted from [56]

Up to now, CERN in Geneva hosts the largest particle accelerator built, called LHC. In its current run 3, it reaches a collision energy of up to $\sqrt{s} = 13.6\,\mathrm{TeV}$ in pp collisions and $\sqrt{s_{\mathrm{NN}}} = 5.36\,\mathrm{TeV}$ in Pb–Pb collisions. In earlier runs, p–Pb and Xe–Xe collisions were also performed. The ring collider itself has a circumference of $26.7\,\mathrm{km}$ and is hosted in the tunnel that was used by the LEP before its decommissioning. Several pre-accelerators are used to inject the desired collision partners. Figure 4.1 visualizes the accelerator complex at CERN.
Run 1, being the first LHC operational period, began in 2009 and finished 2013. During this period, a major goal in physics was achieved. In 2012, the A Toroidal LHC Apparatus (ATLAS) and Compact Muon Solenoid (CMS) collaborations published the discovery of the Higgs boson, up to this date the last missing particle in the SM. Peter Higgs and François Englert were awarded

the Nobel Prize in physics in 2013 for predicting the Higgs boson.
After a maintenance phase from 2013 to 2015, called Long Shutdown 1, a second run period was initiated with an upgraded collider and improved detectors. During run 2, a collision energy of $13\,\mathrm{TeV}$ was reached in pp collisions and $5.02\,\mathrm{TeV}$ in Pb–Pb collisions. In addition, Xe ions were delivered to the LHC for a short time. Run 2 ended in 2018, and a second maintenance and upgrade period, Long Shutdown 2, began and concluded in 2022. The third and currently ongoing data-taking period started afterward and will last until 2026. During the four-year shutdown, major upgrades were implemented to the LHC and the experiments to enable interaction rates of $200\,\mathrm{kHz}$ up to $1\,\mathrm{MHz}$ in pp collisions and $50\,\mathrm{kHz}$ in Pb–Pb collisions, corresponding to an increase of a factor of 50 compared to run 2.
CERN operates seven experiments at the LHC, with four large, general purpose detectors and dedicated physics goals, and three smaller and specialized experiments:

- ATLAS (**A Toroidal LHC ApparatuS**) [57] is the largest experiment and currently the largest detector ever built. It is a general-purpose detector that is designed for measurements of the Higgs boson properties and searches for physics beyond the standard model.
- CMS (**Compact Muon Solenoid**) [58] is the second-largest experiment and follows similar physics goals as ATLAS, but with a different detector approach.
- ALICE (**A Large Ion Collider Experiment**) [59] is the third-largest general-purpose detector designed for the study of heavy-ion collisions, especially the properties of the QGP. A detailed description is given in section 4.2.
- Large Hadron Collider beauty (LHCb) (**Large Hadron Collider beauty**) [60] is the smallest of the four large experiments focusing on the study of CP violation in heavy-flavored hadrons.

Located inside the caverns of the larger experiments, Total Elastic and diffractive cross section measurement (TOTEM) [61], Large Hadron Collider forward (LHCf) [62], and Monopole and Exotics Detector at the LHC (MoEDAL) [63], complete the LHC detector family.

4.2 A Large Ion Collider Experiment

ALICE is a large experiment at the LHC, being a general-purpose detector specialized to study heavy-ion collisions with a good capability to track particles over a broad kinematic range. A schematic view of the detector is given in figure 4.2. Subdetectors are placed inside a giant solenoid magnet, called L3, creating a homogenous magnetic field of up to $0.5\,\mathrm{T}$. Tracks of charged-particles are bent through the magnetic field, enabling momentum and charge measurements within ALICE *central barrel*, that consists of Inner Tracking System (ITS), Time Projection Chamber (TPC), Transition Radiation Detector (TRD), Time-of-flight Detector (TOF), Electromagnetic Calorimeter (EMCal), Photon Spectrometer (PHOS), Di-jet Calorimeter (DCal), and High Momentum Particle Identification (HMPID). Additional forward detectors are used for

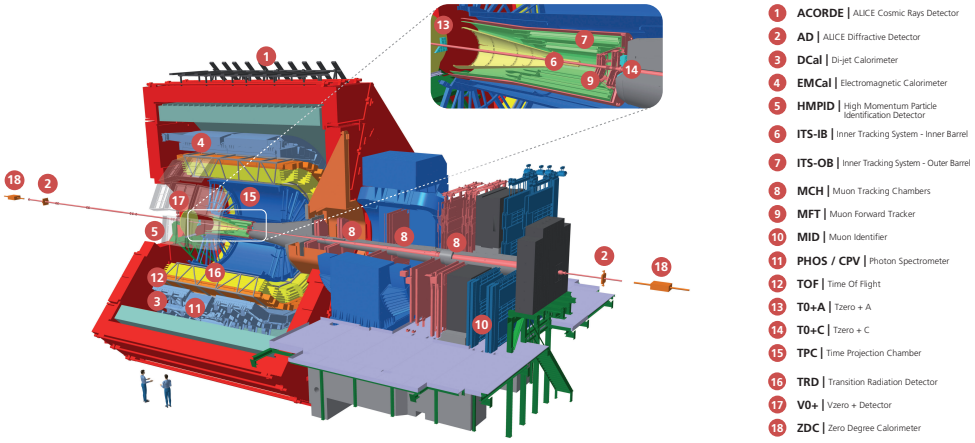


Figure 4.2: Schematic picture of the current run 3 ALICE detector setup with an overview of the installed sub-detectors and their location inside the detector. [64]

dedicated purposes: Fast Interaction Trigger (FIT), consisting of FT0, FV0, and FDD, are the main triggering and luminosity monitoring devices. Muon tracking in the forward region is provided by three dedicated detectors: Muon Tracking Chamber (MCH), Muon Forward Tracker (MFT), and Muon Identifier (MID). Covering the backward and forward region, ALICE Diffractive Detector (AD) and Zero Degree Calorimeter (ZDC) are placed along the beam-line outside the detector, selecting diffractive events, and measuring the energy of forward particles. Above L3, ALICE Cosmic Rays Detector (ACORDE) is positioned to detect high-energy cosmic radiation.

4.2.1 Inner Tracking System

ITS [65] is the innermost detector of ALICE central barrel, directly positioned around the beam pipe. Seven cylindrical layers of Monolithic Active Pixel Sensors (MAPs) with the first three layers, called Inner Barrel (IB), having a length of $271\,\mathrm{mm}$ and a radial position ranging from $22.4\,\mathrm{mm}$ to $42.1\,\mathrm{mm}$ around the beam pipe, cover a pseudorapidity range of $|\eta| < 2.0$. All remaining layers are called Outer Barrel (OB) with a length of $1475\,\mathrm{mm}$ and a radial position of $194.4\,\mathrm{mm}$ to $394.9\,\mathrm{mm}$, covering a range of $|\eta| < 1.3$. In total, ITS covers a transverse momentum range from $0.05\,\mathrm{GeV/c}$ to $20.0\,\mathrm{GeV/c}$ with a material budget of $0.3\,\%X_0$ in the IB and $0.8\,\%X_0$ in the OB.

The main purposes of the ITS are: precise determination of the PV[1] with a resolution of up to $100\,\mu\mathrm{m}$, secondary vertex reconstruction for charm and hyperon decays, charged-particle tracking, and improvement of the TPC momentum and angular resolution.

[1] A vertex is a distinct point in space where particles interact. In this sense, a primary vertex is the initial interaction point of the event. Secondary vertices occur when particles decay into charged hadrons.

4.2.2 Time Projection Chamber

The TPC [66] is ALICE main tracking and Particle Identification (PID) device, capable of performing a three-dimensional reconstruction of tracks produced by charged particles. It has a cylindrical volume of $90\,\mathrm{m}^3$ with a length of $5\,\mathrm{m}$ that covers $|\eta| < 0.9$ in pseudorapidity. The detector volume is filled with a Ne–CO_2–N_2 gas mixture of a $90{:}10{:}5$ composition[2], separated by a central electrode in the axial center. Along the z-Axis, a uniform electric field is applied, ranging from the central electrode to both end plates, which are themselves divided into 18 sectors, each consisting of two inner and outer readout chambers.
When charged-particles traverse the gas, they ionize Ne atoms, leaving free electrons in the volume. The electrons drift with a constant velocity of $2.58\,\mathrm{cm}\,\mu\mathrm{s}^{-1}$ toward the readout chambers, where their ionization signal is amplified via Gas Electron Multipliers (GEMs). Drift electrons exhibit an avalanche effect, which can be detected as a current. During an avalanche, ultraviolet radiation is emitted that causes further ionization in the active TPC gas. A quenching mixture of CO_2 and N_2 is used that absorbs secondary photons to prevent such radiation.
A total of 3276 Front-End Cards (FEC) are used to read the signal, where each card consists of 160 front-end channels. Over these front-end channels, a total of 524160 pads are distributed that form the GEM chambers anode plane. The collected detector hits are transformed into semi-Gaussian voltage signals and digitized for further processing. This method provides capabilities for 3D flight path reconstruction of particles. The peak voltage of a signal from a readout pad is proportional to the local energy loss of the tracked particles. Using reconstructed track information, one can extract the energy loss per path length $\mathrm{d}E\,/\,\mathrm{d}x$ of particles as a function of velocity β, and thus perform PID via comparison of measured energy loss signals with an expected Bethe-Bloch signal, determined by equation (2.13).

4.2.3 Time-of-Flight Detector

The TOF [67] detector encapsulates the TRD at a distance of around $3.7\,\mathrm{m}$ from the nominal interaction point. Employing an active area of $141\,\mathrm{m}^2$ and pseudorapidity coverage of $|\eta| < 0.9$, it is used to measure the time a particle needs to travel from the PV to the TOF detector, allowing for precise velocity measurements of tracked particles. Including momentum information of the particle, e.g., from the TPC, one can specify the particle mass via $\beta\gamma = p/(mc)$, thus identifying particles. This PID procedure works particularly well at intermediate momentum ranges, where the time of flight of different particle species differs the most. At higher momenta, particles move closer to the speed of light, resulting in indistinguishable flight times for different particle species. ALICE TOF consists of 1593 Multigap Resistive Plate Chambers (MRPCs) with an active area of $888\,\mathrm{cm}^2$, which are divided into 18 azimuthal sections. The MRPCs detects charged particles using multiple thin gaps filled with gas between resistive electrodes. Electron avalanches create fast, localized signals with a time resolution of $\sigma_{\mathrm{TOF}} \approx 68\,\mathrm{ps}$ in run 3 [68].

[2] The numbers do not refer to a percentage of the gas in the mixture but rather refers to relative parts per unit volume.

4.2.4 Fast Interaction Trigger

The FIT [69] consists of three sub-detectors: FT0, FV0, and FDD. In total, FIT provides minimum bias triggering information and measures luminosity, as well as a precise collision time to calculate an initial indication of the PV z position.

FT0 involves two arrays of quartz Cherenkov radiators coupled to microchannel plate photomultipliers that detect Cherenkov light produced by traversing particles. These plates are positioned at opposite sides of the nominal interaction point. FT0-A covers a pseudorapidity range of $3.8 < \eta < 5.0$ and is placed $3.3\,\mathrm{m}$ away from the nominal interaction point in the forward direction. FT0-C is placed just $0.8\,\mathrm{m}$ away from the nominal interaction point and covers a pseudorapidity range of $-3.4 < \eta < -2.3$. Such asymmetric positioning is a result of the spatial constraints placed on the detector by the existing infrastructure for other detectors and previous experiments. Despite these constraints, FT0 achieves a one-MIP time resolution of about $25\,\mathrm{ps}$ and provides timing information for minimum bias triggering and acts as a multiplicity counter.

FV0 is a plastic scintillator disk divided into five concentric rings with an outer circumference of $144\,\mathrm{cm}$. It is positioned in the forward direction at a distance of $3.2\,\mathrm{m}$ with a coverage of $2.2 < \eta < 5.1$ and encapsulates the FT0-A detector, which has a one-MIP time resolution of $200\,\mathrm{ps}$ and provides additional minimum bias trigger information and monitors the luminosity.

FDD consists of two nearly identical scintillator pads with an active volume of $977\,\mathrm{cm}^3$, placed on opposite sides of the interaction point. FDD-A is positioned in the forward direction at a distance of $17\,\mathrm{m}$ and FDD-C is positioned in the backward direction at $19.5\,\mathrm{m}$ distance. They cover a very narrow pseudorapidity range of $4.7 < \eta < 6.3$ and $-6.9 < \eta < -4.9$ and are used to measure diffractive cross-sections and ultra-peripheral collisions, as well as to monitor the beam-quality.

4.3 Tracking and Vertex Reconstruction

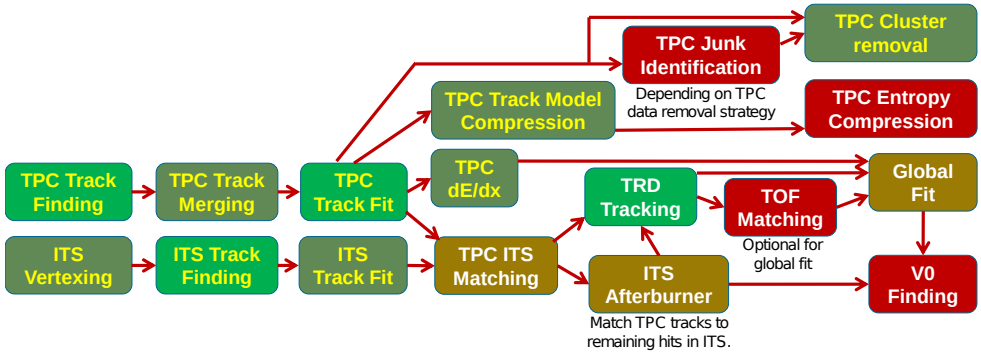


Figure 4.3: Global track reconstruction procedure in run 3. Adopted from [70]

The physical properties of the particles are measured by determining the properties of the tracks inside the detector. A central reconstruction algorithm was applied during earlier runs, employing a Kalman filter approach for track finding and fitting. Several steps must be performed to find all tracks and vertices in an event. A detailed explanation of the procedure is given in [71]. This reconstruction strategy relied on the triggered read-out of all detectors. However, this procedure is not applicable anymore in run 3 due to the different detector readout environments. Instead of a triggered read-out, ITS, TPC, TOF, and ZDC are operated in a continuous data-taking mode without hardware triggers. A continuous readout mode is mandatory to process all the information due to the increased interaction rates.
The new procedure starts with a preliminary vertex reconstruction in the ITS by clustering tracklets in the IB and extrapolate them back to the assumed vertex. Subsequently, the short track segments are clustered into ITS tracks, which are then fitted to obtain the track parameters. Simultaneously, track finding, merging, and fitting in the TPC is performed. When standalone track reconstruction in both detectors is performed, the tracks are matched from ITS to TPC. A global fit over the entire reconstructed track is performed after all individual track segments are matched between the detectors. With information from the last step, the PV can be reconstructed and secondary vertices are found by propagating tracks back to their origin. Additionally, PV reconstruction using ITS and TPC matched tracks is assisted by the FT0 detector by measuring the arrival time in both sides FT0-A and C and calculating $z = c \cdot |t_A - t_B|/2$. Figure 4.3 shows an overview of the entire global track reconstruction procedure.
In addition to the new track reconstruction procedure, the continuous data-taking mode imposes several new challenges for data analysis. Instead of distinct events, data is stored in several so-called Heart Beat Frames (HBFs), where two consecutive heart beats (also called ORBIT) mark the beginning and end of one (arbitrarily sized) data sample. The time of one orbit is typically determined at the software level. A typical duration from one beat to the next is $89.4\,\mu\mathrm{s}$. HBFs are determined at the level of the Front-End Readouts of the detectors and are entirely independent of ongoing physical processes. All data from heart beat frames are further processed by the First-level processor (FLP), which groups ≈ 256 consecutive heart beats from one FLP into Sub-Time Frames (STFs). This data is passed to several Event Processing Nodes, where the online track reconstruction is performed as described above. All STFs from all FLPs of one period are stored into Time Frames (TFs), with one TF containing again approximately 256 heart-beat frames. The concept is visualized in figure 4.4.

4.4 Track to Collision Association

At an interaction rate of $500\,\mathrm{kHz}$, collisions occur approximately every $2\,\mu\mathrm{s}$. One HBF contains on average 45 collisions. Even though the readout of the detectors is much faster, there is still an overlap of tracks to which collision they might belong. To solve this issue, the approximate time of detector crossing t_{track} and collision time t_{coll} is stored for each collision. At the analysis level, a so-called track-to-collision-association is performed, which uses previously stored

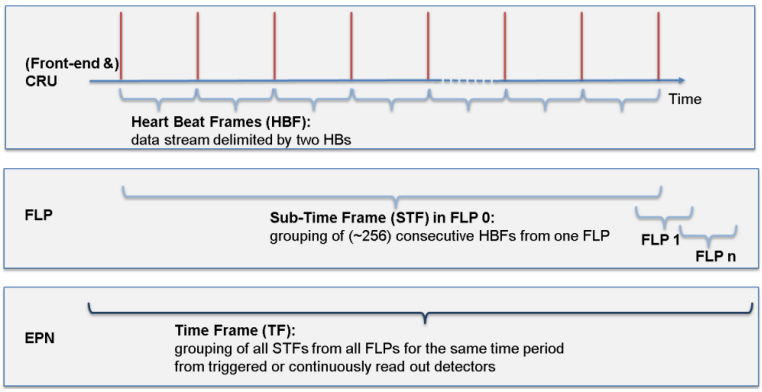


Figure 4.4: Description of division of the continuous read data into HBFs, STFs, and TFs. [72]

timing information to reject incompatible collisions. One loops over all tracks and collisions to reject for each track every collision candidate outside a predefined time window and different Bunch Crossings (BCs) [3]. Subsequently, one loop is made over all remaining collisions, and for each collision, every track produced inside a possible time window, is investigated.

Let $\mathrm{BC}_{\mathrm{track}} = N_{\mathrm{BC}} + t_{\mathrm{track}}/t_{\mathrm{spacing}}$ be the index of a BC of tracks in the middle of readout frames and $\mathrm{BC}_{\mathrm{coll}}$ the index of the BC of the collision. Here, N_{BC} is the BC index and $t_{\mathrm{spacing}} = 24.95\,\mathrm{ns}$ is the time between two BCs in ns. If $|\mathrm{BC}_{\mathrm{track}} - \mathrm{BC}_{\mathrm{coll}}| < C$, collisions are considered time-compatible. $C = n\Delta\mathrm{BC}_{1\sigma} + \tau/t_{\mathrm{Bunch}}$ is a user-defined constant that depends on several values. An allowed BC time interval accepted for 1σ of the Gaussian distributed time resolution, called $\Delta\mathrm{BC}_{1\sigma}$ is introduced, with a possibility to select broader BC time compatibility windows by changing n. The time margin τ that an analysis wants to allow for compensates for uncertainties in time measurements caused by uncalibrated TPC values. Default values for these parameters are $\Delta\mathrm{BC}_{1\sigma} = 60$, $n = 4$ and $\tau = 0.0$. A time margin is not necessary during this analysis because only calibrated data is used.

If more than one time-compatible collision is found, further steps are needed. To associate a track to its correct collision, the difference in track time t_{track} at the middle of the BC and the collision time t_{coll} is calculated by defining $t_{\mathrm{track,\,BC}} = t_{\mathrm{track}} + N_{\mathrm{BC}} \cdot t_{\mathrm{Bunch}}$. When $|t_{\mathrm{track,\,BC}} - t_{\mathrm{coll}}| < T$, the collision is considered compatible. If more than one compatible collision is found with this procedure, the collision with the lowest Δt is considered the correct collision.

T depends on whether the track time error is box-like or Gaussian distributed. Detectors that perform tracking inside of readout frames, such as ITS, exhibit box-like time uncertainties. In this case, the track time uncertainty is defined as $\sigma_{\mathrm{track,\,box}} = (\Delta t_{\mathrm{ROF}} \cdot t_{\mathrm{track}})/2$, where Δt_{ROF} is the duration of the Read-out Frame (ROF). For other detectors, the time resolution is Gaussian distributed, and the uncertainty is the standard deviation $\sigma_{\mathrm{track,\,gaus}}$ of this distribution. One defines the threshold T via

[3] In the LHC, protons are delivered within larger packages, so-called bunches, with each containing on average $10^1 1$ protons. Bunch crossing refers to the passage of two bunches.

- ▷ Box-like uncertainty: $T = \sigma_{\text{track, box}} + n\sigma_{\text{coll}} + \tau$
- ▷ Gaussian-like uncertainty: $T = n\sqrt{\sigma^2_{\text{track, gaus}} + \sigma^2_{\text{coll}}} + \tau$.

Here, n and τ are both user defined variables from the previous step and σ_{coll} is the standard deviation of the (always) Gaussian distributed collision time resolution. Ambiguous tracks may still be possible, depending on the chosen values.

4.5 Particle Identification

ALICE sub-detectors provide several ways to identify particles in different momentum ranges. *Identifying* a particle essentially means determining a signal in a detector that can be solely attributed to a specific type of particle, e.g. Pions ($\pi^{\pm}$), Kaons ($K^{\pm}$) or Protons (p). Direct identification is restricted to charged particles because all employed techniques rely on the production of ionization signals. This analysis uses PID especially via the TPC. Here, the specific energy loss signal $\mathrm{d}E\,/\,\mathrm{d}x$ over 160 pad rows and the momentum over charge ratio p/Z of a track are measured. The energy-loss is described by the Bethe-Bloch curve in equation (2.13). For each TPC pad row, a truncated mean is calculated which represents a specific energy loss signal of the track. To identify a particle via that signal, one has to take into account the velocity dependence of the energy loss. Proposed by the ALEPH collaboration, a parameterized version of the Bethe-Bloch formula [73] can be used to fit the measured curves. It depends on $\beta = v/c$, the Lorentz factor γ and five distinct fit parameters $P_1, \ldots, P_5$

$$\frac{\mathrm{d}E}{\mathrm{d}x} = \frac{P_1}{\beta^{P_4}}\left(P_2 - \beta^{P_4} - \ln\left(P_3 + \frac{1}{(\beta\gamma)^{P_5}}\right)\right). \tag{4.1}$$

Figure 4.5 shows the experimentally measured values of the TPC energy loss in a range from $|p/Z| < 3$ together with several fits with the parameterization in equation (4.1). The energy loss is a statistical process and can only be described on average. At low signals and small p/Z, the curves start to merge, making the particle species distinction impossible. At a given velocity $\beta\gamma$, the energy loss calculated as truncated mean of a specific particle i is approximately Gaussian distributed. The standard deviation σ_i of this distribution is used to calculate the track-specific value $n\sigma_{\text{TPC},i}$ via

$$n\sigma_{\text{TPC},i} = \frac{\mathrm{d}E\,/\,\mathrm{d}x_{\text{measured}} - \mathrm{d}E\,/\,\mathrm{d}x_{\text{expected},i}}{\sigma_i}. \tag{4.2}$$

By putting cuts on the $n\sigma_{\text{TPC},i}$ for different particle species, a particle can be identified. For example, if the value fulfills $-3 < n\sigma_{\text{TPC},\pi} < 3$ for a pion π and at the same time $|n\sigma_{\text{TPC},i}| > 3.5$ for every other species, the track was most likely to be produced by a π.
Neutral particles can be identified via their (charged) decay products. The invariant mass of a particle, defined as $m = \sqrt{(E/c)^2 - p^2}/c$, is conserved through a decay process. Using the methods described above, one can identify decay products, calculate their invariant mass, and

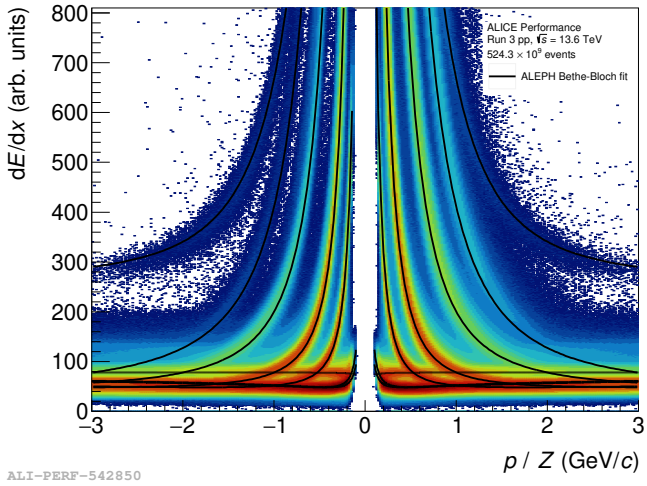


Figure 4.5: Bethe-Bloch energy loss signal in TPC from pp collisions at $\sqrt{s} = 13.6\,\mathrm{TeV}$ within a p/Z range of $-3\,\mathrm{GeV/c}$ to $3\,\mathrm{GeV/c}$ with the ALEPH Bethe-Bloch fits to signals from different particle species. [74]

fill a distribution. If done correctly and the decay daughters are selected carefully, a peak is found around the rest mass of the desired particle in the distribution.

4.6 Analysis Software

The analysis of data from the ALICE experiment depends on several software stacks that consider the special needs created by the continuous readout. Due to the large amount of recorded events, the analysis must be performed in a highly parallelized environment to produce results in a reasonable amount of time. Especially for this purpose, the new ALICE O^2 and O^2Physics framework was developed. O^2 consists of several codes that define a general data model to analyze run 3 and later run 4 data. O^2Physics is a software stack that is split into several smaller programs that perform desired tasks, so-called analysis tasks. Both, O^2 and O^2Physics is written in C++. The research program of ALICE is split into several Physics Working Groups (PWGs), which are divided into different Physics Analysis Groups (PAGs). All follow their own physics goals and have their own analysis tasks.
However, every analysis needs different general purpose analysis tasks that perform operations on data necessary for a full physics analysis. One of the tasks discussed above is the so-called *track-to-collision-association* task explained in section 4.4. Because in the data model, tracks are stored at the innermost update[4]. For various analysis cases, it might be necessary to know the track parameters at the PV. The *track-propagation* task calculates track parameters at the

[4] Innermost update refers to points in the detector where tracks first hit one of the sub-detectors. For a track with ITS, this is one of the IB layers, for track only with TPC, this is the inner wall of the TPC. Other radial positions may also be possible.

PV. In case of Monte Carlo (MC) data it is often necessary to smear the reconstructed track parameters to match differences between reconstructed MC and real data. This is performed by the *track-tuner* task, which is part of the *track-propagation*. To properly select events and tracks, there exist respective tasks called *event-selection* and *track-selection*. Additionally, tasks for PID with TPC and TOF exists. Special tasks for the presented analysis are the *multiplicity-table* task, that creates relevant multiplicity values of the detectors in an event. *Dq-table-maker-with-assoc* selects events and tracks based on user-defined cuts for the analysis of Di-Quark (DQ) analysis processes, such as $J/\psi \rightarrow e^+e^-$ that is investigated in this analysis. It uses the track-to-collision association. To read data created by this task, the *dq-table-reader-with-assoc* task is used, which creates histograms such as invariant mass distributions, p_{T} distributions or else. Both tasks have equivalents for the analysis of MC data, denoted with the suffix *-mc*.
To create histograms and for general data analysis, the package ROOT6, developed by CERN is used. Data is stored in so-called *AO2Ds* as ROOT trees. Collisions and tracks are stored in separate arrays and are connected through an index to effectively process data in a memory efficient way. Apache Arrow Tables are used as definition for this data model. This results in an unintuitive way of how data is represented: Instead of a hierarchical *event-to-track* order, data is now stored in a relational database structure. However, the usual event loop approach is still possible inside an analysis, despite being much slower in terms of computing time.
To correct for acceptance and efficiency and several background estimation processes as well as calibration and estimation of systematic uncertainties, MC datasets are necessary. In general, the raw MC output is produced via PYTHIA8.3 and then propagated virtually through the ALICE detector via GEANT4. Using other MC generators is, however, possible.

Analysis of Multiplicity Dependence of J/ψ Production

5

This chapter describes the strategy used to analyze the multiplicity dependence of J/ψ production in pp collisions at $\sqrt{s} = 13.6\,\mathrm{TeV}$. An introduction of the general analysis strategy is provided first, followed by an explanation of event- and track selection criteria. The multiplicity estimation with iterative Bayesian unfolding is then presented, followed by a description of how to extract a J/ψ signal.

5.1 Analysis Strategy

This analysis estimates the self-normalized J/ψ yield $N_{J/\psi}/\langle N_{J/\psi}\rangle$ within $|y| < 0.9$, as a function of the self-normalized charged-particle multiplicity $N_{\mathrm{ch}}/\langle N_{\mathrm{ch}}\rangle$[1] in the pseudorapidity range of $|\eta| < 0.8$. The analysis is performed in the overall available p_{T} range, denoted as p_{T} integrated, and in three p_{T} bins $0 < p_{\mathrm{T}} < 4\,\mathrm{GeV/c}$, $4 < p_{\mathrm{T}} < 8\,\mathrm{GeV/c}$, $p_{\mathrm{T}} > 8\,\mathrm{GeV/c}$. A secondary goal is to identify a sufficient multiplicity estimator at mid-rapidity. Several experimental quantities are available that can be used as an estimator: Global Tracks, PV contributors, TPC multiplicity, and FT0 multiplicity. A detailed description of how to choose the estimator is given in section 5.5. Carrying out the analysis involves several steps:

- ▷ Select suitable collision candidates.
- ▷ Calculate and correct for efficiencies related to the selection criteria.
- ▷ Estimate the charged particle multiplicities.
- ▷ Identify the J/ψ decay daughters and reconstruct the signal.
- ▷ Calculate the self-normalized J/ψ yield and multiplicity.

Event selection is performed based on several flags that select Minimum Bias (MB) events and reject pileup events. With the increased interaction rate compared to run 2, this analysis can reach up to 7 times the average multiplicity with lower statistical uncertainties. Efficiencies related to the selection criteria are estimated from MC simulations based on PYTHIA8.3 and GEANT4.

[1] In earlier analyses, the self-normalized yields were denoted as $N_{J/\psi}/\,\mathrm{d}y\,/\left\langle N_{J/\psi}/\,\mathrm{d}y\right\rangle$ and $N_{\mathrm{ch}}/\,\mathrm{d}\eta\,/\,\langle N_{\mathrm{ch}}/\,\mathrm{d}\eta\rangle$, but in these ratios, (pseudo)rapidity differentials cancel, resulting in redundant notation.

Multiplicity estimation is performed in the same pseudorapidity interval as the J/ψ signal extraction. This requirement rejects the use of the FT0 multiplicity as a possible estimator because it is located in a different pseudorapidity region. The TPC multiplicity was considered to be used as an estimator, but it was ultimately rejected due to occurrences of TPC-only tracks that have no corresponding matching candidate in the surrounding detectors, leading to a low estimator quality. Thus, only global tracks and PV contributors in $|\eta| < 0.8$ are considered as estimators. Multiplicity estimation is performed by calculating the correlation $P(N_{\text{trk}}|N_{\text{ch}})$ between the estimator and MC particles in the same rapidity interval, called detector response matrix. The matrix $P(N_{\text{trk}}|N_{\text{ch}})$, the estimator probability distribution $P(N_{\text{trk}})$ and MC particle distribution $P(N_{\text{truth}})$ is passed to an iterative Bayesian unfolding algorithm, which converts the specific amount of tracks in the detector to the physical amount of charged particles in an event.
The J/ψ signal is extracted in the e^+e^- decay channel by selecting electron (positron) candidates in the central barrel detectors with certain track quality criteria and PID $n\sigma$ values. Selected candidates are paired, and their invariant mass is calculated. A mass spectrum is obtained that shows a peak around the J/ψ and $\psi(2S)$ mass. The event-mixing technique is used to estimate the combinatorial background, while the residual background is fitted with a third-order polynomial. Both background components are subtracted and all remaining entries in a mass window around the J/ψ are counted to obtain a raw J/ψ count $N_{J/\psi,\text{raw}}$.
Raw J/ψ yield and multiplicity are calculated in MB events as well as ten multiplicity bins. Events are classified into bins according to the number of tracks in the event. The bin edges depend on the estimator are chosen in such a way that every bin has a sufficiently high J/ψ count. Ultimately, the self-normalized J/ψ yield in the i-th bin is calculated as follows:

$$n^i_{J/\psi} = \frac{N^i_{J/\psi}}{\langle N_{J/\psi}\rangle} = \frac{N^i_{J/\psi,\text{raw}}}{A^i \times \varepsilon^i} \frac{A^{\text{MB}} \times \varepsilon^{\text{MB}}}{N^{\text{MB}}_{J/\psi,\text{raw}}} \cdot \frac{n^{\text{MB}}_{\text{evt}}}{n^i_{\text{evt}}}. \tag{5.1}$$

Where $A \times \varepsilon$ is the J/ψ acceptance times reconstruction efficiency. Previous analyses have shown that the acceptance and efficiency are independent of multiplicity to first order and cancel in the ratio. The event counts are denoted with n^i_{evt} and $n^{\text{MB}}_{\text{evt}}$ in the i-th bin and MB events, respectively. The ratio $n^i_{\text{evt}}/n^{\text{MB}}_{\text{evt}}$ is calculated via integration of the event-efficiency corrected $P(N_{\text{trk}})$ distribution for the corresponding estimator, first in the desired interval $[N_{\text{trk},i}, N_{\text{trk},i+1}]$ as well as over the full available N_{trk} range. In this analysis, a maximum number of global tracks of $N_{\text{trk, Global}} = 115$ and of PV contributors of $N_{\text{trk, PV}} = 140$ was reached. The ratio is then given by

$$\frac{n^i_{\text{evt}}}{n^{\text{MB}}_{\text{evt}}} = \frac{\int_{N_{\text{trk},i}}^{N_{\text{trk},i+1}} P(N_{\text{trk}})\,\mathrm{d}N_{\text{trk}}}{\int_0^{N_{\text{trk, max}}} P(N_{\text{trk}})\,\mathrm{d}N_{\text{trk}}}. \tag{5.2}$$

The self-normalized multiplicity is determined using an iterative Bayesian unfolding algorithm of the track distributions. Applying the unfolding matrix $P(N_{\text{ch}}|N_{\text{trk}})$ to the measured distribution $P(N_{\text{trk}})$ yields the unfolded distribution $P(N_{\text{ch}})$. The mean of this distribution is equal to the average number of charged-particles $\langle N_{\text{ch}}\rangle$. A similar procedure is applied to the same track

bins as before, resulting in corresponding multiplicity distributions within the bins. The average values of these distributions are taken as the corresponding bin values N_{ch}^{i}. The self-normalized yield is then calculated as follows:

$$n_{\mathrm{ch}} = \frac{N_{\mathrm{ch}}^{i}}{\langle N_{\mathrm{ch}} \rangle} = \frac{\langle P_i(N_{\mathrm{ch}}) \rangle}{\langle P_{\mathrm{MB}}(N_{\mathrm{ch}}) \rangle}. \tag{5.3}$$

The use of self-normalized quantities has two advantages. It enables the comparison across different collision energies and systems because experiment-specific quantities cancel in the ratio due to the absence of any multiplicity dependence. This includes the integrated luminosity as well as the acceptance and efficiency.
To better visualize the departure of the production from linearity, one defines the double ratio as

$$r_{J/\psi} = \frac{N_{J/\psi}^{i} / \langle N_{J/\psi} \rangle}{N_{\mathrm{ch}}^{i} / \langle N_{\mathrm{ch}} \rangle}. \tag{5.4}$$

The physical content of this expression is the same as that of the self-normalized yields, but any deviations from linearity are stronger expressed, especially at multiplicities below the average multiplicity.

5.2 Event Selection Criteria

During the writing of this thesis the data taking of run 3 was still running, and thus only the run periods of the years 2022, 2023, and 2024 were available for analysis. All data samples were taken in pp collisions at an energy of $\sqrt{s} = 13.6\,\mathrm{TeV}$. A total amount of $1.276 \cdot 10^{10}$ events have been considered for the multiplicity analysis from which $3.481 \cdot 10^{9}$ passed the event selection criteria, listed in table 5.1. Thus, only about $30\,\%$ of the collected events are suitable for analysis.

Table 5.1: List of event selection criteria used for this analysis and their corresponding value.

Nr.	Event Cut	Value
	kIsTriggerTVX	true
	kNoTimeFrameBorder	true
	kNoITSROFrameBorder	true
	kNoSameBunchPileup	true
	kIsVertexITSTPC	true
	kIsVertexTOFmatched	true
	kIsGoodZvtxFT0vsPV	true
	$\lvert z_{vtx}\rvert$	$< 10\,\mathrm{cm}$

Cuts $1-3$ build make up the MB trigger condition, which is denoted as *sel8*. Cuts $4-7$ are referred to as *pileup rejection*, which is mainly driven by the cut *kNoSameBunchPileup*. The remaining three cuts in the pileup rejection ensure good vertex quality. A cut on the vertex z coordinate $|z_{vtx}| < 10\,\mathrm{cm}$ ensures that only events are taken into account with a PV that lies within $\pm 10\,\mathrm{cm}$ around the nominal interaction point to have the full detector acceptance available. Figure 5.1 shows how many total events are left after a cut category.

The flag *kIsTriggerTVX* is responsible for selecting events that have an acceptable FT0A to FT0C time difference, determined via a hardware vertex position measurement by FIT. When a measured vertex position lies within $\pm 20\,\mathrm{cm}$ around the nominal interaction point, the event is considered a real one. This vertex position corresponds directly to an acceptable time difference of $2\,\mathrm{ns}$. A cut on this time difference can then be applied offline to reject non-real events.
To achieve a sufficient MB trigger condition, the time-difference rejection is supplemented with a rejection of collisions that occur at the border of general data taking TF and ITS ROF. This is implemented by rejecting a constant amount of BCs at the beginning and end of each TF and ROF. The cut *kNoTimeFrameBorder* rejects the first 300 BCs as well as 4000 BCs at the TF end, while *kNoITSROFrameBorder* rejects the first 10 BCs and 20 BCs at the end of the ROF.
The entire acceptance of $|\eta| < 0.9$ is only available when the collision PV lies within $z_{\mathrm{vtx}} = \pm 10\,\mathrm{cm}$ around the nominal interaction point. Within this range, the distribution of the collision vertices is approximately Gaussian.

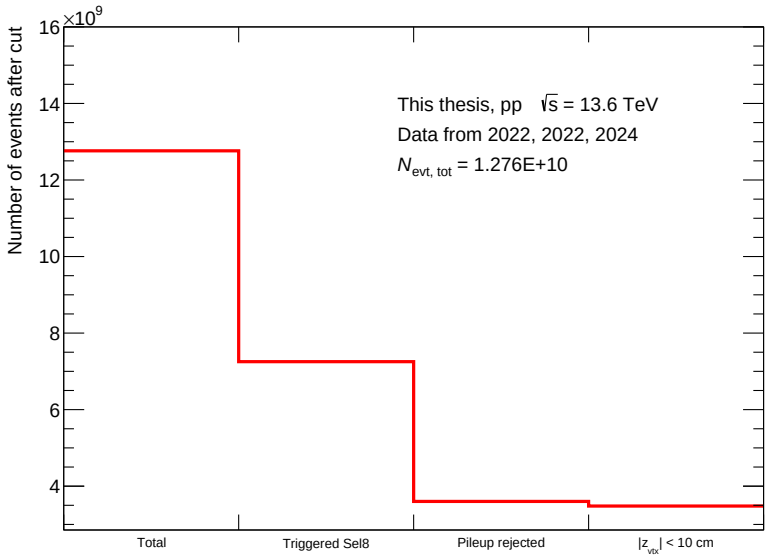


Figure 5.1: Number of events from all available run periods in MB events in pp collisions at $\sqrt{s} = 13.6\,\mathrm{TeV}$. The total number of recorded events is $1.278 \cdot 10^{10}$.

Figure 5.2 shows the distribution of the z coordinate of the PV from all available datasets and the anchored MC productions over the entire measurable range of the ITS, normalized to the distribution maximum. A green box indicates all collisions within the desired range. A slightly shifted interaction point toward the forward (positive z) region of the detector is observed for both datasets. In MC $\langle z_{\mathrm{vtx}} \rangle$ differs from data by about $\Delta z_{vtx} \approx 0.228\,\mathrm{cm}$, while both distributions are approximately equally wide. A larger Δz_{vtx} between data and MC could lead to incorrectly re-associated tracks. As described in section 4.2.4, z_{vtx} can be determined by fitting tracks within the central barrel and the timing difference in the FT0A and FT0C detectors. Ideally, both methods lead to a similar vertex position. Due to occurrences of pileup events and different resolutions, the position can vary by several centimeters. Figure 5.3 (a) shows the probability distribution of finding a collision with a $z_{\mathrm{vtx,\,barrel}}$ and $z_{\mathrm{vtx,\,FT0}}$. A marked region shows the available detector acceptance. Differences between both possible vertex positions can be up to $20\,\mathrm{cm}$, which typically belongs to pileup events. To reject such events, the cut *kIsGoodZvtxFT0vsPV* is used, which rejects all events with a difference of $\Delta z > 1\,\mathrm{cm}$. A maximally allowed difference can be defined during the analysis procedure, the chosen value represents the default value. Figure 5.3 (b) show the distribution after applying the cut.

In context of MC productions it should also be checked whether there is a significant difference between the true PYTHIA8.3 event vertex and the recontructed vertex. Larger differences could also lead to falsely associated tracks and particles, which bias the distributions. Figure 5.4 (a) shows the total z_{vtx} distribution compared to the INEL> 0 distribution, and (b) shows the correlation between the MC vertex and reconstructed vertex position. No significant impact is

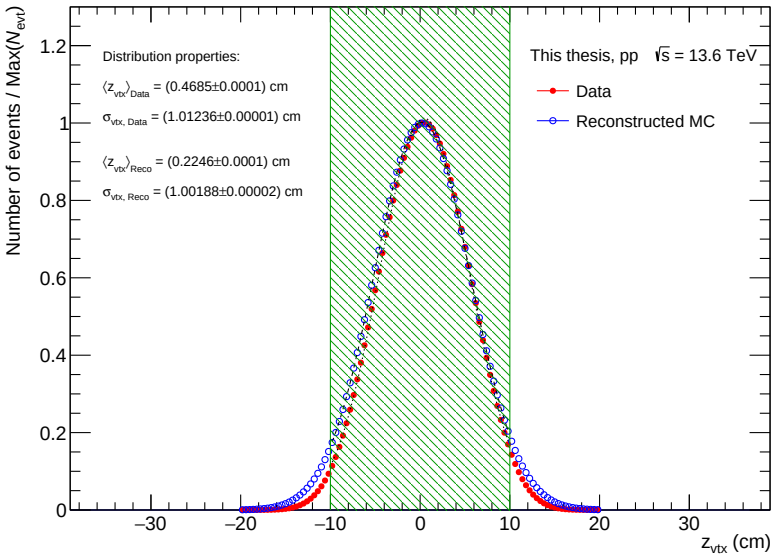
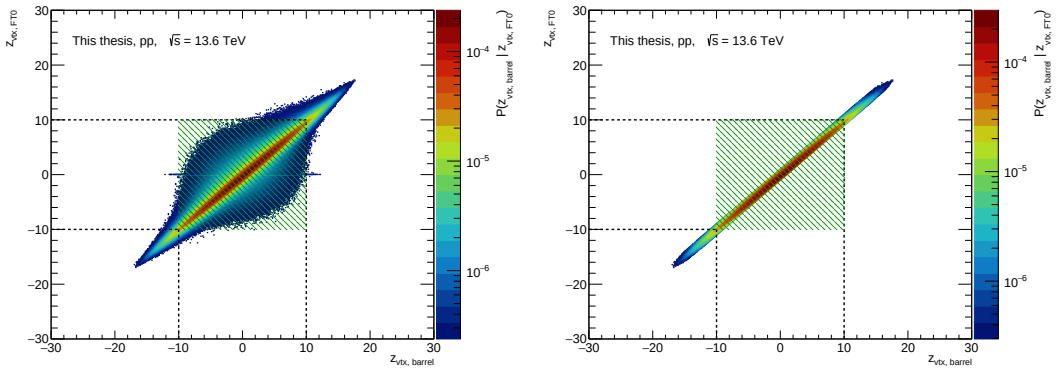


Figure 5.2: Distribution of the z_{vtx} position of the PV of all analyzed collisions. The distribution is shown for both data and reconstructed MC.

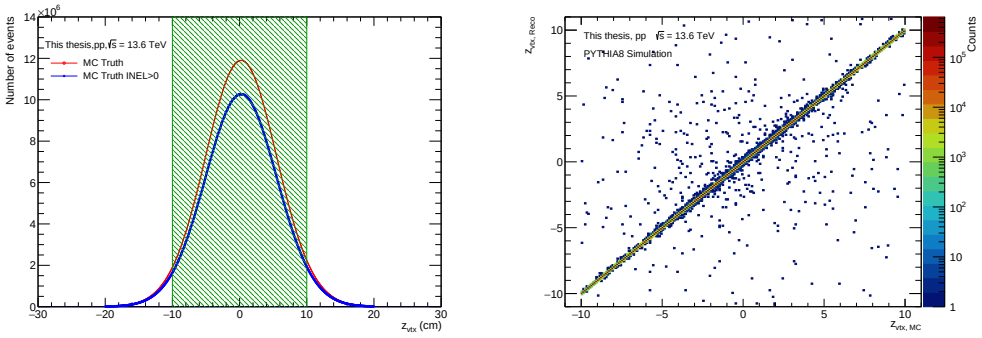
found.

To remove additional pileup events that have passed the selection criteria, an additional cut on the correlation between global tracks and PV contributors is applied in the calculation of the multiplicity estimator and the true MC particles. Pileup events occur as events with a significant difference between the number of global tracks and tracks that contributed to the fit of the PV. The correlation between global tracks and PV contributors is shown in figure 5.5 in (a) the data and (b) for the reconstructed MC. Both correlations show a significant difference, hinting at a much larger amount of simulated pileup.



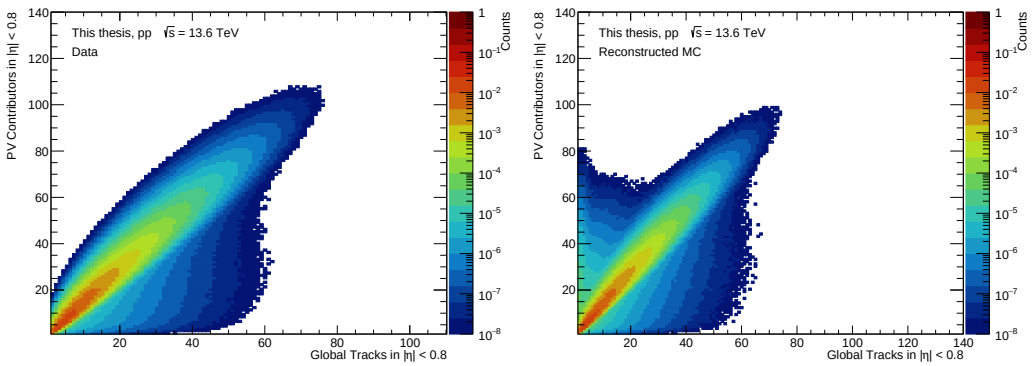
(a) (b)

Figure 5.3: Correlation between the z_{vtx} position determined from the barrel tracks and the FT0 detector before (a) the *kIsGoodZvtx* cut was applied and after the cut was applied (b). In this setup, the cut removes all events with a difference larger than $1\,\text{cm}$ in the two vertex positions.



(a) (b)

Figure 5.4: (a) Distribution of the z_{vtx} position of the primary vertex in true MC events, simulated in PYTHIA8.3 for all events and the INEL>0 event class. (b) Correlation of the z_{vtx} position of the MC truth event and the corresponding reconstructed event.



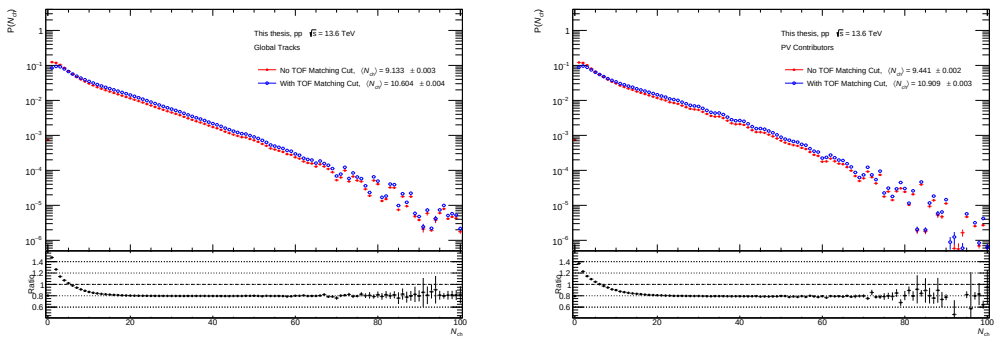
(a) (b)

Figure 5.5: Correlation between PV contributors and global tracks in pp collisions at $\sqrt{s} = 13.6\,\mathrm{TeV}$ for data (a) and for reconstructed MC (b).

Additional pile up is removed by requiring events to fulfill the following conditions:

$$N_{\mathrm{trk}} < \mu(N_{\mathrm{PV}}) + 2\sigma(N_{\mathrm{PV}}), \quad N_{\mathrm{PV}} < \mu(N_{\mathrm{trk}}) + 2\sigma(N_{\mathrm{trk}}). \tag{5.5}$$

Here, $\mu(N_i)$ and $\sigma(N_i)$ represent average and standard deviation of the corresponding $P(N_j)$ distribution at a given N_i (with $i, j \in \{\mathrm{trk}, \mathrm{PV}\}$). The different versions of these cuts are discussed in section 5.5. A value of 2σ was chosen to maximize pileup rejection and simultaneously keep as many non-pileup events as possible.



(a) (b)

Figure 5.6: Distribution of (a) global tracks and (b) PV contributors from events with and without *kIsVertexTOFMatched* cut. Applying these cuts leads to a larger $\langle N_{\mathrm{ch}} \rangle$ value.

The cut *kIsVertexITSTPC* requires that at least on PV contributor is matched between ITS and TPC. This method mainly rejects events with low vertex quality. Additionally, at least one vertex contributor must be matched to the TOF detector by requiring the cut *kIsVertexTOFmatched*. This ensures that at least one fully propagated track is present in an event and helps to reject collisions that were low in quality. Events with a larger amount of tracks have a higher probability of being matched to TOF but also events that primarily contain a low number of bad quality tracks are rejected. This influences the average number of charged particles per event. Figure 5.6 shows the $P(N_{\mathrm{ch}})$ distribution estimated via global tracks and PV contributors. By requiring TOF matching of at least one PV contributor, $\langle N_{\mathrm{ch}} \rangle$ is increased by about one particle for both estimators. Without the cut, the calculated average in this analysis differs significantly from the expected $\langle N_{\mathrm{ch}} \rangle$ value from previous experiments, which is $\langle N_{\mathrm{ch}} \rangle = 10.31$ at $\sqrt{s} = 13\,\mathrm{TeV}$ [75]. Meanwhile, the values without required TOF are $\langle N_{\mathrm{ch}} \rangle = 9.13$ for global tracks and $\langle N_{\mathrm{ch}} \rangle = 9.44$ for PV contributors and for events with matching cut $\langle N_{\mathrm{ch}} \rangle = 10.64$ for global tracks and $\langle N_{\mathrm{ch}} \rangle = 10.91$ for PV contributors respectively. Note that this values were obtained with the cuts mentioned in [75], which differ from the ones in this analysis, leading to a smaller $\langle N_{\mathrm{ch}} \rangle$ compared to the value obtained below.

5.3 Track Selection Criteria

Tracks have several quality properties that are used to decide whether the track is a result of a real particle or if it originates from the background or if the particle was poorly tracked and should be discarded because its physical properties are not well-defined. The ALICE central barrel can track particles with a momentum range of $0.1 < p_{\mathrm{T}} < 100.0\,\mathrm{GeV/c}$ in a rapidity range of $|\eta| < 0.9$. Any track with kinematic properties outside the range is probably not from a real particle. Additionally, a Distance of Closest Approach (DCA) in z-direction and in the xy-plane provides useful information on whether a track originates from a real collision or not. Note, that the DCA resolution in the xy-plane is a momentum-dependent quantity. A cut on the χ^2/ndf of the track in the ITS and TPC rejects tracks with low quality. A minimum number of required crossed rows in the TPC additionally ensures that the track passed enough of the TPC volume to be tracked in good quality. This part is assisted with the requirement of having a minimum number of actually crossed rows, divided by the number of findable clusters in the TPC. The latter requirement ensures that most of the findable clusters were actually passed, thus increasing the selected tracks' quality. The distributions of these track quality parameters, except p_{T} and η, can be seen in appendix A.1 in figure A.1. The highlighted regions mark the tracks that are called *Global Tracks*. Additionally, the distributions of tracks that are marked as PV contributors are shown. Global tracks additionally need to have at least one hit in the three innermost ITS layers. A full list of track quality requirements for global tracks is given in table 5.2. PV contributors do not need to fulfill additional quality requirements. However, it is noticeable that the PV contributors have on average a good quality compared to tracks without any quality requirement. Global Tracks in general are ITS-TPC matched tracks with high quality.

Table 5.2: Full list of track cuts required for a track to be classified as a global track.

Track cut	**Value**
min number of crossed rows TPC	70
min ratio of crossed rows over findable clusters TPC	0.8
max χ^2 per cluster TPC	4.0
max χ^2 per cluster ITS	36.0
max DCA to vertex z	2.0
max DCA to vertex xy	$0.0105 + 0.035/p_{\mathrm{T}}^{1.1}$
cluster requirement ITS	at least one hit in 3 innermost ITS layers
p_{T} range	$0.1 - 100.0\,\mathrm{GeV/c}$
η range	$-0.8 - 0.8$

5.4 Event-Level Corrections

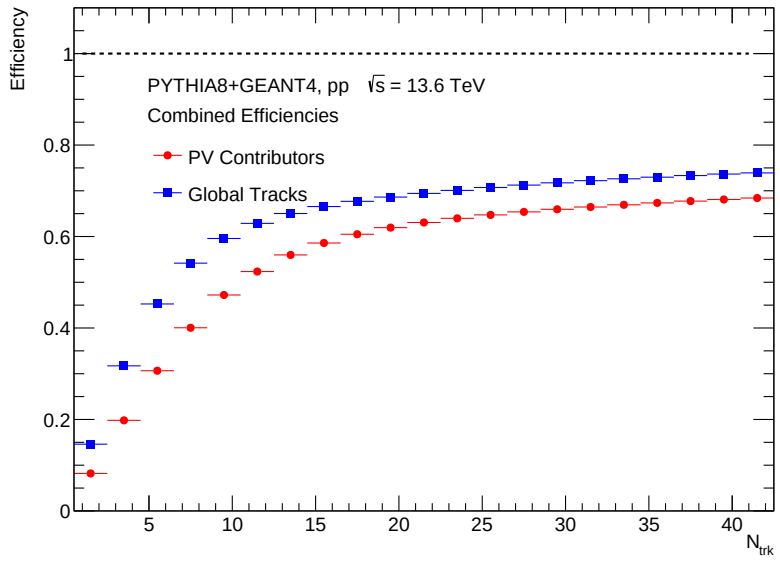


Figure 5.7: Total event selection efficiency as a function of global tracks and PV contributors in pp collisions at $\sqrt{s} = 13.6\,\mathrm{TeV}$. The efficiency was estimated using PYTHIA8.3 and a detector simulation in GEANT4.

Any event selection cut applied may introduce a bias and reject physical events that need to be compensated for. To account for these efficiencies, one determines in a MC simulation the number of events that passed the selected event cut and divides it by the total number of correctly reconstructed events. To retrieve the efficiency as a function N_{trk} or N_{PV}, the corresponding, non-normalized track distributions $\tilde{P}(N_{\mathrm{trk}})$ are calculated from reconstructed events before and after the cut. It is required that the truth MC event connected to the reconstructed collision must have at least one charged particle in $\eta < 1$ (INEL> 0). Trigger efficiency is calculated by dividing the distribution with the *sel8* cut applied by the distribution without the cut applied. All other efficiencies are calculated in the sense that the *without Cut* distribution still has the minimum bias cut passed. This ensures that the remaining cuts are independent of the trigger efficiency and avoids duplication. This provides an efficiency ε_i for each cut i:

$$\varepsilon_i(N_{\mathrm{trk}}) = \frac{\tilde{P}_{\text{Cut Applied}}(N_{\mathrm{trk}})}{\tilde{P}_{\text{Without Cut}}(N_{\mathrm{trk}})}. \tag{5.6}$$

By multiplying all independent efficiencies, the total efficiency $\varepsilon = \prod \varepsilon_i$ is obtained, shown in figure 5.7 as a function of global tracks and PV contributors. The independent efficiencies are shown in figure A.2 (a) - (f), the total efficiency is used as a multiplicity-dependent weighting factor $w = 1/\varepsilon$ applied to selected events.

5.5 Multiplicity Estimation

The number of charged particles in an event is an essential step in this analysis. Due to detector inefficiencies, particles being produced outside the detector acceptance, and background events, the measurable number of tracks that produce a hit in the detector differs from the actual amount of physical particles. It is possible that a recorded event has more tracks than actual charged particles produced and vice versa. Such differences occur on an event-by-event bias and thus do not follow any functional relationship.
Different types of tracks are qualified to act as *multiplicity estimators*. Such an estimator is then used later in a mathematical procedure called *iterative Bayesian unfolding* (see section 5.5.2) to convert the number of tracks to the number of charged particles. As an input, the unfolding needs a response matrix $P(N_{\text{trk}}|N_{\text{ch}})$ as well as the estimator distribution $P(N_{\text{trk}})$ and a true charged-particle distribution $P(N_{\text{ch}})$, both estimated from MC. A MC particle is considered for the analysis when it has the *isPhysicalPrimary* flag set, carries a non-zero charge, and is produced within $|\eta| < 0.8$. A definition and discussion of the term *primary charged particle* is given in [76]. The entries of the response matrix describe the probability that the detector responds with some N_{trk} tracks to an event with N_{ch} physical particles. Since different MC generators implement different particle production mechanisms, the choice of the estimator biases the result. ALICE in run 3 offers several track types that can potentially be used as an estimator. The global tracks and PV contributors are chosen because they inherently have the highest quality. In earlier runs of the LHC with previous detector versions, other types of estimators were available that have been discarded in the upgrade procedure. To mention here is the *SPD tracklet* multiplicity, where the Silicon Pixel Detector (SPD) was a sub-detector of the predecessor of the current ITS. Small track segments inside SPD, so-called *tracklets*, had a strong and clean correlation with the actual number of charged-particles.

5.5.1 Estimator Distributions

This section discusses the properties of two multiplicity estimators: Global tracks and PV contributors. For each estimator, the distribution is shown and compared with the corresponding MC reconstructed and MC truth distribution.

Global Tracks:

Figure 5.8 shows the distribution of global tracks in pp collisions at $\sqrt{s} = 13.6\,\text{TeV}$ together with the same distribution from reconstructed MC simulations with PYTHIA8.3 + GEANT4, and the pure MC truth distribution from PYTHIA8.3 in the same η range. No additional p_{T} cuts were applied to the MC truth distribution to not bias them, despite ALICE limited momentum range. Green lines mark the selected multiplicity bin edges. Data and reconstructed distributions are in good agreement in the low and high multiplicity regions. At mid-multiplicity, ranging from $N_{\text{trk}} = 20 - 60$, the reconstructed distribution has a slight bump. This difference will impact the

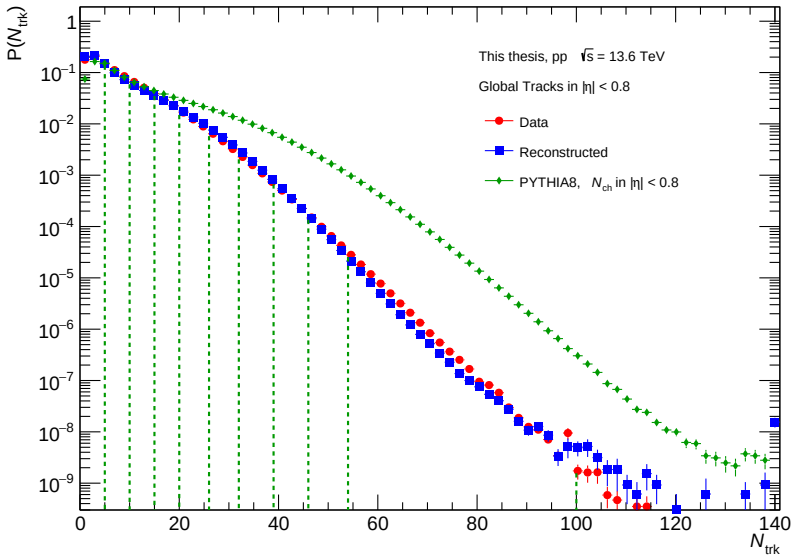


Figure 5.8: Probability distribution $P(N_{\text{trk}})$ of events in pp collisions at $\sqrt{s} = 13.6\,\text{TeV}$ from data and reconstructed MC compared to the pure PYTHIA8.3 N_{ch} distribution.

determination of multiplicity. However, because the order of magnitude of the probability is at 10^{-2} to 10^{-5}, a negligible impact is assumed for this analysis. Another difference that must be mentioned is between the track distribution and truth N_{ch} distribution. The track distribution decreases much steeper than the truth distribution, which was not observed in previous runs. This difference can be explained by the occurrence of truth MC events which have a regular distributed number of charged particles, but a minuscule number of tracks. This irregular behavior is also observed in the response matrix figure 5.9.

Such events appear as entries outside the main correlation line in the lower left corner. They occur with a probability in the order of 10^{-4} and have a significant impact on unfolding. Until now, no reason for their occurrence was found.
The response matrix in figure 5.9 was determined by simultaneously iterating over true MC events and their corresponding reconstructed events and filling the matrix $P(N_{\text{trk}}|N_{\text{ch}})$, where in the reconstructed events the same cuts as in data are applied. Additional rejections are applied to account for differences in the MC reconstruction datasets and the measured data that are shown in figure 5.5. An event is rejected when its number of global tracks is larger than $\mu(N_{\text{PV}}) + 2\sigma(N_{\text{PV}})$ of the global track distribution from events with a given number of PV contributors. The same cut is applied to events that have more PV contributors than $\mu(N_{\text{trk}}) + 2\sigma(N_{\text{trk}})$. 2σ in both cases was chosen to not only reject physical events but also to maximize the rejection of additional pile-up events. The impact of different cut values is visualized in appendix A.2 in appendix A.2. Without the additional cut, more non-main-correlation entries appear. In the

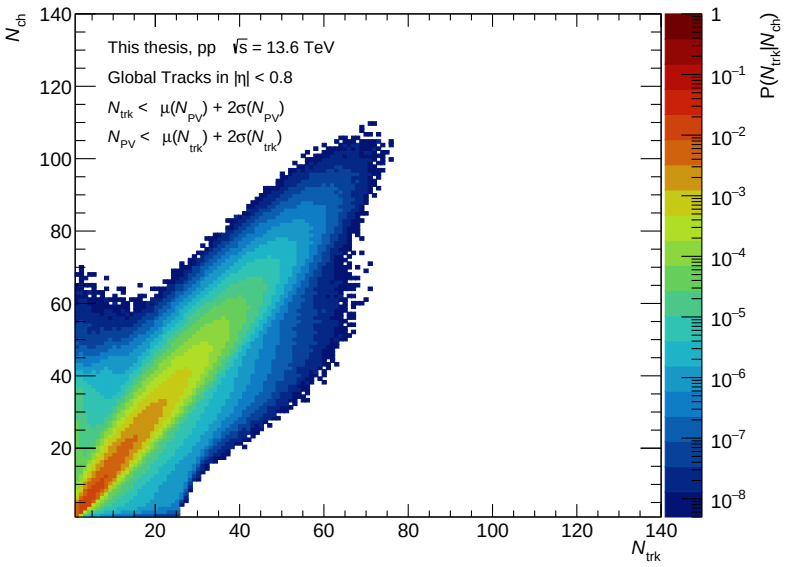


Figure 5.9: Detector response matrix for global tracks and true MC particles in pp collisions at $\sqrt{s} = 13.6\,\mathrm{TeV}$, estimated via PYTHIA8.3 and a detector simulation with GEANT4.

last tested response matrix, a significant number of entries of the main-correlation line were removed.

Although these strong cuts already remove a lot of this pileup, some entries remain outside the main correlation line. Especially MC particles at low tracks contaminate the response matrix. An additional correlation appears for some tracks between $N_{\mathrm{trk}} = 35 - 65$ and $N_{\mathrm{ch}} = 20 - 80$. The reason for this additional pileup is currently unknown. A possible reason for additional entries is a concept called vertex-splitting. When two events occur close to each other in space, they might not be distinguishable. However, its impact is not strong because the probability is in the order of $< 10^{-6}$. With global tracks as the estimator, a maximum number of $N_{\mathrm{ch}} \approx 100$ is reached with sufficient statistics at a maximum of $N_{\mathrm{trk}} \approx 80$.

PV Contributors:
The multiplicity distribution of PV contributors is shown in figure 5.10 again compared to the respective reconstructed and truth MC distributions. The measured data distribution is less steep than the truth distribution, the reconstructed distribution, in contrast to what was observed for global tracks. Instead, the reconstructed MC distribution differs strongly from the measured distribution and matches the truth distribution unusually well. This hints at the possibility that in the MC productions, only tracks with a matched MC particle are used to fit the PV. The green lines mark the bin edges used for the event selection.

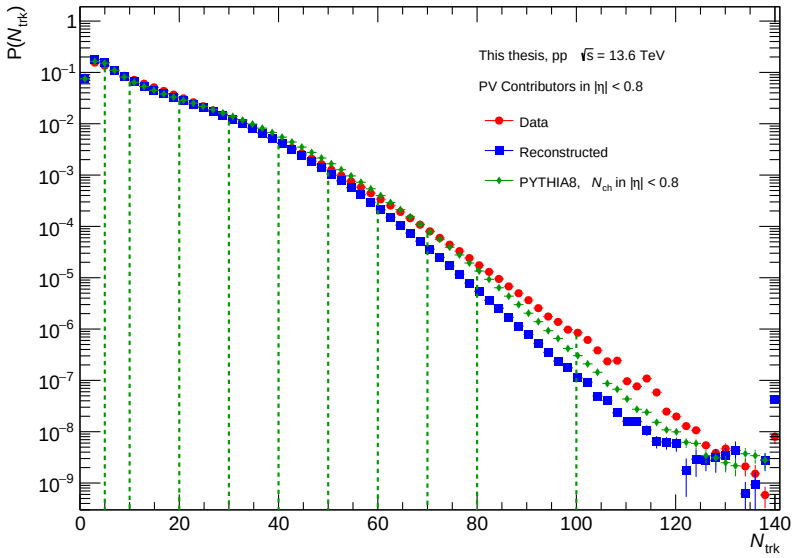


Figure 5.10: Probability distribution $P(N_{\mathrm{PV}})$ of events in pp collisions at $\sqrt{s} = 13.6\,\mathrm{TeV}$ from data and reconstructed MC compared to the pure PYTHIA8.3 N_{ch} distribution.

The response matrix for PV contributors, shown in figure 5.11, has a much more complex behavior than the global tracks matrix. $N_{\mathrm{ch}} \approx 110$ is maximally reached as the number of particles at a maximum number of tracks of $N_{\mathrm{trk}} \approx 100$. Two additional correlation lines appear that reach up to $N_{\mathrm{ch}} \approx 60$ particles at low track multiplicity with $N_{\mathrm{trk}} < 30$. A large amount of additional pileup events occur below the main correlation line. Even the additional rejection of events with a too large difference in PV contributors and global tracks has no apparent impact on the quality of the estimator, as appendix A.2 (see appendix appendix A.2) indicates.
A first quality comparison of the tested estimators shows that both suffer from contamination of a significant amount of pileup events despite having applied tight event cuts, with the global track distribution being much cleaner. In both cases, second order differences between the data and reconstructed distributions occur. Their impact on the final results needs to be studied further, but this is beyond the scope of this thesis. They are assumed to be negligible for the remainder of the analysis.

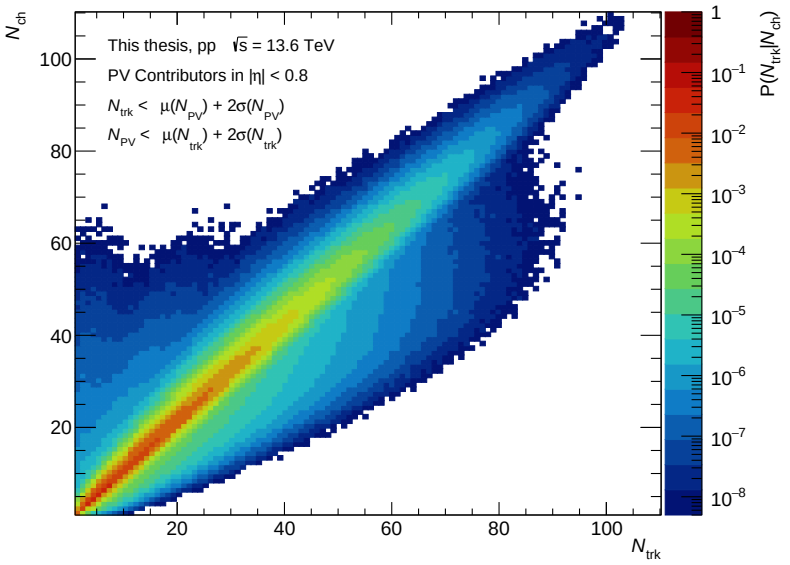


Figure 5.11: Detector response matrix for PV contributors and true MC particles in pp collisions at $\sqrt{s} = 13.6\,\mathrm{TeV}$, estimated via PYTHIA8.3 and a detector simulation with GEANT4.

5.5.2 Bayesian Unfolding of Spectra

To convert from a raw N_{trk} distribution to a real N_{ch} distribution, this analysis employs an *iterative Bayesian unfolding* algorithm, that estimates a probability matrix $P(N_{\mathrm{ch}}|N_{\mathrm{trk}})$ from the response matrix $P(N_{\mathrm{trk}}|N_{\mathrm{ch}})$, the estimator distribution $P(N_{\mathrm{trk}})$ and the true MC distribution $P(N_{\mathrm{ch}})$ via the *Bayesian theorem*[2] [77]. The term unfolding is used because the above-mentioned detector effects can be considered convoluted with the underlying real charged-particle distribution. To unfold means to deconvolute this detector effects to obtain the distribution of the primary charged particles. The Bayesian theorem states the following:

$$P(N_{\mathrm{ch}}|N_{\mathrm{trk}}) = \frac{P(N_{\mathrm{trk}}|N_{\mathrm{ch}})P(N_{\mathrm{ch}})}{P(N_{\mathrm{trk}})} = \frac{P(N_{\mathrm{trk}}|N_{\mathrm{ch}})P(N_{\mathrm{ch}})}{\sum_N P(N_{\mathrm{trk}}|N)P(N)}. \tag{5.7}$$

Bayesian unfolding requires a prior $P(N_{\mathrm{ch}})$ distribution, generated in MC, and the response matrix $P(N_{\mathrm{trk}}|N_{\mathrm{ch}})$ to calculate via the Bayesian theorem the *unfolding matrix* $P(N_{\mathrm{ch}}|N_{\mathrm{trk}})$. With the new matrix, an unfolded distribution can be determined

$$P(N_{\mathrm{ch}}) = \sum_{N'_{\mathrm{trk}}} P(N_{\mathrm{ch}}|N'_{\mathrm{trk}})P(N'_{\mathrm{trk}}). \tag{5.8}$$

[2] The general form of the Bayesian theorem states that $P(A|B) = P(B|A)P(A)/P(B)$. Here, A and B are general events that can occur with a probability $P(A)$ and $P(B)$. $P(A|B)$ and $P(B|A)$ are the *conditional probabilities*, that state the probability that A occurs given the condition that B is true (or vice versa).

$P(N'_{\text{trk}})$ is taken from real data. The tracks determined in the response matrix passed the same event cuts as the real data distribution. In this case, the track distributions for unfolding do not need to be corrected for event selection efficiencies because the correction is inherently taken care of by the unfolding procedure. In principle, one could stop at this point because an unfolded distribution was obtained. However, the unfolding matrix depends on the selection of a prior, which is not an accurate description of the real charged-particle distribution. On the other hand, since information from measured spectra and the detector response was injected to obtain the distribution in equation (5.8), it can be stated that a newly calculated $P(N_{\text{ch}})$ is a better description of the real distribution than the previous one. Thus, the new distribution is used as an input prior for another iteration, hence the name *iterative* Bayesian unfolding. The procedure is terminated when a χ^2 of change between two consecutive iterations, defined as follows:

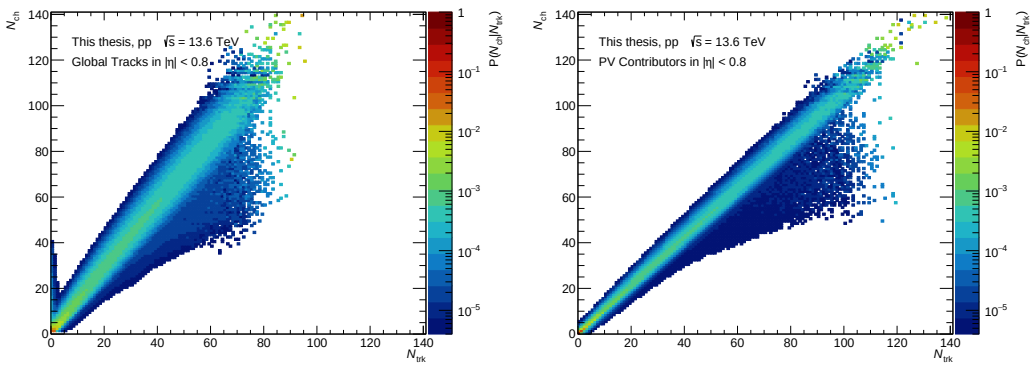
$$\chi^2 = \sum_N \begin{cases} n_{\text{evt}} \cdot \frac{(P_i(N) - P_{i+1}(N))^2}{P_i(N) + P_{i+1}(N)} & n_{\text{evt}} \cdot (P_i(N) + P_{i+1}(N)) > 1 \\ n_{\text{evt}}^2 \cdot (P_i(N) - P_{i+1}(N))^2 & \text{otherwise} \end{cases}, \tag{5.9}$$

is below unity $\chi^2 < 1$. Typically, only a few dozen iterations are necessary to reach convergence. Each iteration injects the measured distribution, resulting in statistical fluctuations in each step. These fluctuations propagate through the unfolding procedure and may be amplified by numerous iterations. A description of this error propagation is given in [78].
Figure 5.12 shows the unfolding matrices obtained by iterative Bayesian unfolding for global tracks (a) and PV contributors (b). Both distributions show a strong main correlation line with spread out entries beside the main correlation. Both matrices have additional entries outside the main correlation at roughly $N_{\text{ch}}, N_{\text{trk}} = 20 - 80$. These entries result from additional pileup events in response matrices. The global track unfolding matrix still shows entries up to $N_{\text{ch}} = 40$ at low $N_{\text{trk}} < 4$. Applying the unfolding matrix to the measured track distribution, as described in equation (5.8), yields the unfolded distributions shown in figure 5.13 (a) global tracks and (b) for PV contributors. Both cases show the unfolded distribution together with MC PYTHIA8.3 N_{ch} and the measured track distribution, as well as the unfolded and MC distribution. The mean of the unfolded distribution is taken as the MB value $\langle N_{\text{ch}} \rangle$, necessary to determine the self-normalized multiplicity values.

5.5.3 Distributions in Multiplicity Bins

To obtain bin-wise average multiplicities, the unfolding matrix is applied again to the measured distribution in the considered multiplicity intervals. For each multiplicity interval I, one calculation is performed for every N_{ch}

$$P_I(N_{\text{ch}}) = \sum_{N_{\text{trk}'}=i_{\text{low}}}^{i_{\text{up}}} P(N_{\text{ch}}|N_{\text{trk}'})P(N_{\text{trk}'}). \tag{5.10}$$



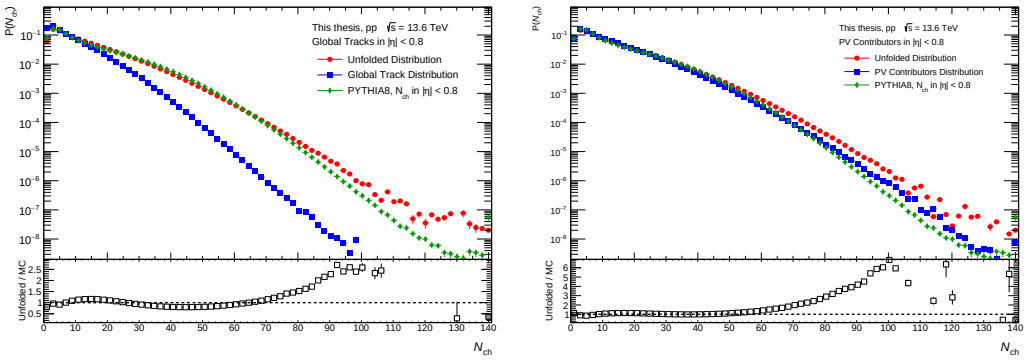
(a) (b)

Figure 5.12: Unfolding matrices used to convert the number of tracks to the number of charged-particles in pp collisions at $\sqrt{s} = 13.6\,\mathrm{TeV}$ for global tracks as estimator (a) and PV contributors (b).

Here, i_{Low} and i_{Up} are lower and upper bin edges of the interval I. The bin-wise distributions are shown in figure 5.14 for global tracks (a) and for PV contributors (b). The mean of these distributions is taken as the bin values of N_{ch}^{I} which is then divided by the average of the full unfolded distribution to obtain the self-normalized multiplicity in every bin. All bin distributions show an unphysical distortion of the probability at multiplicity much larger than or much lower than the mean value. These distortions are caused by additional pileup entries in the original response matrix. However, the impact of these distortions is negligible in the lower bins, but becomes significant at larger bins with fewer statistics. Table 5.3 lists the bin edges for global tracks and PV contributors and their corresponding N_{ch}^{I} value and the value for $\langle N_{\mathrm{ch}} \rangle$.

Table 5.3: Bin edges of the N_{trk} intervals and the corresponding self-normalized multiplicity values.

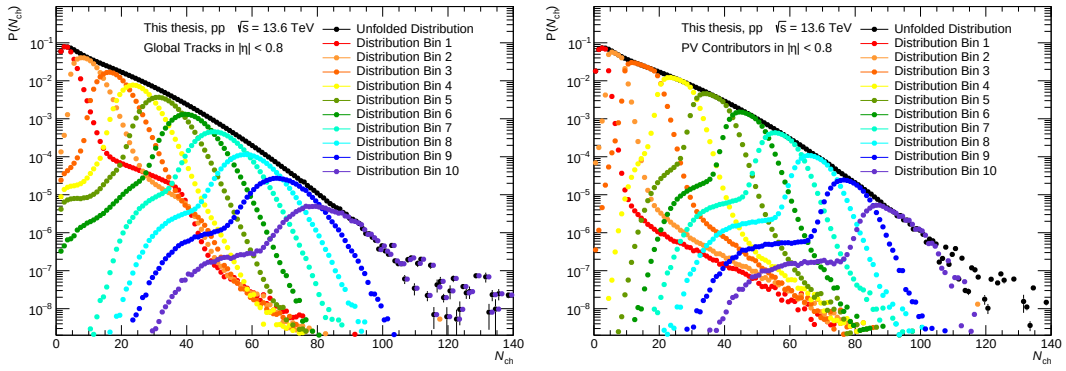
	Global Tracks		**PV Contributors**	
Bin	N_{trk} Interval	$N_{\mathrm{ch}}^{I}/\langle N_{\mathrm{ch}} \rangle$	N_{PV} Interval	$N_{\mathrm{ch}}^{I}/\langle N_{\mathrm{ch}} \rangle$
1	[0, 4]	0.33	[0, 4]	0.21
2	[4, 9]	0.81	[5, 9]	0.55
3	[10, 14]	1.46	[10, 19]	1.18
4	[15, 19]	2.08	[20, 29]	2.05
5	[20, 25]	2.72	[30, 39]	2.91
6	[26, 31]	3.42	[40, 49]	3.76
7	[32, 38]	4.15	[50, 59]	4.61
8	[39, 45]	4.95	[60, 69]	5.44
9	[46, 53]	5.75	[79, 79]	6.27
10	[54, 100]	6.81	[80, 100]	7.21
$\langle N_{\mathrm{ch}} \rangle$	11.82		12.23	



(a) (b)

Figure 5.13: Unfolded multiplicity distributions in pp collisions at $\sqrt{s} = 13.6\,\mathrm{TeV}$, estimated from global tracks (a) and PV contributors (b). The unfolded distribution is compared to the true MC distribution, the raw track distribution is shown as well.

It has to be noted that the here presented $\langle N_{\mathrm{ch}} \rangle$ values differ from those presented in figure 5.6 due to different selection cuts that were made to match the analysis to which the values were compared to. The statistical uncertainties of the average values are in the order of $0.01\,\%$ and were neglected.



(a) (b)

Figure 5.14: Unfolded distributions in the multiplicity bins defined for this analysis for global tracks (a) and PV contributors (b).

5.6 J/ψ Signal Extraction

This section describes the procedure for obtaining the number of J/ψ counts in each multiplicity bin and p_{T} interval. The J/ψ signal is reconstructed in the e^+e^- decay channel, which has an p_{T} integrated production cross-section of $\mathrm{d}\sigma\,/\,\mathrm{d}y\,|_{y=0} = 9.08 \pm 0.56\,\mu\mathrm{b}$[3] [79] at $\sqrt{s} = 13.6\,\mathrm{TeV}$. Reconstruction is performed by selecting suitable electron and positron candidates and calculate their invariant mass $m_{e^+e^-} = (p_{e^+} + p_{e^-})^{1/2}$, where p is the four-momentum of the electron (positron), and filled into a spectrum. With suitable selection cuts, a resonance structure around the rest mass of the J/ψ appears, that lies on top of a background. The intrinsic decay width of a J/ψ is $\Gamma \approx 92.9\,\mathrm{keV/c^2}$ while in the experiment, one observes a much broader structure. Especially toward lower masses, the J/ψ peak exhibits a long tail caused by the bremsstrahlung of the electrons (positrons) that pass through the detector material and cannot be fully recovered. Generally, one cannot distinguish whether a selected candidate originates from a J/ψ decay or from other sources. Therefore, each candidate is paired with every other candidate from the same event. This results in a combinatorial background beneath the J/ψ peak. Another part of the background originates from other uncorrelated dielectron sources like Dalitz decays, pair-creation from photon conversion in the detector material, and electrons that exhibited bremsstrahlung losses. Most of these background electrons (positrons) are created in the low-mass regime $< 50\,\mathrm{MeV}$ and then paired with a high-mass candidate.

The J/ψ signal is obtained by counting the entries in the invariant mass distribution within a mass window of $2.72\,\mathrm{GeV/c^2} < m_{e^+e^-} < 3.20\,\mathrm{GeV/c^2}$ after all background components are subtracted. Previous analyses used a narrower mass window with a lower mass cut at $2.92\,\mathrm{GeV/c^2}$. However, in the currently available datasets, the J/ψ invariant mass distribution has a much larger bremsstrahlung tail compared to previous runs. It is as well observed that the peak of the distribution is not at the J/ψ mass, but shifted to about $3.054\,\mathrm{GeV/c^2}$. Both can be attributed to a misalignment between ITS and TPC, but central investigations of this are currently ongoing during the writing of this thesis. These differences justify the use of a broader mass window.

The event-mixing technique is employed to estimate the combinatorial background. One pairs an electron candidate with positrons from other events. This destroys any physical correlation between electrons from the same event, resulting in a clean combinatorial background. The number of events that one candidate is mixed with is called *mixing-depth*. A larger amount of events used for mixing yields a cleaner distribution and increases the amount of pairs. A mixing-depth of 20, meaning that every electron candidate is paired with candidates from 20 other events is configured for this analysis. The event-mixing background is scaled by a factor obtained by integrating the same-event and mixed-event distribution in a high-mass sideband region from $3.4\,\mathrm{GeV/c^2}$ to $4.5\,\mathrm{GeV/c^2}$ and dividing both integrals, to reach the same-event distribution. Again, due to a large bremsstrahlung tail, only the high-mass sideband is suitable for scaling.

[3] The cross-section was extrapolated from data at $\sqrt{s} = 13\,\mathrm{TeV}$ since no official cross-section measurement was published at the corresponding collision energy of this analysis.

Another method for estimating the combinatorial background would be the *same-sign pairing* of electrons and positrons. With this method, one pairs each electron with every other electron in the same event and each positron with every other positron. The geometric mean is calculated as $2\sqrt{N_{++}N_{--}}$ and scaled to match the unlike sign distribution to provide an estimate for the combinatorial background. However, events containing J/ψ candidates are triggered at the offline level. This trigger includes the rejection of candidate events without an electron–positron pair. Consequently, only events containing at least one e^+e^- pair are kept, reducing the available statistics for the same-sign background to an unreliable level.
After subtracting the combinatorial background, the residual component is described by a third-order polynomial of the form $f(x) = ax^3 + bx^2 + cx + d$. The background is fitted in the sideband region from

$$2.0\,\mathrm{GeV/c^2} < m_{e^+e^-} < 2.2\,\mathrm{GeV/c^2} \quad \text{and} \quad 3.3\,\mathrm{GeV/c^2} < m_{e^+e^-} < 4.5\,\mathrm{GeV/c^2}.$$

Although fitting the high-mass regions includes the $\psi(2S)$ mass peak, which biases the fit, the background estimate becomes worse when excluding the $\psi(2S)$ signal region.
After all background components are subtracted, the invariant mass distribution is integrated in the previously defined mass window to obtain the raw number $N_{J/\psi}$. To define a fit quality parameter χ^2/ndf, the distribution is fitted with an asymmetric crystal ball function

$$\mathrm{CB2}(m_{e^+e^-}, \mu, \sigma, \alpha_L, n_L, \alpha_R, n_R) = \begin{cases} e^{-\frac{\alpha_L^2}{2}} \cdot \left(\frac{n_L}{|\alpha_L|}\right)^{n_L} \cdot \left(\frac{n_L}{|\alpha_L|} - |\alpha_L| - t\right)^{-n_L} & t < -\alpha_L \\ e^{-\frac{t^2}{2}} & -\alpha_L \leq t \leq \alpha_R \\ e^{-\frac{\alpha_R^2}{2}} \cdot \left(\frac{n_R}{|\alpha_R|}\right)^{n_R} \cdot \left(\frac{n_R}{|\alpha_R|} - |\alpha_R| + t\right)^{-n_R} & t > \alpha_R \end{cases} \tag{5.11}$$

where $t = (m_{e^+e^-} - \mu)/\sigma$. The fit is performed for the $J/\psi + \psi(2S)$ signal shape, scaled by the yields.

5.6.1 Electron Selection Cuts

The selection of electron (positron) candidates is done in several steps. Due to the large size of the collisions, a software trigger is applied to create so-called skimmed datasets, which enable performing analyses with less computational power. For the presented analysis, at least one e^+e^- pair with a combined $p_\mathrm{T} > 0.2\,\mathrm{GeV/c}$ that was produced within $|\eta| < 0.9$. Individual tracks should have at least one hit in the ITS IB and a TPC $\chi^2/\mathrm{clstr} < 4.0$ with at least 70 crossed rows in the TPC. Tracks are considered as electrons (positrons) when their corresponding TPC PID values fulfill the conditions $|n\sigma_\mathrm{el}| < 4.0$ and $n\sigma_{\mathrm{Pi,\,Pr}} > 2.5$. For the data taking periods of 2023 and 2024, an additional cut on the pair invariant mass at $m_{e^+e^-} > 1.8\,\mathrm{GeV/c^2}$ was applied. Additional cuts for other kinds of studies, including heavy-flavor physics and jet physics, etc. are applied. The available dataset size is reduced by approximately $33\,\%$ compared to the MB datasets. Cuts at this reduction level are chosen to be very loose to only reject tracks and events that are of no use for specified analyses. This also includes several good quality MB events, making the skimmed dataset not suitable for general multiplicity analysis. Dedicated MB datasets are stored separately, but they require much more computational time and are thus avoided whenever possible.
A second skimming process is performed after the initial reduction to remove any remaining events that are not related to the desired analysis. Pair candidate electrons must have at leat $p_\mathrm{T} > 0.7\,\mathrm{GeV/c}$ and must be produced within $|\eta| < 0.9$. Additionally, to the requirements at the trigger level for the electron tracks, they need to have a ITS $\chi^2/\mathrm{clstr} < 5.0$. For the PID, additional requirements to the momentum of the track at the inner wall of the TPC p_IN are placed. A track is rejected when $p_\mathrm{IN} < 3\,\mathrm{GeV/c}$ and TPC $n\sigma_{\mathrm{Pi,\,Pr}} > 2.5$ or when $p_\mathrm{IN} > 3\,\mathrm{GeV/c}$ and $n\sigma_{\mathrm{Pi,\,Pr}} > 1.5$. The use of these additional cuts reduces contamination from hadrons that decayed into pions or protons. Differentiating the PID values at higher and lower momentum considers that the energy loss signal is not well distinguishable at higher momentum, thus only selecting candidates that are well separated from other particles.
The reduction applied so far was performed centrally and served mainly to reduce the required computational time and disk storage for the analysis. The self-normalized J/ψ yield as a function of self-normalized multiplicity is analyzed using the following cuts:

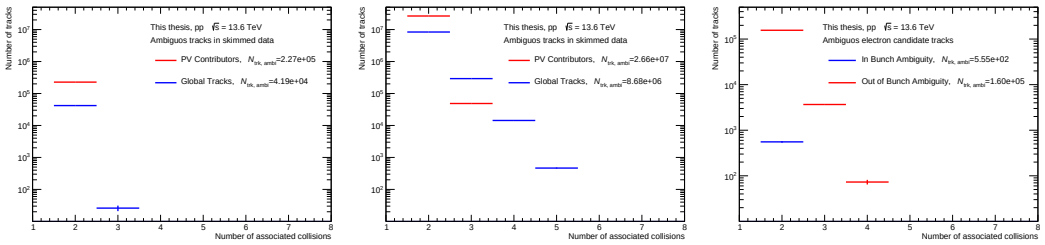
- Kinematic: e^+e^- pairs need to have a $p_\mathrm{T} > 1.0\,\mathrm{GeV/c}$ and must be produced within $|\eta| < 0.9$.
- Tracking: Each track must fulfill the following ITS + TPC tracking requirements:
  - At least one hit in the first two ITS layers: kIsSPDany
  - A ITS $\chi^2/\mathrm{clstr} < 5.0$.
  - A minimum of required crossed ITS clstr of $3 < N_{\mathrm{clstr,\,ITS}} < 100$.
  - A TPC $\chi^2/\mathrm{clstr} < 4.0$.

- ▷ A minimum of required crossed TPC clstr $100 < N_{\text{clstr, TPC}} < 160$
- ▷ A distance of closest approach in xy and z direction of $|\text{DCA}_{xy}|, |\text{DCA}_z| < 1.0\,\text{cm}$.

▷ PID: Tracks must have an electron PID signal of $-2 < n\sigma_{\text{TPC},e} < 3$ and simultaneously $n\sigma_{\text{TPC},\pi} > 3.0$ and $n\sigma_{\text{TPC, Pr}} > 3.5$.

These cuts ensure a high-quality electron selection and rejection of secondary particles and electrons from photon conversions. Applying kinematic requirements ensures that daughter tracks have the full radial TPC length available, the p_{T} requirement reduces background from electrons that originated from low-mass sources. No major amount of J/ψ daughters is rejected by this requirement, since approximately $85\,\%$ of the decay products have $p_{\text{T}} > 1\,\text{GeV/c}$. The tracking requirements ensure that the decay daughters are well tracked and have sufficient quality, which is necessary for the correct determination of PID requirements. The asymmetric electron PID requirement is because pions experience a lower energy loss at the same p_{T} than electrons. The rejection of the pion and proton $n\sigma_{\text{TPC}}$ value is applied. By using these rejection cuts, the background produced from kaons is implicitly removed because their energy loss is below the one from protons.

Such strong requirements of the DCA in the z direction and in the xy-plane reduce the amount

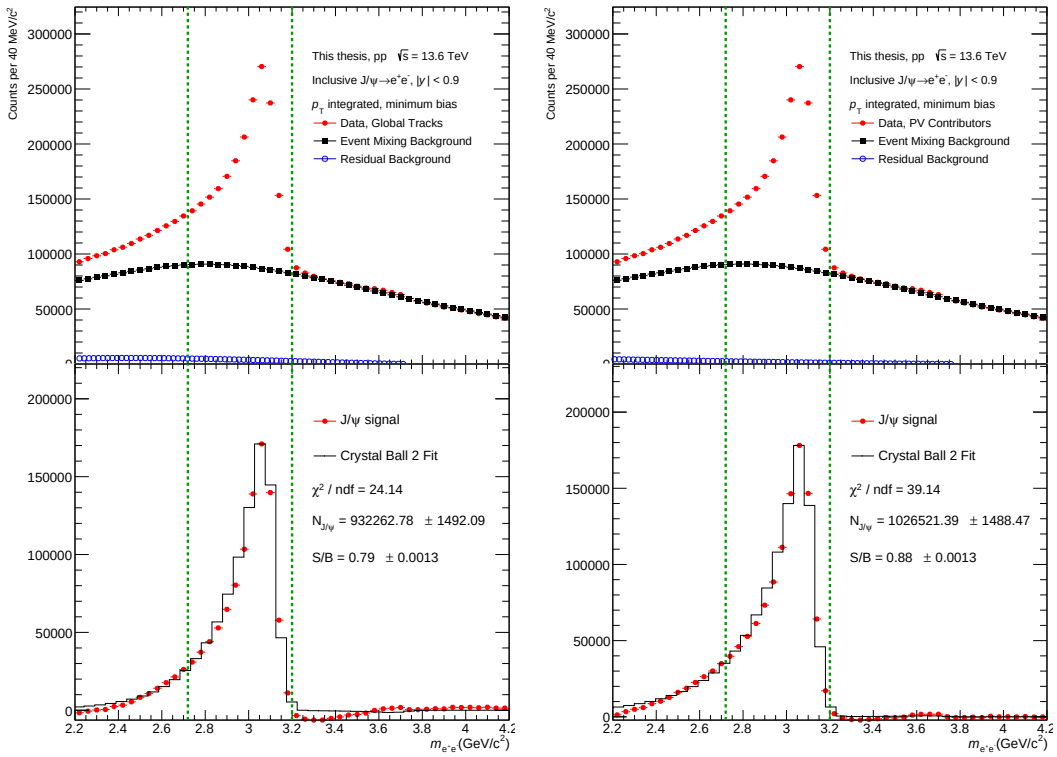


(a) (b) (c)

Figure 5.15: Number of ambiguous tracks in the analysis. (a) shows the track ambiguity of same bunch collisions, (b) the corresponding out-of-bunch ambiguity of global tracks and PV contributors. (c) shows the ambiguity of selected electron candidates.

of ambiguous tracks by a factor of 10. In a high-multiplicity environment, many tracks may be associated to several collisions. A large amount of misassociations can lead to unphysical results, since tracks may be associated with events containing a J/ψ and thus increasing the multiplicity, assigning the event to the wrong bin. The number of ambiguous tracks for both estimators is shown in figure 5.15 (a) and (b). Figure 5.15 (c) respectively shows the number of ambiguous electron candidate tracks. In general, the event- and track selection cuts lead to a low number of in-bunch ambiguous tracks but still leave a lot of out-of-bunch ambiguity.

5.6.2 Invariant Mass Distributions



(a) (b)

Figure 5.16: MB invariant mass distributions of e^+e^- pairs around the J/ψ peak in the mass range $2.2 < m_{e^+e^-} < 4.2\,\mathrm{GeV/c^2}$ in pp collisions at $\sqrt{s} = 13.6\,\mathrm{TeV}$. The upper panel shows the full distribution with the mixed-event and residual background. The lower panel shows the signal after the full background is subtracted. The event-mixing background was estimated in bins of global tracks (a) and bins of PV contributors (b). The J/ψ signal is fitted with an asymmetric crystal ball function to obtain a fit quality parameter.

Electrons (positrons) that pass the quality selection criteria are paired and their invariant mass is calculated. Figure 5.16 (a) shows the invariant mass distribution of e^+e^- candidates. The upper panel of the figure shows the full invariant mass distribution together with the combinatorial background, estimated via event-mixing, and the residual background, described by a third-order polynomial. The lower panel shows the invariant mass distribution after both background

components are subtracted. The remaining distribution is fitted with a sum of two asymmetric crystal ball functions that describe the $J/\psi + \psi(2S)$ signal shape

$$\begin{aligned} f(m_{e^+e^-},&\mu_{J/\psi}, \sigma_{J/\psi}, \alpha_L, n_L, \alpha_R, n_R, N_{J/\psi}, N_{\psi(2S)}) = \\ &N_{J/\psi} \cdot \text{CB2}(m_{e^+e^-}, \mu_{J/\psi}, \sigma_{J/\psi}, \alpha_L, n_L, \alpha_R, n_R) \\ &+N_{\psi(2S)} \cdot \text{CB2}(m_{e^+e^-}, \mu_{J/\psi} + 589.2\,\text{MeV/c}^2, 1.19 \cdot \sigma_{J/\psi}, \alpha_L, n_L, \alpha_R, n_R). \end{aligned} \tag{5.12}$$

Here, $\mu_{J/\psi}$ and $\sigma_{J/\psi}$ are mean and width, respectively, of the CB2 function Gaussian core. α_L and α_R are the left and right transition points, relative to the mean, from the Gaussian core to the power-law background and n_L and n_R are the exponents of such a background. The transition points are assumed to be equal for the J/ψ and $\psi(2S)$ peak. To further eliminate the parameters, the mean and width of the $\psi(2S)$ are assumed to be shifted relative to the J/ψ peak. Both parameters shift with the mass difference and their respective ratio:

$$\begin{aligned} \mu_{\psi(2S)} &= \mu_{J/\psi} + \Delta m_\psi \quad \text{with} \quad \Delta m_\psi = m_{\psi(2S)} - m_{J/\psi} = 589.2\,\text{GeV/c}^2 \\ \sigma_{\psi(2S)} &= \sigma_{J/\psi} \cdot \left(\frac{m_{\psi(2S)}}{m_{J/\psi}} \right) = 1.19 \sigma_{J/\psi} \end{aligned}$$

Event-mixing is performed within bins of global tracks such that only events with a similar number of global tracks (PV contributors) are mixed. Event-Mixing in different multiplicity bins is responsible for the difference in the raw number of J/ψ in both distributions.
The combinatorial background reaches the mass spectrum of the J/ψ daughters on the right side of the peak, but it is significantly underestimated on the left side. This part of the background is subtracted by the polynomial estimate. With the chosen track selection requirements, the $\psi(2S) \to e^+e^-$ peak is clearly visible around $m_{e^+e^-} \approx 3.686\,\text{GeV/c}^2$, because it shares the e^+e^- decay channel with the lighter J/ψ. However, this decay channel is much less probable [12] and the $\psi(2S)$ has in general about $10\,\%$ lower integrated production cross-section than the J/ψ. Performing an asymmetric crystal ball fit provides a quality measure for signal extraction. For both estimators, the value of χ^2/ndf is beyond 1 in the MB case, indicating a poor fit quality. With increasing event multiplicity, the quality of the fit improves significantly. The signal-to-background ratio is largest at low multiplicity and decreases significantly at high multiplicities. Overall, the fit quality of the p_T integrated study is summarized for both estimators and all datasets in figure 5.18.
The analysis was also performed in several p_T bins, ranging from $0 < p_\text{T} < 4\,\text{GeV/c}$, $4 < p_\text{T} < 8\,\text{GeV/c}$,$p_\text{T} > 8\,\text{GeV/c}$. MB distributions for global tracks and PV contributors are shown in figure 5.17. With increasing p_T, the signal extraction quality improves, due to a reduced number of multiple scatterings and higher tracking precision for the decay daughters, clearing out more background components.

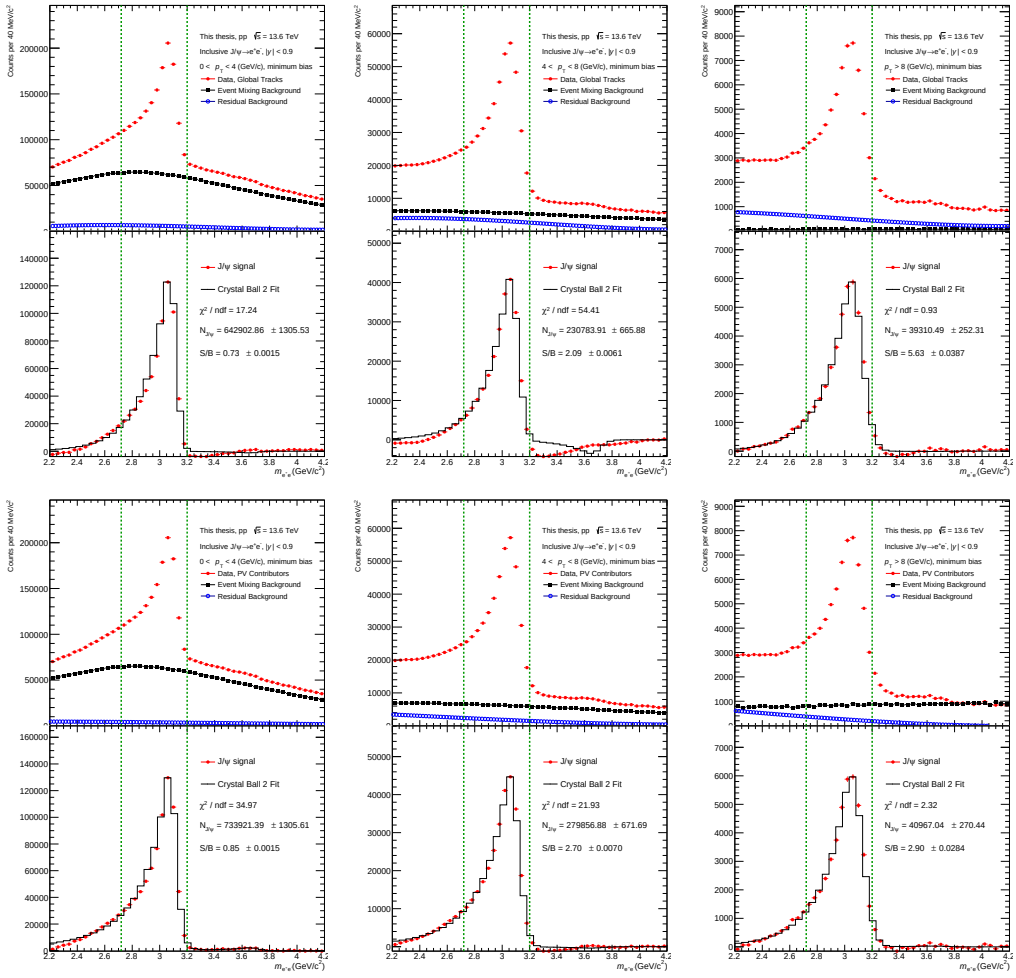


Figure 5.17: MB invariant mass distributions of e^+e^- pairs around the J/ψ peak in the mass range $2.2 < m_{e^+e^-} < 4.2\,\mathrm{GeV/c^2}$ in pp collisions at $\sqrt{s} = 13.6\,\mathrm{TeV}$ in p_T bins. The upper panel shows the full distribution together with the mixed-event background and the residual background, whereas the lower panel shows the signal after the full background is subtracted. The event-mixing background was estimated in bins of global tracks and bins of PV contributors. The J/ψ signal is fitted with an asymmetric crystal ball function to obtain the fit quality parameter

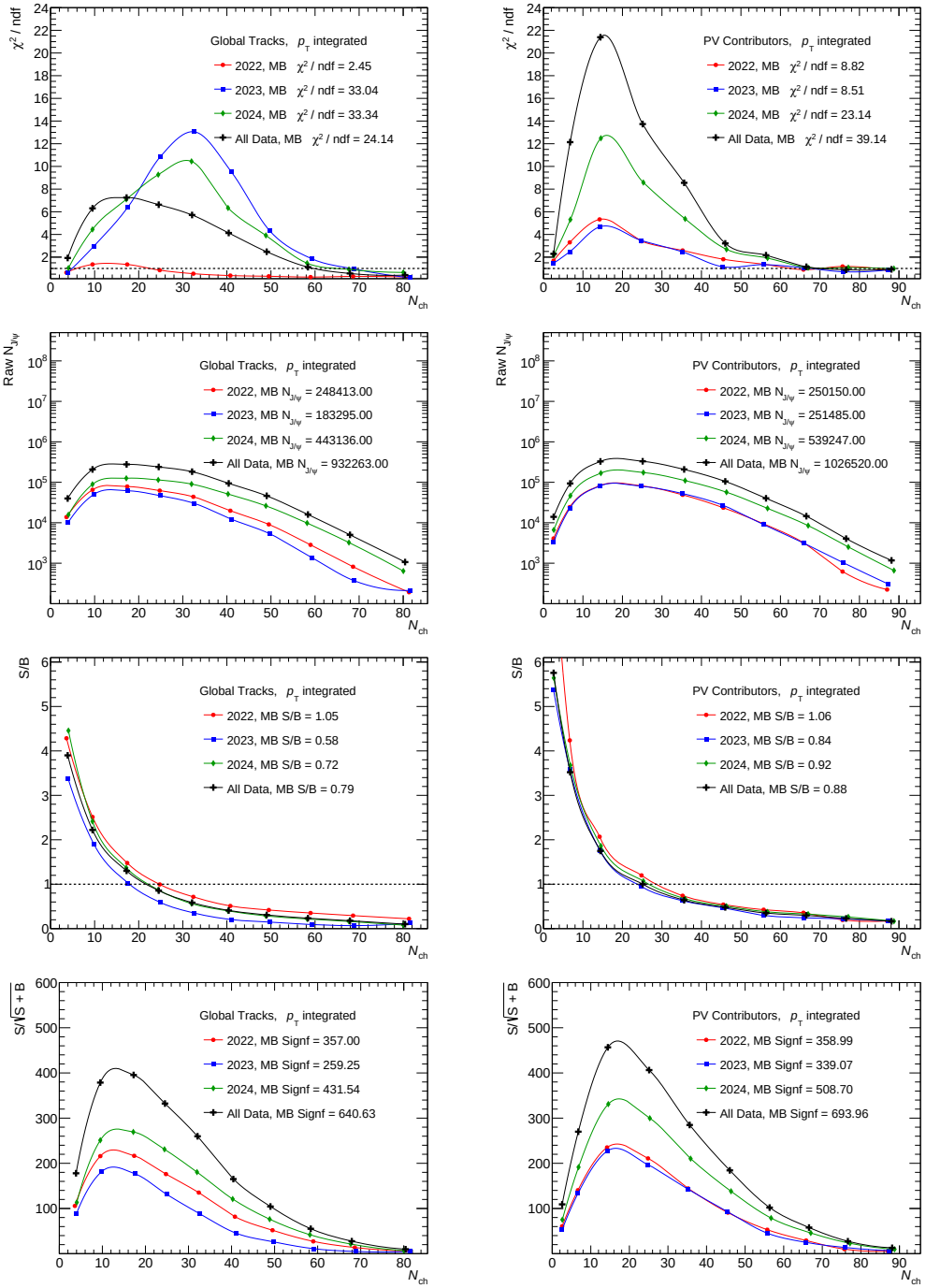


Figure 5.18: Visualization of fit quality parameters χ^2/ndf, raw $N_{J/\psi}$, S/B and $S/\sqrt{S+B}$ for both estimators and for all datasets as a function of charged-particle multiplicity.

All remaining invariant mass distributions are shown in appendix A.4 and appendix A.5. In particular, the global track signal extraction shows a large amount of over-subtraction at regions around the mass window, which is not present at the same level for the PV contributor signal extraction. In high p_{T} bins, the event-mixing background starts to flatten out, which has an significant impact on the quality of the signal extraction.

5.6.3 Statistical Uncertainties

Both yields, multiplicity and J/ψ, suffer from statistical uncertainties. In run 2, data collection was performed at an integrated luminosity of up to $7\,\mathrm{pb}^{-1}$ in MB triggered events and a maximum of $30\,\mathrm{pb}^{-1}$ at high-multiplicity triggered events. During run 3, several integrated luminosity were reached during the individual production years, shown in figure 5.19. Over the total triggered data sample, the integrated luminosity is $\approx 40\,\mathrm{pb}^{-1}$. In general, statistical uncer-

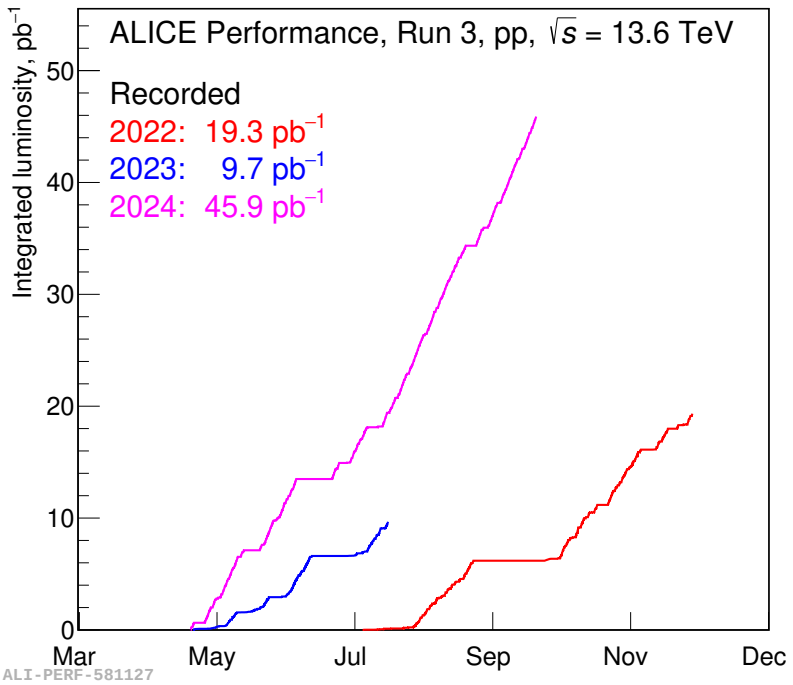


Figure 5.19: Total integrated luminosity for pp data taken in 2024 (as of 19.09.2024) compared with 2022 and 2023 data taking periods. [ALI-PERF-581127]

tainties scale like $\sigma_{\mathrm{stat}} \propto L_{\mathrm{int}}^{-1/2}$. Thus, a decrease in the statistical uncertainties of a maximum of $\sqrt{40\,\mathrm{pb}^{-1}/7\,\mathrm{pb}^{-1}} \approx 2.38$ is expected. However, the statistical uncertainties may differ from the expected luminosity scaling due to the different detector setup, event selections, and the occurrence of larger background effects.

In the case of the self-normalized multiplicity yields, the statistical uncertainty is the error of the

mean of the unfolded (MB and bins) distributions, which is added with Gaussian error propagation. Let $\sigma(\langle N_{\mathrm{ch}}\rangle)$ and $\sigma(N^I_{\mathrm{ch}})$ be the uncertainty of the mean of the MB and bin distributions, respectively. Then, the total uncertainty is given by

$$\sigma\left(\frac{N^I_{\mathrm{ch}}}{\langle N_{\mathrm{ch}}\rangle}\right) = \frac{N^I_{\mathrm{ch}}}{\langle N_{\mathrm{ch}}\rangle}\sqrt{\left(\frac{\sigma(N^I_{\mathrm{ch}})}{N^I_{\mathrm{ch}}}\right)^2 + \left(\frac{\sigma(\langle N_{\mathrm{ch}}\rangle)}{\langle N_{\mathrm{ch}}\rangle}\right)^2} \tag{5.13}$$

However, the statistical uncertainty on the self-normalized yield is negligible. The uncertainties in the highest multiplicity bin, estimated from global tracks and PV contributors, are

$$\sigma(N^{10}_{\mathrm{ch}}/\langle N_{\mathrm{ch}}\rangle) = 5\cdot 10^{-4}, \quad \sigma(N^{10}_{\mathrm{ch}}/\langle N_{\mathrm{ch}}\rangle) = 8\cdot 10^{-4}.$$

A similar relationship holds for the statistical uncertainties on the self-normalized J/ψ yield

$$\sigma\left(\frac{N^I_{J/\psi}}{\langle N_{J/\psi}\rangle}\right) = \frac{N^I_{J/\psi}}{\langle N_{J/\psi}\rangle}\sqrt{\left(\frac{\sigma(N^I_{J/\psi})}{N^I_{J/\psi}}\right)^2 + \left(\frac{\sigma(\langle N_{J/\psi}\rangle)}{\langle N_{J/\psi}\rangle}\right)^2}. \tag{5.14}$$

Uncertainties on individual yields are assumed to be $\sigma(N) = \sqrt{N}$. The full yields and uncertainties for both estimators of the p_{T} integrated analysis are shown in table 5.4.

Table 5.4: Full track intervals and corresponding self-normalized multiplicity and self-normalized J/ψ yield estimated via global tracks and PV contributors for the p_{T} integrated analysis.

	Global Tracks			PV Contributors		
Bin	N_{trk} Interval	$N^I_{\mathrm{ch}}/\langle N_{\mathrm{ch}}\rangle$	$N^I_{J/\psi}/\langle N_{J/\psi}\rangle$	N_{PV} Interval	$N^I_{\mathrm{ch}}/\langle N_{\mathrm{ch}}\rangle$	$N^I_{J/\psi}/\langle N_{J/\psi}\rangle$
	[0, 4]	0.33	0.09 ± 0.0004	[0, 4]	0.21	0.04 ± 0.0004
	[4, 9]	0.81	0.64 ± 0.002	[5, 9]	0.55	0.28 ± 0.001
	[10, 14]	1.46	1.68 ± 0.004	[10, 19]	1.18	1.05 ± 0.002
	[15, 19]	2.08	2.83 ± 0.006	[20, 29]	2.05	2.47 ± 0.05
	[20, 25]	2.72	4.08 ± 0.01	[30, 39]	2.91	4.07 ± 0.01
	[26, 31]	3.42	5.50 ± 0.02	[40, 49]	3.76	6.20 ± 0.02
	[32, 38]	4.15	7.31 ± 0.04	[50, 59]	4.61	8.17 ± 0.04
	[39, 45]	4.95	9.63 ± 0.08	[60, 69]	5.44	11.41 ± 0.1
	[46, 53]	5.75	12.00 ± 0.19	[79, 79]	6.27	13.60 ± 0.24
	[54, 100]	6.81	12.92 ± 0.54	[80, 100]	7.21	16.32 ± 0.68

6 Results

This chapter presents the results of the analysis of self-normalized J/ψ yield as a function of self-normalized charged-particle multiplicity. Results are shown for global tracks and PV contributors as multiplicity estimator. The analysis was performed both p_{T} integrated and in three p_{T} bins. Results obtained in each p_{T} bin are presented, followed by a comparison with previously published results and theoretical model predictions.

6.1 Inclusive J/ψ Production versus Charged Particle Multiplicity

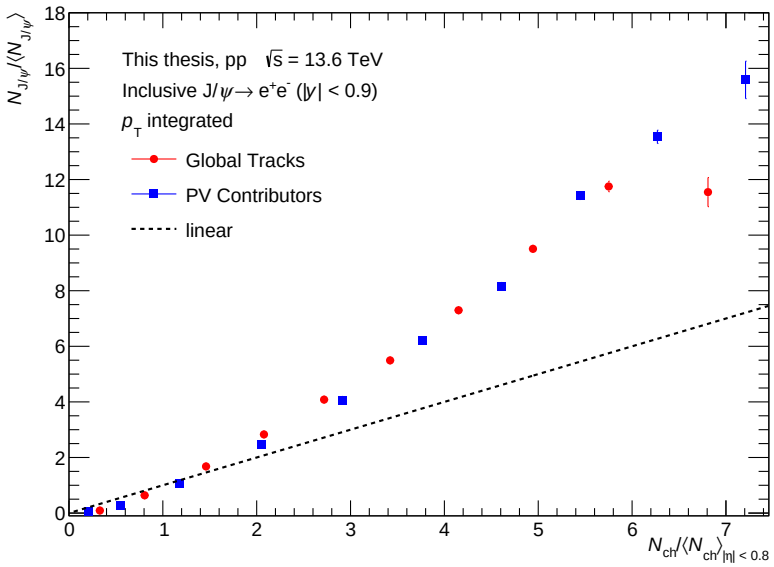


Figure 6.1: Self-normalized, p_{T} integrated J/ψ yield in $|y| < 0.9$ as a function of the self-normalized charged-particle yield in $|\eta| < 0.8$ in pp collisions at $\sqrt{s} = 13.6\,\mathrm{TeV}$. The multiplicity was estimated from two types of tracks: Global tracks (red) and PV contributors (blue). Additionally, a linear function is drawn to clearly show the departure from linearity.

Results of the p_{T} integrated analysis of the self-normalized J/ψ yield in $|y| < 0.9$ as a function of the self-normalized multiplicity are shown in figure 6.1. The multiplicity was estimated using

two types of tracks: Global tracks (red) and PV contributors (blue). To visualize the departure from a linear increase, an additional linear function $y = x$ is drawn.
With PV contributors, a maximum relative multiplicity of $n_{\mathrm{ch}} = 7.21$ is reached while global tracks extend up to $n_{\mathrm{ch}} = 6.81$. A deviation from linearity can also be visualized by calculating the double ratio $r_{J/\psi}$ as a function of n_{ch}. This is shown in figure 6.2, together with a constant line at 1 representing the linear increase.

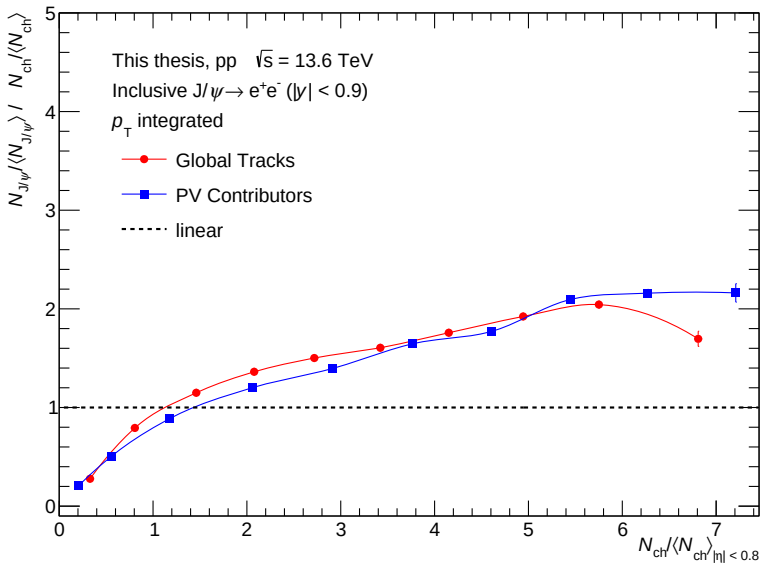


Figure 6.2: Double ratio of self-normalized, p_{T} integrated J/ψ yield and self-normalized charged-particle multiplicity. The constant line at 1 denotes a linear increase.

A strong deviation from a linear increase is observed over the complete multiplicity range. For $n_{\mathrm{ch}} < 1$, the double ratio is below unity but increases significantly for multiplicities above 1.
Overall, the curve shapes of both estimators are similar. Between a relative multiplicity of 2 to 5, the yield estimated from global tracks is slightly above the PV contributor estimation, but then suddenly drops in the last multiplicity bin about half a unit in the relative J/ψ yield. This sudden decrease is due to the low statistics in the higher-track bins. As previously examined, the $P(N_{\mathrm{trk}})$ distribution of the global tracks only reaches up to ≈ 80 tracks with sufficient statistics.
The p_{T} differentiated analysis for both estimators is shown in figure 6.3. Again, for all p_{T} bins and estimators, a clear departure from a linear increase is visible. The slope of the stronger-than-linear curve significantly increases with p_{T}. Due to less available statistics, higher p_{T} bins can only be investigated up to lower relative multiplicities with sufficient significance. For both estimators, the last bins show a decrease in the relative yield. Despite this, a clear increase of the slope is still visible in the lower multiplicity regime. The increase with larger p_{T} is much stronger by the global track estimation than by the PV contributors. In addition, the estimation

by PV contributors in the $p_{\mathrm{T}} > 8\,\mathrm{GeV/c}$ bin lasts only up to a relative multiplicity of ≈ 4, whereas the global track estimation reaches up to ≈ 4.6.

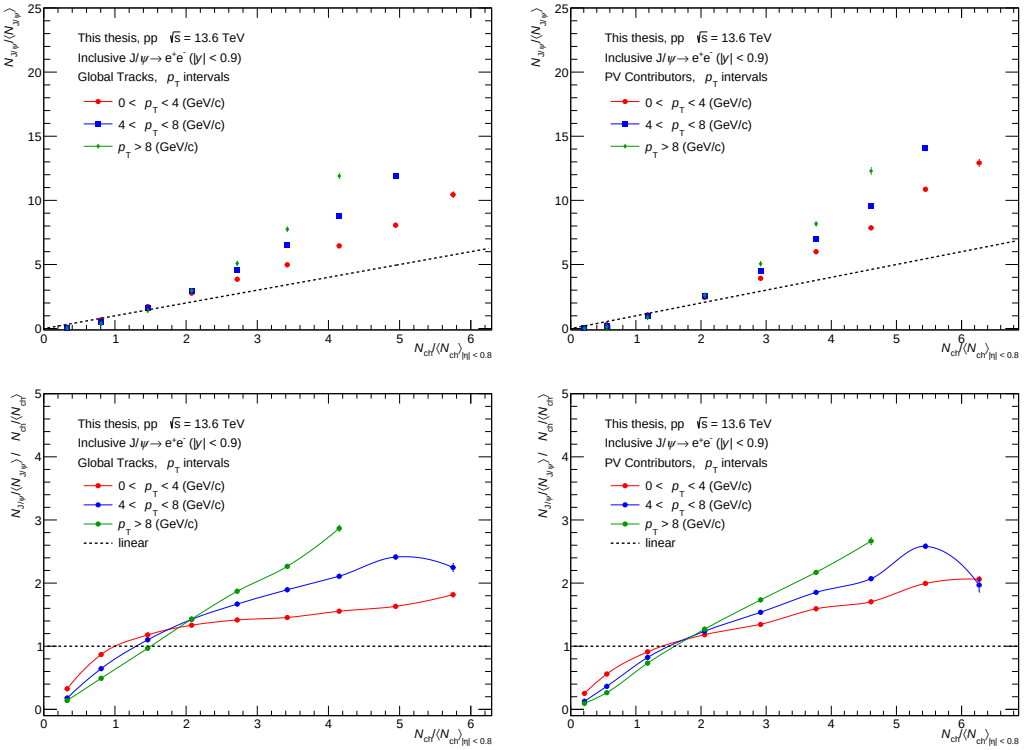


Figure 6.3: Self-normalized J/ψ yield as a function of self-normalized multiplicity, estimated via global tracks and PV contributors for three p_{T} bins and the corresponding double ratios.

The same analysis was performed independently for each available dataset, with the results shown in appendix A.6 in the appendix. For each dataset, a more complex picture emerges. There are clear differences between the three run periods, especially in the global track estimation. The main difference between the runs was the total integrated luminosity. In the years 2023 and 2024, for the offline reconstruction, additionally TPC-only tracks were removed to reduce necessary storage. Differences might occur due to different background behavior in the signal extraction. During the analysis, it was found that the selection of the mass region for the sidebands hashave a significant impact on the results, even in the combined datasets, hinting at large systematic uncertainties.

6.2 Comparison with previously published Results

The obtained results are compared with the results from previous analysis. The values for the self-normalized yield versus multiplicity, estimated from SPD tracklets at $\sqrt{s} = 7\,\mathrm{TeV}$, are taken from [1], and the corresponding values at $\sqrt{s} = 13\,\mathrm{TeV}$ are taken from [80]. The estimation via global tracks at $\sqrt{s} = 13\,\mathrm{TeV}$ are preliminary results and were not published yet. Figure 6.4 shows the relative J/ψ yield versus the relative multiplicity at $\sqrt{s} = 13.6\,\mathrm{TeV}$ compared to the same observable at $\sqrt{s} = 7\,\mathrm{TeV}$ and $\sqrt{s} = 13\,\mathrm{TeV}$. Results from two distinct estimators are available at $\sqrt{s} = 13\,\mathrm{TeV}$, both included data triggered by a high-multiplicity trigger, which is not present at $\sqrt{s} = 13.6\,\mathrm{TeV}$. The global tracks used in the analysis at $\sqrt{s} = 13\,\mathrm{TeV}$ have a different definition to the ones used in the presented analysis. Primarily, they differ in a less strict η cut ($|\eta| < 0.9$ instead of 0.8) and additionally require a maximum of 0.4 fraction of shared TPC clusters and an additional geometrical length cut. In run 2, the yield estimated from the global tracks is shown in two ways. The first, marked with black crosses, shows the same estimation performed during this analysis. In the second case, the J/ψ decay daughters were removed from the multiplicity estimator to reduce the influence of autocorrelations. Systematic uncertainties are not included in this comparison.

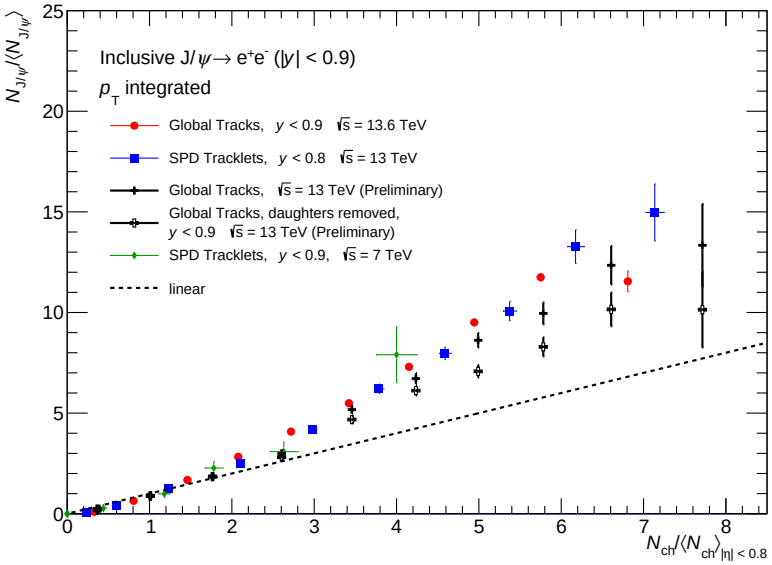


Figure 6.4: Self-normalized, p_T integrated J/ψ yield as a function of self-normalized multiplicity, estimated via global tracks, compared to the previously published results. The SPD tracklet estimation at $\sqrt{s} = 7\,\mathrm{TeV}$ was published in [80], the corresponding analysis at $\sqrt{s} = 13\,\mathrm{TeV}$ was published in [1]. The global track estimation at $\sqrt{s} = 13\,\mathrm{TeV}$ is a preliminary result that is not published yet.

Overall, the results obtained in this analysis are in good agreement with previously published results. In the representation of self-normalized yields, it is expected that the influence of the detector or the collision energy and system will mostly vanish. The values estimated via global tracks at $\sqrt{s} = 13\,\mathrm{TeV}$ and $\sqrt{s} = 13.6\,\mathrm{TeV}$ have a different slope, and the results from the present analysis are more consistent with the SPD tracklet estimation. In general, the shape remains the same, although a clearly visible difference between the two versions of the global track estimators is visible. Statistical uncertainties decrease approximately by a factor of 2.63 for the global tracks compared to SPD tracklets and 2.08 for the PV contributors. This is approximately in agreement with the expected reduction of $\sqrt{5.7} \approx 2.34$ from the increase in the integrated luminosity. In particular, the estimation by PV contributors is in excellent agreement with the SPD tracklets. Small deviations are present in the high-multiplicity bins, and the general amount of statistics is large enough to reach approximately the same relative multiplicity as the other analyses.

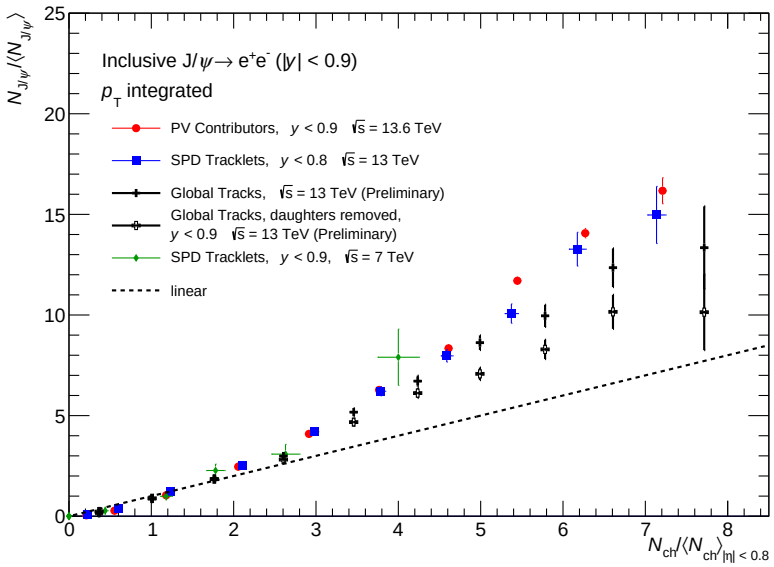
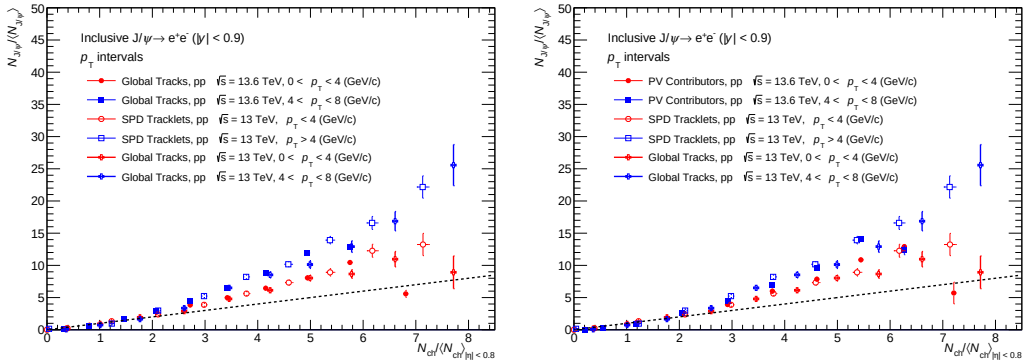


Figure 6.5: Self-normalized, p_T integrated J/ψ yield as a function of self-normalized multiplicity, estimated via PV contributors, in comparison with previously published results. The SPD tracklet estimation at $\sqrt{s} = 7\,\mathrm{TeV}$ was published in [80], the corresponding analysis at $\sqrt{s} = 13\,\mathrm{TeV}$ was published in [1]. The global track estimation at $\sqrt{s} = 13\,\mathrm{TeV}$ is a preliminary result that is not published yet.

The comparison in p_T bins for both estimators is shown in figure 6.6. Data points from the presented analysis are shown as full markers, whereas points from earlier analyses have open markers. Distinct p_T intervals are marked with the same color. The SPD tracklet estimation at $\sqrt{s} = 13\,\mathrm{TeV}$ was performed in two bins $p_\mathrm{T} < 4\,\mathrm{GeV/c}$ and $p_\mathrm{T} > 4\,\mathrm{GeV/c}$. Again, both estimators agree well with previously published results. It has to be noted that, despite having a much

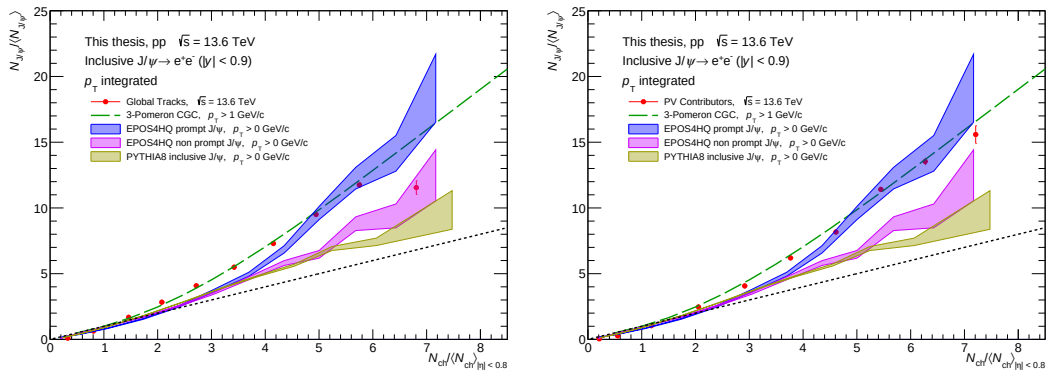
larger integrated luminosity, the relative multiplicity of this analysis does not reach the same value as in the previous analyses. This is due to the absence of a high-multiplicity trigger in run 3. The estimation via global tracks shows a decrease of the relative J/ψ yield in the last bin at $0 < p_{\mathrm{T}} < 4\,\mathrm{GeV/c}$ which is not present in the SPD tracklet analysis.



(a) (b)

Figure 6.6: Self-normalized J/ψ yield as a function of self-normalized multiplicity in two p_{T} bins, estimated via global tracks (a) and PV contributors (b), in comparison to the previously published results. The SPD tracklet estimation at $\sqrt{s} = 7\,\mathrm{TeV}$ was published in [80], the corresponding analysis at $\sqrt{s} = 13\,\mathrm{TeV}$ was published in [1]. The global track estimation at $\sqrt{s} = 13\,\mathrm{TeV}$ is a preliminary result that is not published yet.

6.3 Comparison with Theoretical Models



(a) (b)

Figure 6.7: Self-normalized, p_{T} integrated J/ψ yield as a function of the self-normalized charged-particle multiplicity, estimated via global tracks (a) and PV contributors (b) in comparison to theoretical predictions from a 3-Pomeron CGC, the EPOS4HQ event generator, and the PYTHIA8.3 event generator. The CGC predictions are taken from [81], the EPOS4HQ model is described in [82, 83], and the PYTHIA8.3 model is described in [52].

Figure 6.7 shows the p_{T} integrated relative J/ψ yield as a function of charged-particle multiplicity, estimated via global tracks (a) and PV contributors (b) in comparison to predictions from several models. The 3-Pomeron CGC is a quarkonium production mechanism implemented within the CGC EFT that was developed by E. Levin, I. Schmidt and M. Siddikov [81]. EPOS4 HQ (Heavy-Quark) is a MC event-generator developed by K. Werner that uses a parton-ladder and factorization approach to simulate particle production in a broad range of collision systems [82, 83]. EPOS4 implements a core-corona separation, where the core is treated via a relativistic hydrodynamic evolution to incorporate flow effects. Heavy quarks are created in these parton ladders and interact with the medium via elastic and radiative collisions. They hadronize via coalescence or fragmentation [82, 84]. The simulation can be performed with or without hydrodynamic treatment, the presented predictions were produced with the hydro option enabled. PYTHIA8.3 MC is the last model compared to, which was described in section 3.2.
Predictions from the CGC include only J/ψ with $p_{\mathrm{T}} > 1\,\mathrm{GeV/c}$ while the other also include the J/ψ down to zero p_{T}, although this difference has no major influence on the final results since $\approx 85\,\%$ of the J/ψ have $p_{\mathrm{T}} > 1\,\mathrm{GeV/c}$ anyway. CGC and PYTHIA8.3 predictions include both prompt and non-prompt J/ψ, but since EPOS4HQ does not reproduce the non-prompt fraction well enough, a comparison to inclusive results are not eligible. Instead, the results are compared with the individual relative yields of prompt and non-prompt J/ψ.
For both estimators, the 3-Pomeron CGC model fits the data best over the full available multiplicity range. At relative multiplicities < 1, all models show an increase in agreement with linearity.

In the mid-multiplicity regime, the models all exhibit different behaviors. In the case of the PV contributors at $1 < n_{\text{ch}} < 5.5$, the 3-Pomeron CGC has a slightly stronger increase than the data, which vanishes again for $n_{\text{ch}} > 5.5$, where the models fit the data very well again. For both estimators again, the prompt component of the EPOS4HQ simulation agrees within the uncertainty band at $n_{\text{ch}} > 4.5$. Both the non-prompt component of the EPOS4HQ model and the inclusive PYTHIA8.3 simulation drastically underestimate the data for both estimators and for a relative multiplicity of > 1.

7 Summary and Outlook

The presented thesis dealt with the analysis of the self-normalized inclusive J/ψ yield at mid-rapidity as a function of the self-normalized charged-particle multiplicity in $|\eta| < 0.8$ at a center-of-mass energy of $\sqrt{s} = 13.6\,\mathrm{TeV}$ for p_T integrated J/ψ as well as in three p_T bins of $p_\mathrm{T} < 4\,\mathrm{GeV/c}$, $4 < p_\mathrm{T} < 8\,\mathrm{GeV/c}$ and $p_\mathrm{T} > 8\,\mathrm{GeV/c}$. Multiplicities were estimated using two types of tracks: Global tracks and PV contributors. To convert from the raw number of tracks in a collision to the true charged-particle multiplicity, an iterative Bayesian unfolding algorithm was employed.

With the upgraded ALICE detector in the LHC run 3 period, relative multiplicities of approximately 7 times the average values were reached. In the p_T integrated analysis, the global track estimation reached a relative J/ψ yield of 13 times the average and more than 16 times the average for the PV contributor estimation. The obtained results show a clear stronger-than-linear increase. The strength of this slope is p_T dependent and increases with larger p_T. Both mid-rapidity estimators show good agreement over a broad range of multiplicities. Deviations are found between the estimators in the largest multiplicity bin. In general, PV contributors as multiplicity estimator seem to be more stable than global tracks. They also reach larger multiplicities.

The updated results are in good agreement with previously published data from run 2 of the LHC. Statistical uncertainties could be reduced by a factor of ≈ 2.1 to 2.6. A comparison to various theoretical model predictions was also performed. A 3-Pomeron CGC approach fits the measured data well, whereas the EPOS4HQ and PYTHIA8.3 event generators only describe the general stronger-than-linear increase of the relative J/ψ yield with multiplicity, but fail to reproduce the same strength as observed in data.

Because it is outside the scope of this thesis, no systematic uncertainties were estimated. However, the checks performed during the analysis indicate that the systematic uncertainties are significant. Determining systematic uncertainties is an important next step in this analysis. Additional quality assurance is also necessary to verify the results, especially on the track ambiguity, since wrong track associations to events with a J/ψ may have a large impact on the final result. The signal extraction method used in this analysis suffered from many uncertainties that need to be studied more carefully and must be understood for a final conclusion of this analysis.

To further extend the analysis, a separation in prompt and non-prompt J/ψ can be performed. The detector setup of ALICE in LHC run 3 offers favorable conditions for such studies. Investigations of the multiplicity dependence of the $\psi(2S)$ yield and the ratio to J/ψ would also be a natural extension of this analysis.

Appendix

A

A.1 Track Selection Criteria Distributions

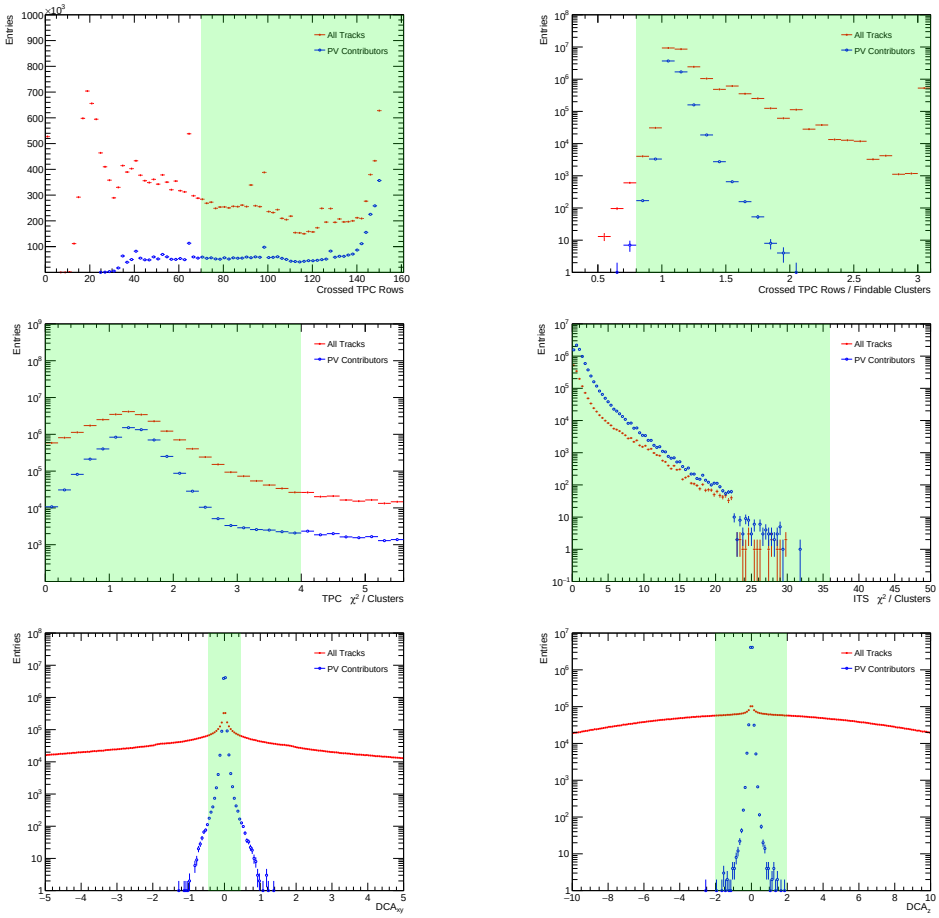
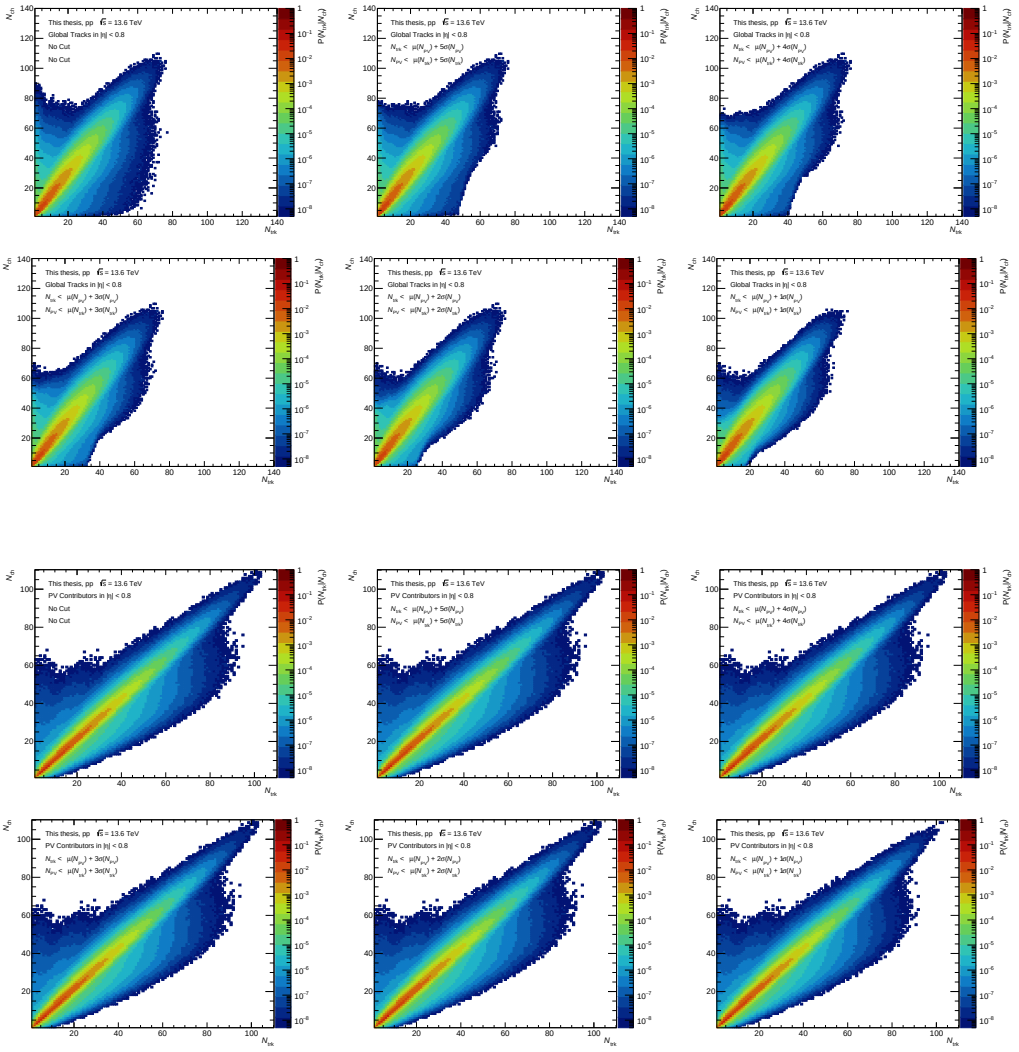


Figure A.1: Global Track quality selection criteria (except kinematic requirements). The green regions mark the requirement for a track to be qualified as a global track. The same criteria are also shown for tracks that are PV contributors.

A.2 Track-to-Particle Correlations for different $n\sigma$

Global Tracks: PV Contributors:



A.3 Independent Event Cut Efficiencies

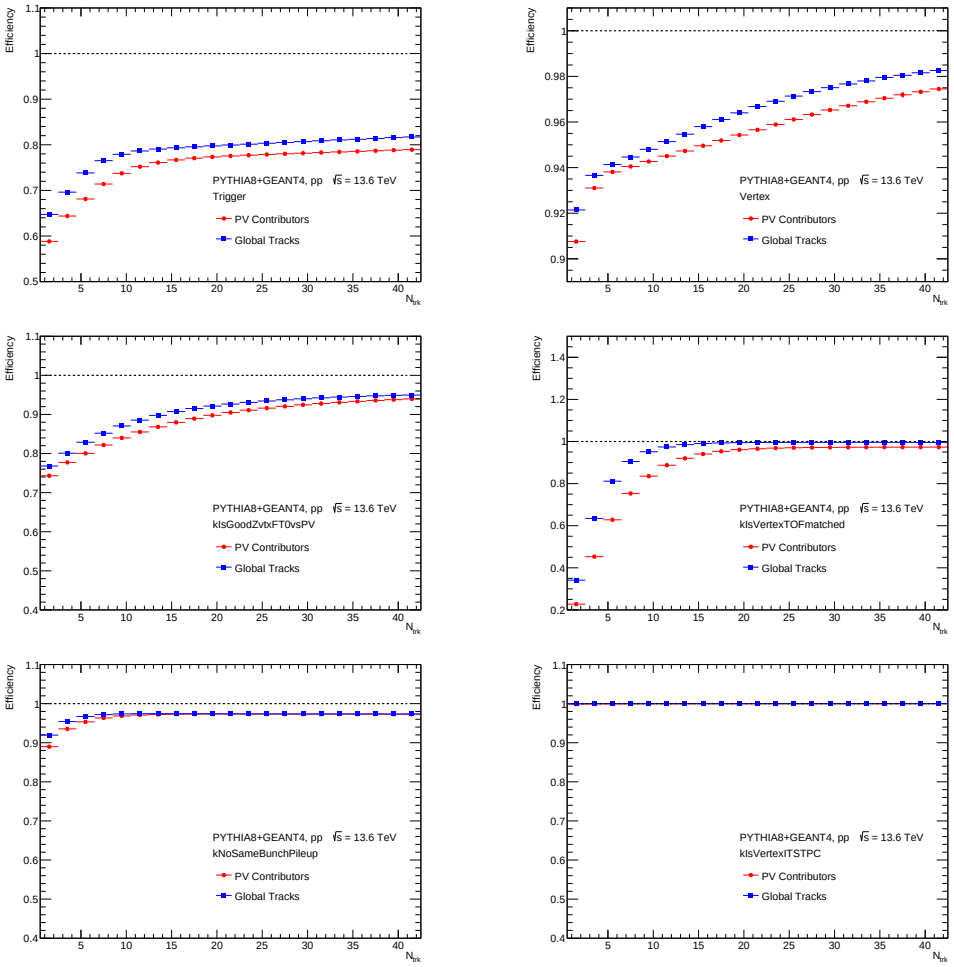
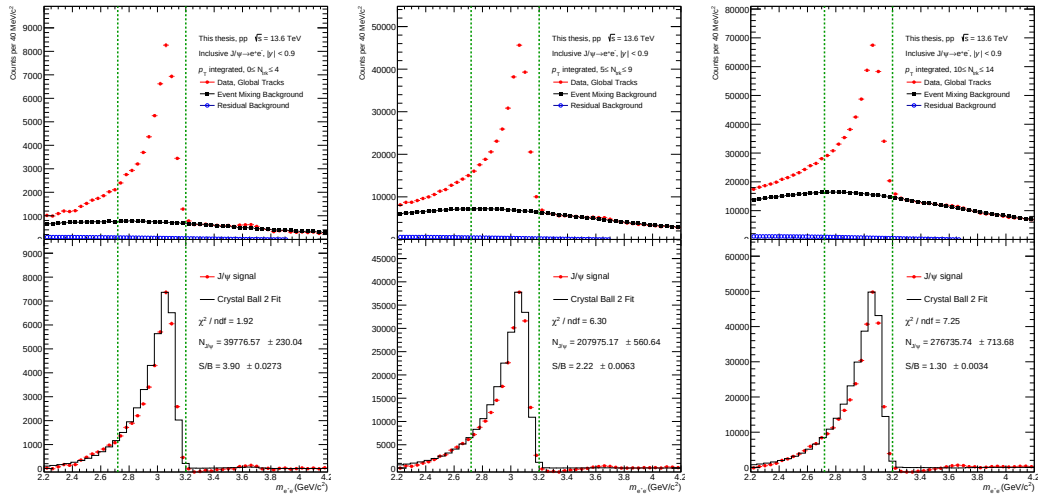
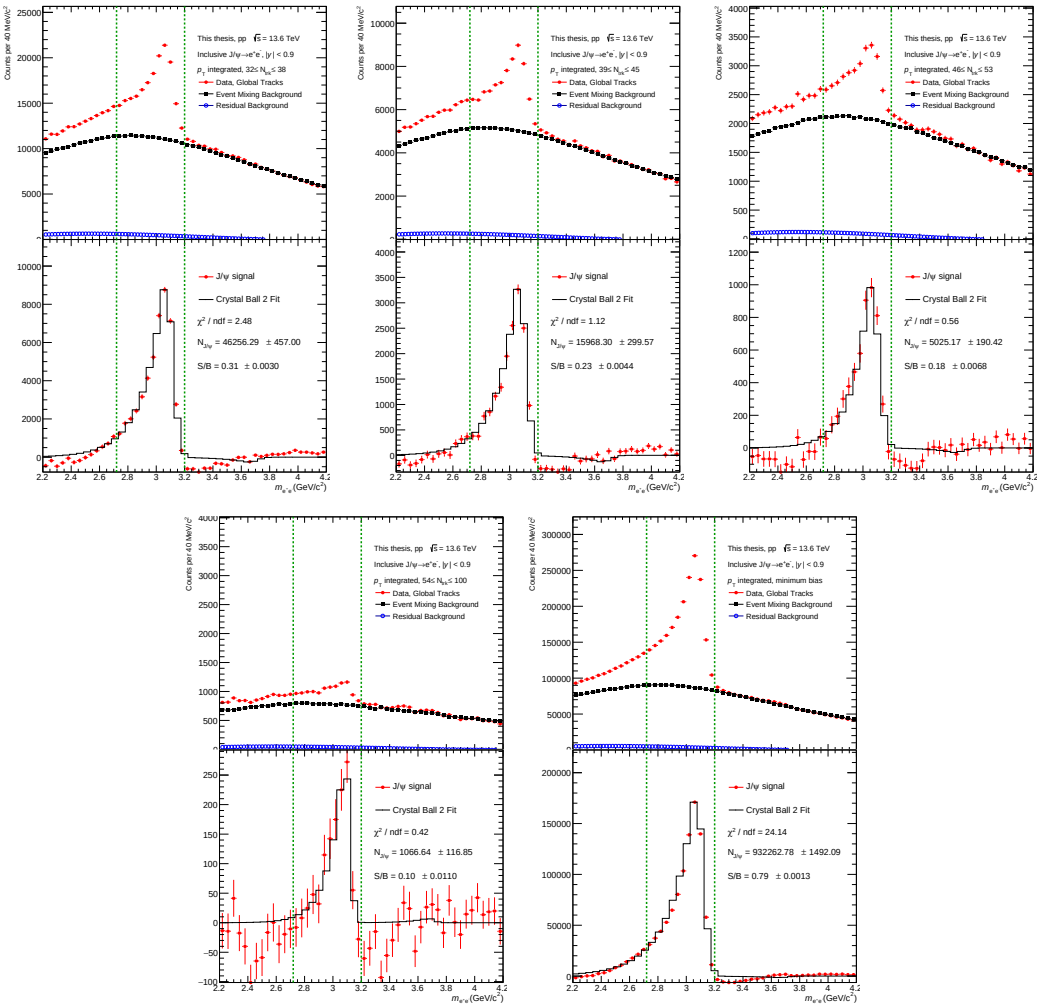


Figure A.2: Independent event cut efficiencies for the used event selection cuts: sel8 trigger, vertex, kIsGoodZvtxFT0VsPV, kIsVertexTOFMatched, kNoSameBunchPileup, and kIsVertexITSTPC

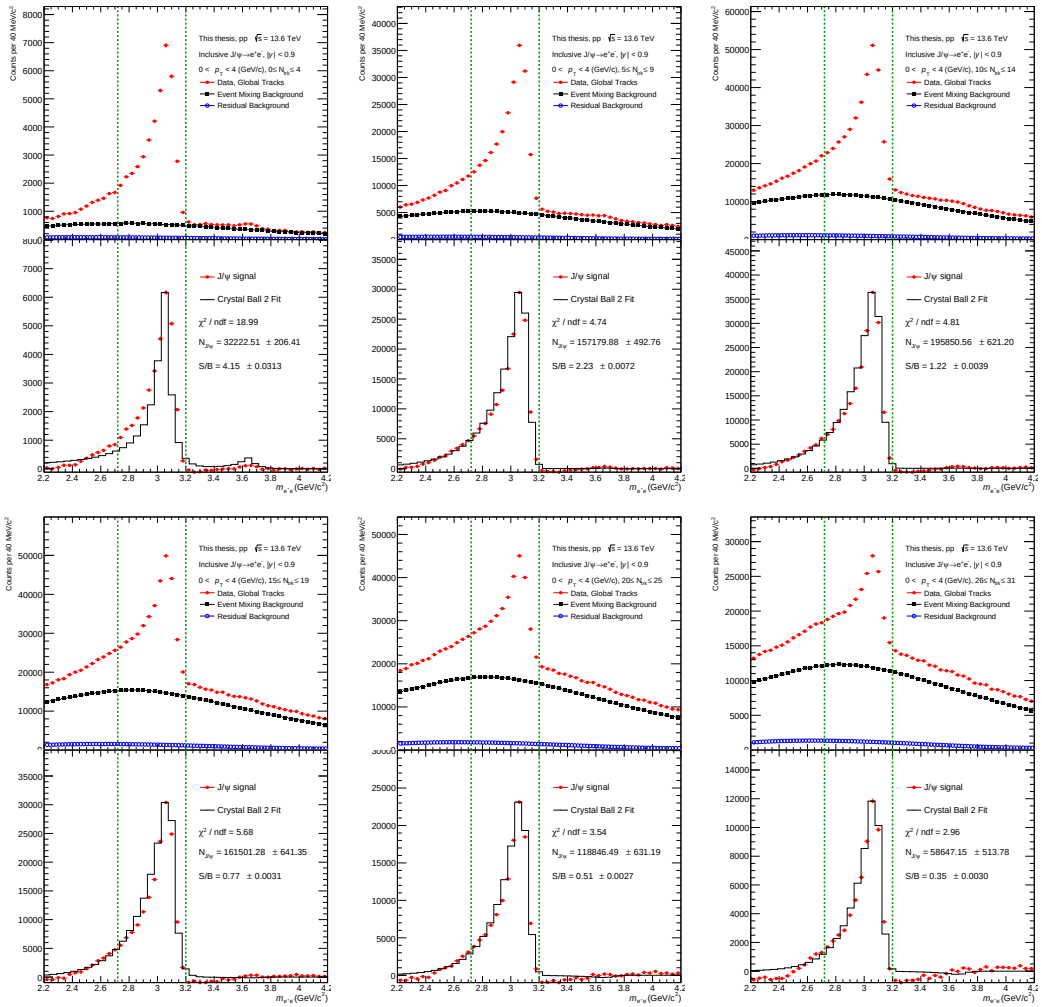
A.4 Global Track Invariant Mass Distributions

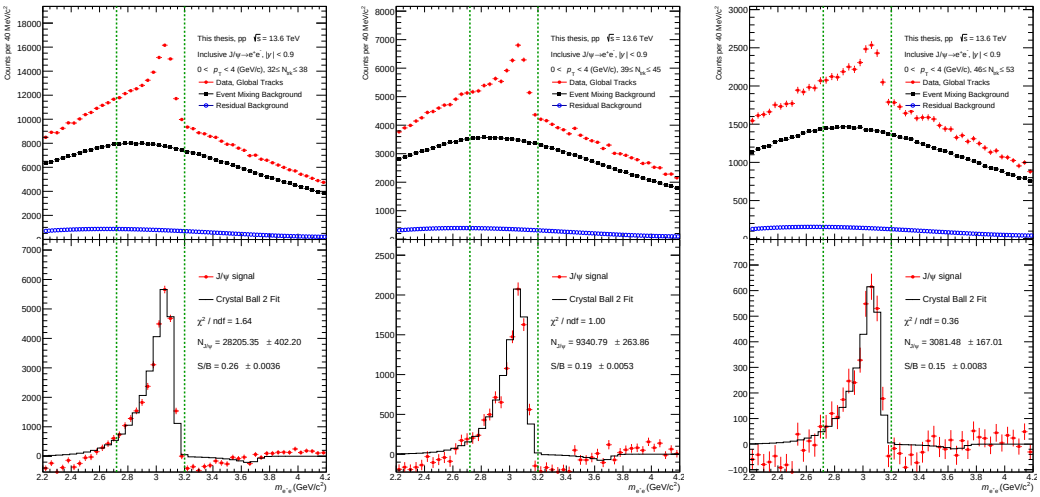
p_{T} integrated:



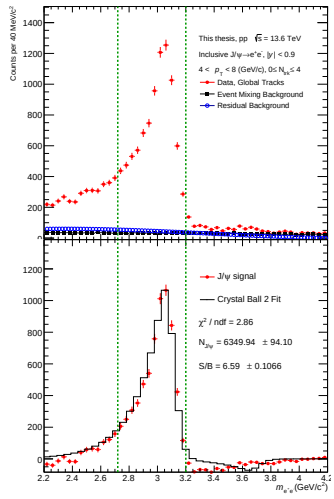

This thesis, pp $\sqrt{s}$ = 13.6 TeV
Inclusive J/ψ→e⁺e⁻, |y| < 0.9
p_T integrated, 32≤ N_{tks} ≤ 38
Data, Global Tracks
Event Mixing Background
Residual Background
J/ψ signal
Crystal Ball 2 Fit
χ^2 / ndf = 2.48
$N_{J/\psi}$ = 46256.29 ± 457.00
S/B = 0.31 ± 0.0030
This thesis, pp $\sqrt{s}$ = 13.6 TeV
Inclusive J/ψ→e⁺e⁻, |y| < 0.9
p_T integrated, 39≤ N_{tks} ≤ 45
Data, Global Tracks
Event Mixing Background
Residual Background
J/ψ signal
Crystal Ball 2 Fit
χ^2 / ndf = 1.12
$N_{J/\psi}$ = 15968.30 ± 299.57
S/B = 0.23 ± 0.0044
This thesis, pp $\sqrt{s}$ = 13.6 TeV
Inclusive J/ψ→e⁺e⁻, |y| < 0.9
p_T integrated, 46≤ N_{tks} ≤ 53
Data, Global Tracks
Event Mixing Background
Residual Background
J/ψ signal
Crystal Ball 2 Fit
χ^2 / ndf = 0.56
$N_{J/\psi}$ = 5025.17 ± 190.42
S/B = 0.18 ± 0.0068
This thesis, pp $\sqrt{s}$ = 13.6 TeV
Inclusive J/ψ→e⁺e⁻, |y| < 0.9
p_T integrated, 54≤ N_{tks} ≤ 100
Data, Global Tracks
Event Mixing Background
Residual Background
J/ψ signal
Crystal Ball 2 Fit
χ^2 / ndf = 0.42
$N_{J/\psi}$ = 1066.64 ± 116.85
S/B = 0.10 ± 0.0110
This thesis, pp $\sqrt{s}$ = 13.6 TeV
Inclusive J/ψ→e⁺e⁻, |y| < 0.9
p_T integrated, minimum bias
Data, Global Tracks
Event Mixing Background
Residual Background
J/ψ signal
Crystal Ball 2 Fit
χ^2 / ndf = 24.14
$N_{J/\psi}$ = 932262.78 ± 1492.09
S/B = 0.79 ± 0.0013
Counts per 40 MeV/c²
$m_{e^+e^-}$(GeV/c²)

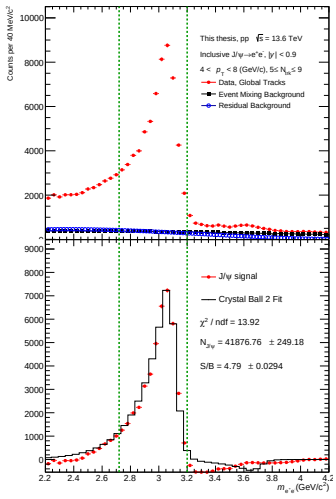
$0 < p_{\mathrm{T}} < 4\,\mathrm{GeV/c}$:

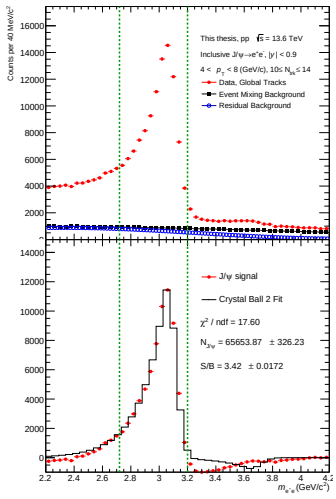


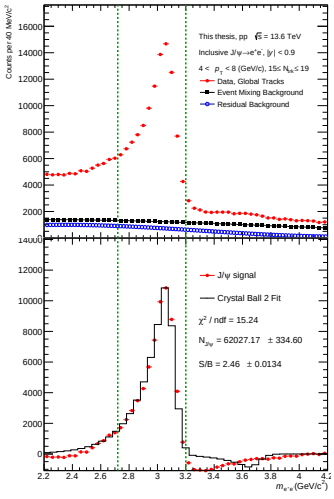

This thesis, pp $\sqrt{s}$ = 13.6 TeV
Inclusive J/ψ→e⁺e⁻, |y| < 0.9
0 < p_T < 4 (GeV/c), 32≤ N_{tk} ≤ 38
Data, Global Tracks
Event Mixing Background
Residual Background
J/ψ signal
Crystal Ball 2 Fit
χ^2 / ndf = 1.64
$N_{J/\psi}$ = 28205.35 ± 402.20
S/B = 0.26 ± 0.0036
Counts per 40 MeV/c²
$m_{e^+e^-}$(GeV/c²)
This thesis, pp $\sqrt{s}$ = 13.6 TeV
Inclusive J/ψ→e⁺e⁻, |y| < 0.9
0 < p_T < 4 (GeV/c), 39≤ N_{tk} ≤ 45
Data, Global Tracks
Event Mixing Background
Residual Background
J/ψ signal
Crystal Ball 2 Fit
χ^2 / ndf = 1.00
$N_{J/\psi}$ = 9340.79 ± 263.86
S/B = 0.19 ± 0.0053
Counts per 40 MeV/c²
$m_{e^+e^-}$(GeV/c²)
This thesis, pp $\sqrt{s}$ = 13.6 TeV
Inclusive J/ψ→e⁺e⁻, |y| < 0.9
0 < p_T < 4 (GeV/c), 46≤ N_{tk} ≤ 53
Data, Global Tracks
Event Mixing Background
Residual Background
J/ψ signal
Crystal Ball 2 Fit
χ^2 / ndf = 0.36
$N_{J/\psi}$ = 3081.48 ± 167.01
S/B = 0.15 ± 0.0083
Counts per 40 MeV/c²
$m_{e^+e^-}$(GeV/c²)
This thesis, pp $\sqrt{s}$ = 13.6 TeV
Inclusive J/ψ→e⁺e⁻, |y| < 0.9
0 < p_T < 4 (GeV/c), 54≤ N_{tk} ≤ 100
Data, Global Tracks
Event Mixing Background
Residual Background
J/ψ signal
Crystal Ball 2 Fit
χ^2 / ndf = 0.39
$N_{J/\psi}$ = 355.71 ± 101.46
S/B = 0.05 ± 0.0134
Counts per 40 MeV/c²
$m_{e^+e^-}$(GeV/c²)
This thesis, pp $\sqrt{s}$ = 13.6 TeV
Inclusive J/ψ→e⁺e⁻, |y| < 0.9
0 < p_T < 4 (GeV/c), minimum bias
Data, Global Tracks
Event Mixing Background
Residual Background
J/ψ signal
Crystal Ball 2 Fit
χ^2 / ndf = 17.24
$N_{J/\psi}$ = 642902.86 ± 1305.53
S/B = 0.73 ± 0.0015
Counts per 40 MeV/c²
$m_{e^+e^-}$(GeV/c²)

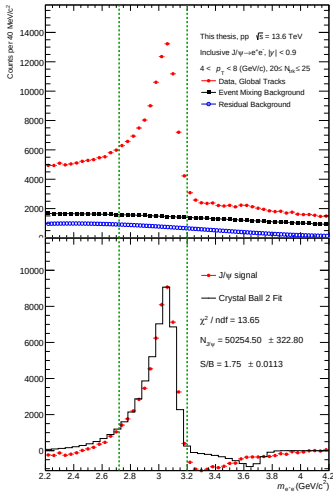
$4 < p_{\mathrm{T}} < 8\,\mathrm{GeV/c}$

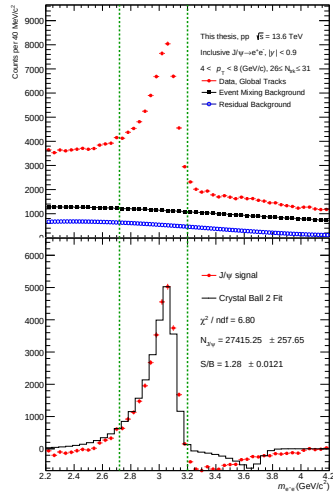


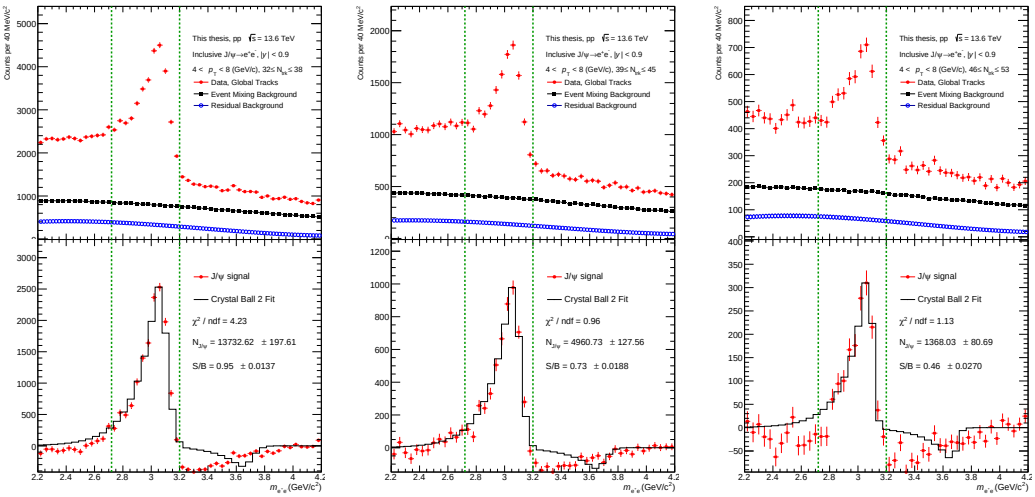




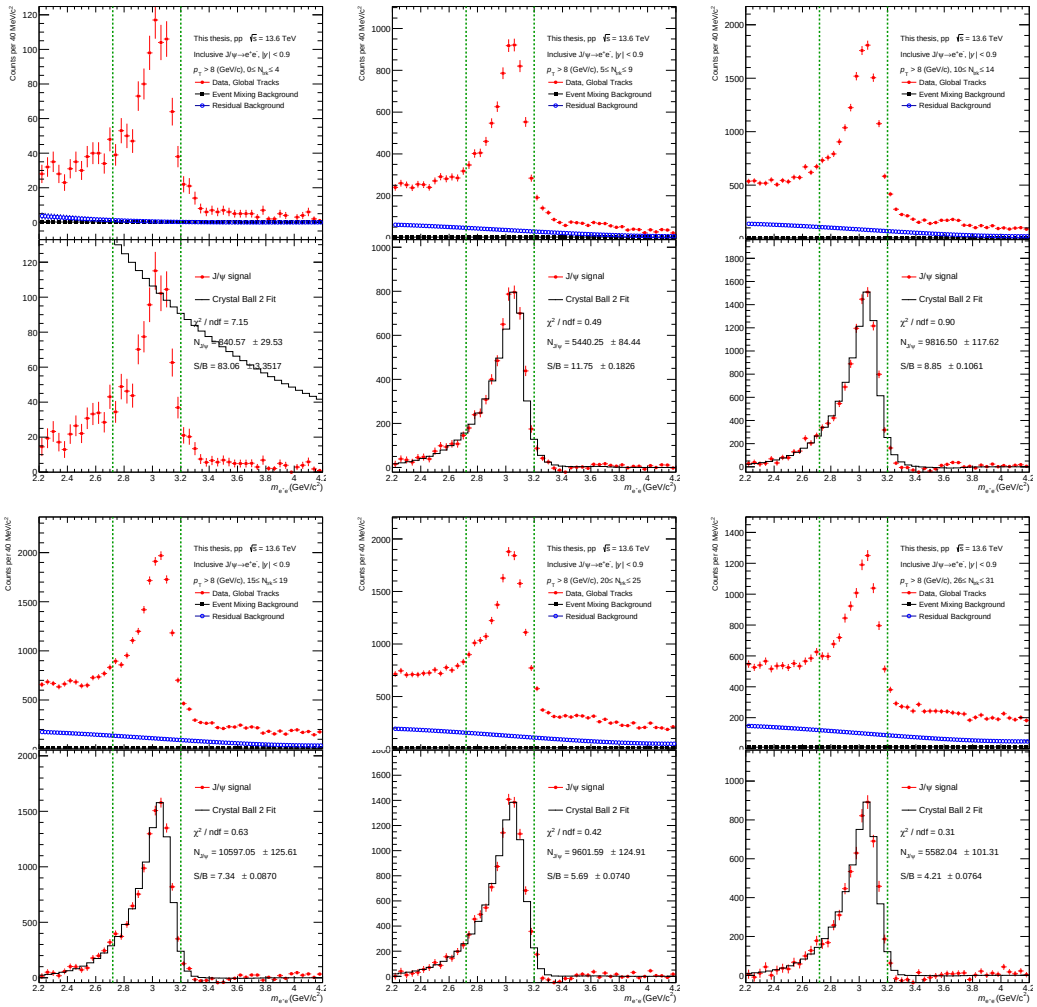


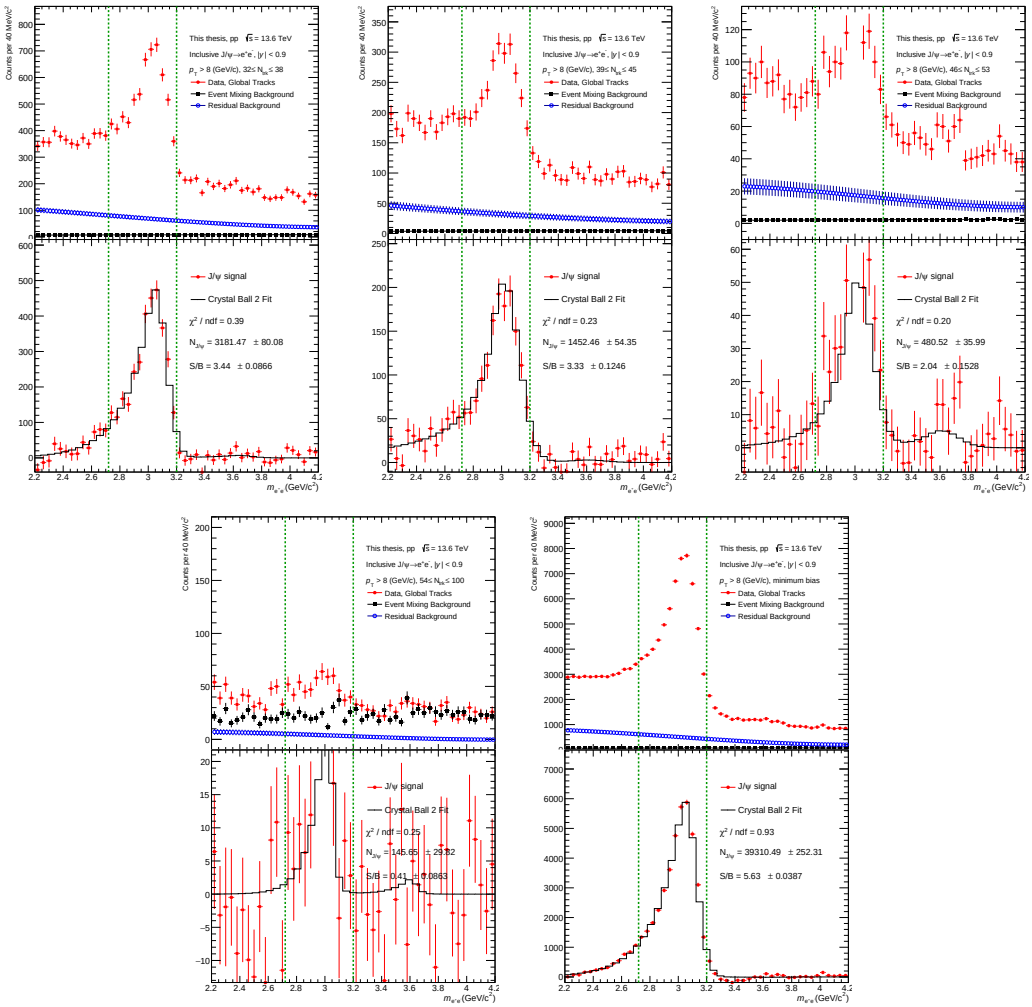





This thesis, pp $\sqrt{s}$ = 13.6 TeV
Inclusive J/ψ→e⁺e⁻, |y| < 0.9
4 < p_T < 8 (GeV/c), 32≤ N_{tk} ≤ 38
Data, Global Tracks
Event Mixing Background
Residual Background
J/ψ signal
Crystal Ball 2 Fit
χ^2 / ndf = 4.23
$N_{J/\psi}$ = 13732.62 ± 197.61
S/B = 0.95 ± 0.0137
Counts per 40 MeV/c²
$m_{e^+e^-}$(GeV/c²)
This thesis, pp $\sqrt{s}$ = 13.6 TeV
Inclusive J/ψ→e⁺e⁻, |y| < 0.9
4 < p_T < 8 (GeV/c), 39≤ N_{tk} ≤ 45
Data, Global Tracks
Event Mixing Background
Residual Background
J/ψ signal
Crystal Ball 2 Fit
χ^2 / ndf = 0.96
$N_{J/\psi}$ = 4960.73 ± 127.56
S/B = 0.73 ± 0.0188
Counts per 40 MeV/c²
$m_{e^+e^-}$(GeV/c²)
This thesis, pp $\sqrt{s}$ = 13.6 TeV
Inclusive J/ψ→e⁺e⁻, |y| < 0.9
4 < p_T < 8 (GeV/c), 46≤ N_{tk} ≤ 53
Data, Global Tracks
Event Mixing Background
Residual Background
J/ψ signal
Crystal Ball 2 Fit
χ^2 / ndf = 1.13
$N_{J/\psi}$ = 1368.03 ± 80.69
S/B = 0.46 ± 0.0270
Counts per 40 MeV/c²
$m_{e^+e^-}$(GeV/c²)
This thesis, pp $\sqrt{s}$ = 13.6 TeV
Inclusive J/ψ→e⁺e⁻, |y| < 0.9
4 < p_T < 8 (GeV/c), 54≤ N_{tk} ≤ 100
Data, Global Tracks
Event Mixing Background
Residual Background
J/ψ signal
Crystal Ball 2 Fit
χ^2 / ndf = 0.29
$N_{J/\psi}$ = 516.34 ± 50.05
S/B = 0.42 ± 0.0409
Counts per 40 MeV/c²
$m_{e^+e^-}$(GeV/c²)
This thesis, pp $\sqrt{s}$ = 13.6 TeV
Inclusive J/ψ→e⁺e⁻, |y| < 0.9
4 < p_T < 8 (GeV/c), minimum bias
Data, Global Tracks
Event Mixing Background
Residual Background
J/ψ signal
Crystal Ball 2 Fit
χ^2 / ndf = 54.41
$N_{J/\psi}$ = 230783.91 ± 665.88
S/B = 2.09 ± 0.0061
Counts per 40 MeV/c²
$m_{e^+e^-}$(GeV/c²)

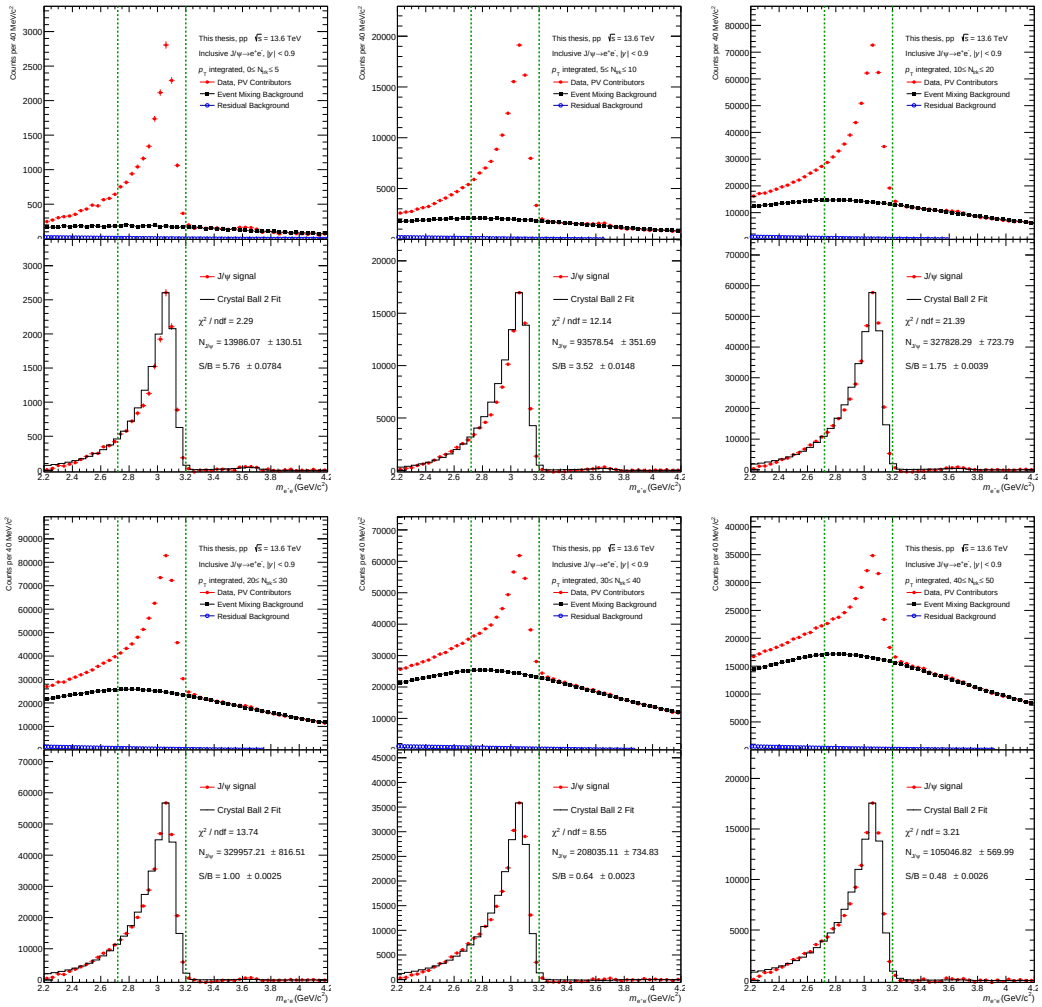
$p_{\mathrm{T}} > 8\,\mathrm{GeV/c}$:

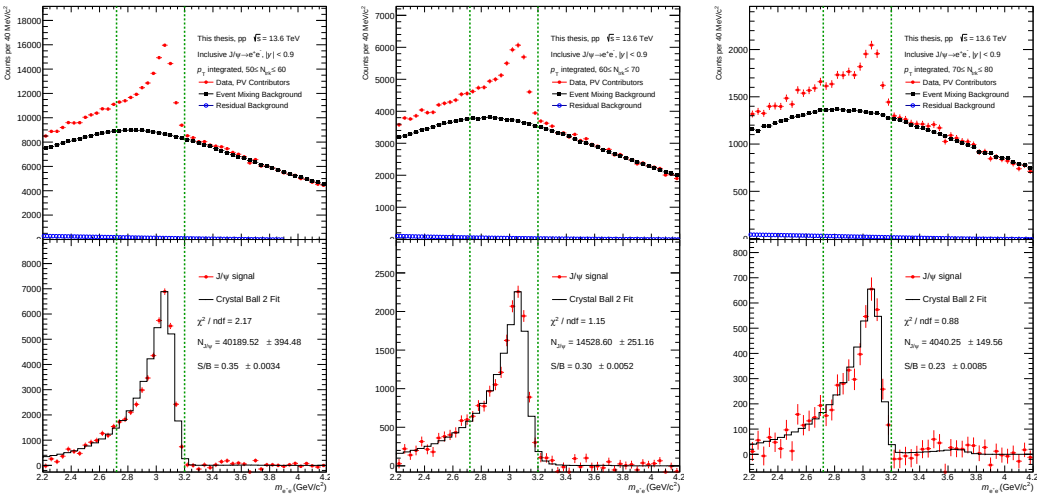



This thesis, pp $\sqrt{s}$ = 13.6 TeV
Inclusive J/ψ→e⁺e⁻, |y| < 0.9
p_T > 8 (GeV/c), 32≤ N_{trk} ≤ 38
Data, Global Tracks
Event Mixing Background
Residual Background
J/ψ signal
Crystal Ball 2 Fit
χ^2 / ndf = 0.39
$N_{J/\psi}$ = 3181.47 ± 80.08
S/B = 3.44 ± 0.0866
Counts per 40 MeV/c²
$m_{e^+e^-}$(GeV/c²)
This thesis, pp $\sqrt{s}$ = 13.6 TeV
Inclusive J/ψ→e⁺e⁻, |y| < 0.9
p_T > 8 (GeV/c), 39≤ N_{trk} ≤ 45
Data, Global Tracks
Event Mixing Background
Residual Background
J/ψ signal
Crystal Ball 2 Fit
χ^2 / ndf = 0.23
$N_{J/\psi}$ = 1452.46 ± 54.35
S/B = 3.33 ± 0.1246
Counts per 40 MeV/c²
$m_{e^+e^-}$(GeV/c²)
This thesis, pp $\sqrt{s}$ = 13.6 TeV
Inclusive J/ψ→e⁺e⁻, |y| < 0.9
p_T > 8 (GeV/c), 46≤ N_{trk} ≤ 53
Data, Global Tracks
Event Mixing Background
Residual Background
J/ψ signal
Crystal Ball 2 Fit
χ^2 / ndf = 0.20
$N_{J/\psi}$ = 480.52 ± 35.99
S/B = 2.04 ± 0.1528
Counts per 40 MeV/c²
$m_{e^+e^-}$(GeV/c²)
This thesis, pp $\sqrt{s}$ = 13.6 TeV
Inclusive J/ψ→e⁺e⁻, |y| < 0.9
p_T > 8 (GeV/c), 54≤ N_{trk} ≤ 100
Data, Global Tracks
Event Mixing Background
Residual Background
J/ψ signal
Crystal Ball 2 Fit
χ^2 / ndf = 0.25
$N_{J/\psi}$ = 145.65 ± 29.82
S/B = 0.41 ± 0.0863
Counts per 40 MeV/c²
$m_{e^+e^-}$(GeV/c²)
This thesis, pp $\sqrt{s}$ = 13.6 TeV
Inclusive J/ψ→e⁺e⁻, |y| < 0.9
p_T > 8 (GeV/c), minimum bias
Data, Global Tracks
Event Mixing Background
Residual Background
J/ψ signal
Crystal Ball 2 Fit
χ^2 / ndf = 0.93
$N_{J/\psi}$ = 39310.49 ± 252.31
S/B = 5.63 ± 0.0387
Counts per 40 MeV/c²
$m_{e^+e^-}$(GeV/c²)

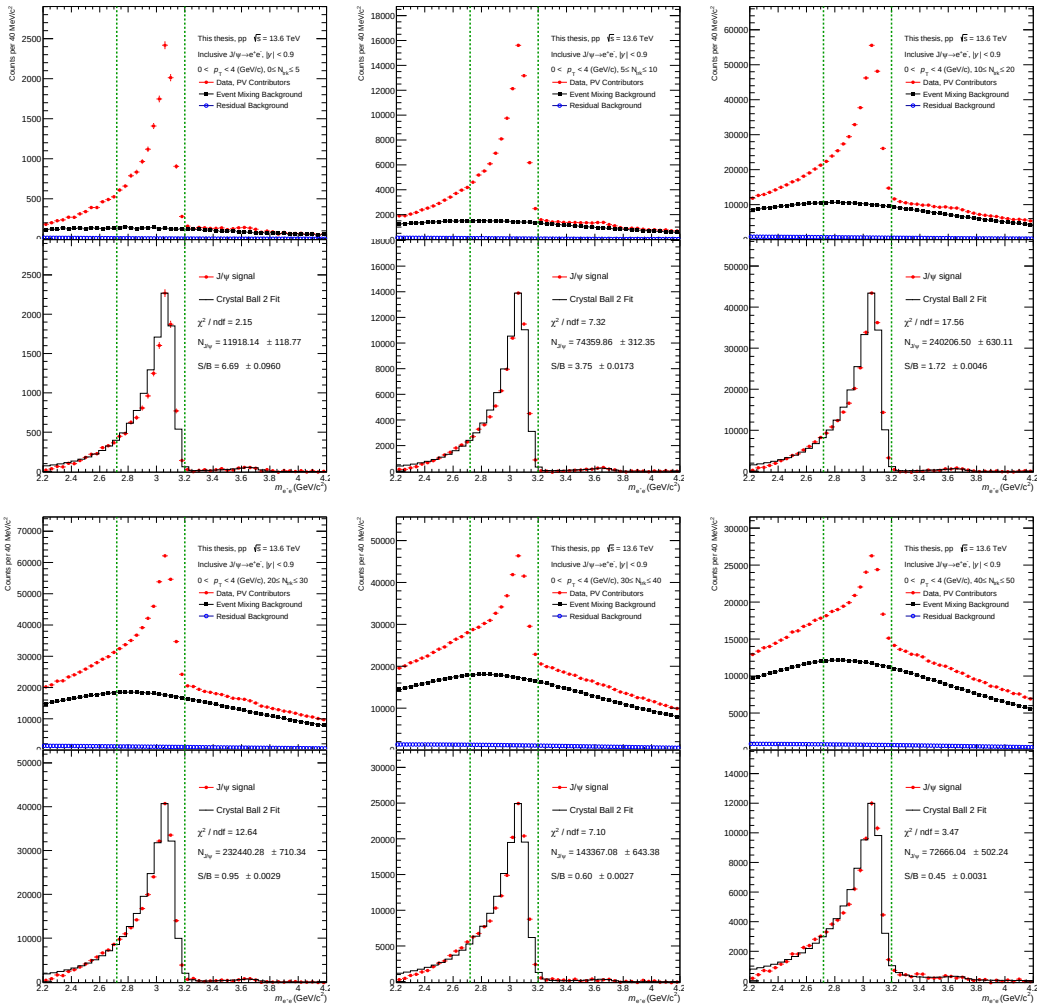
A.5 PV Contributors Invariant Mass Distributions

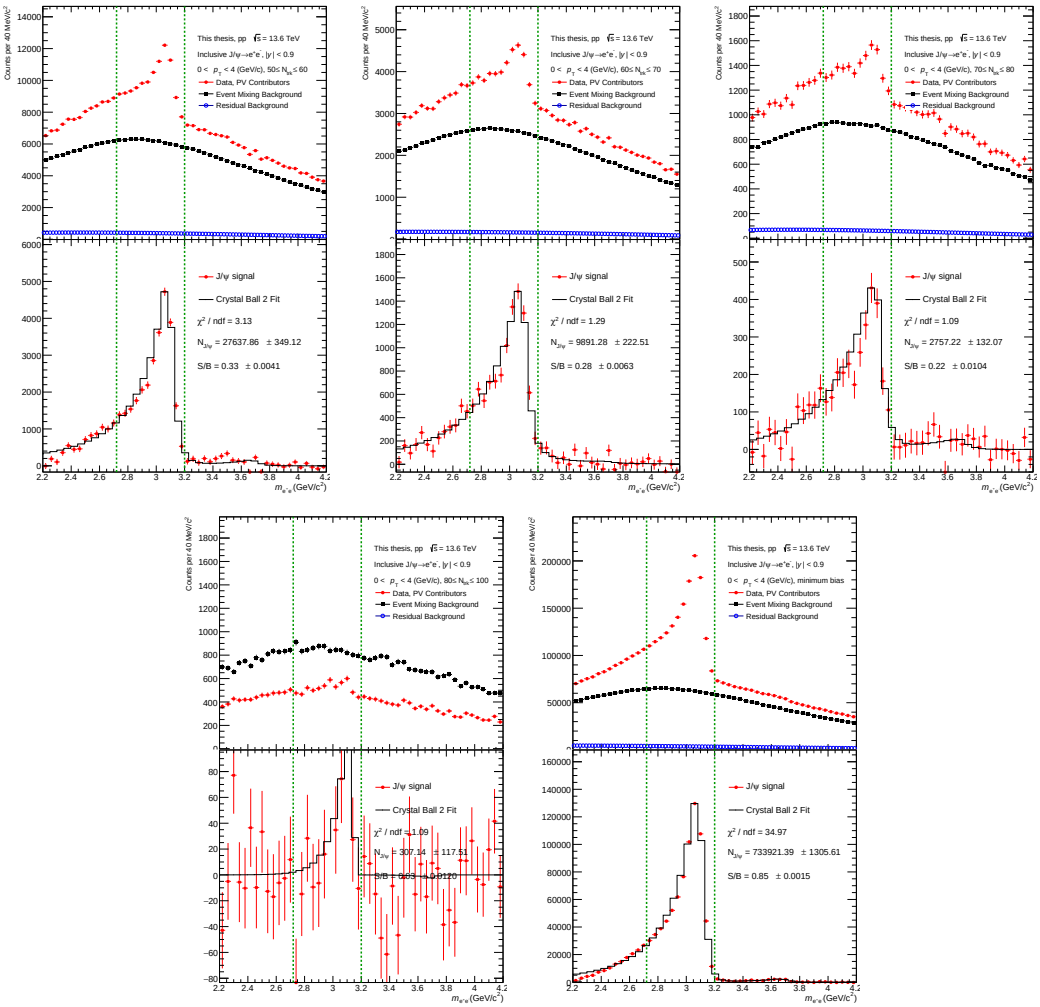
p_{T} integrated:



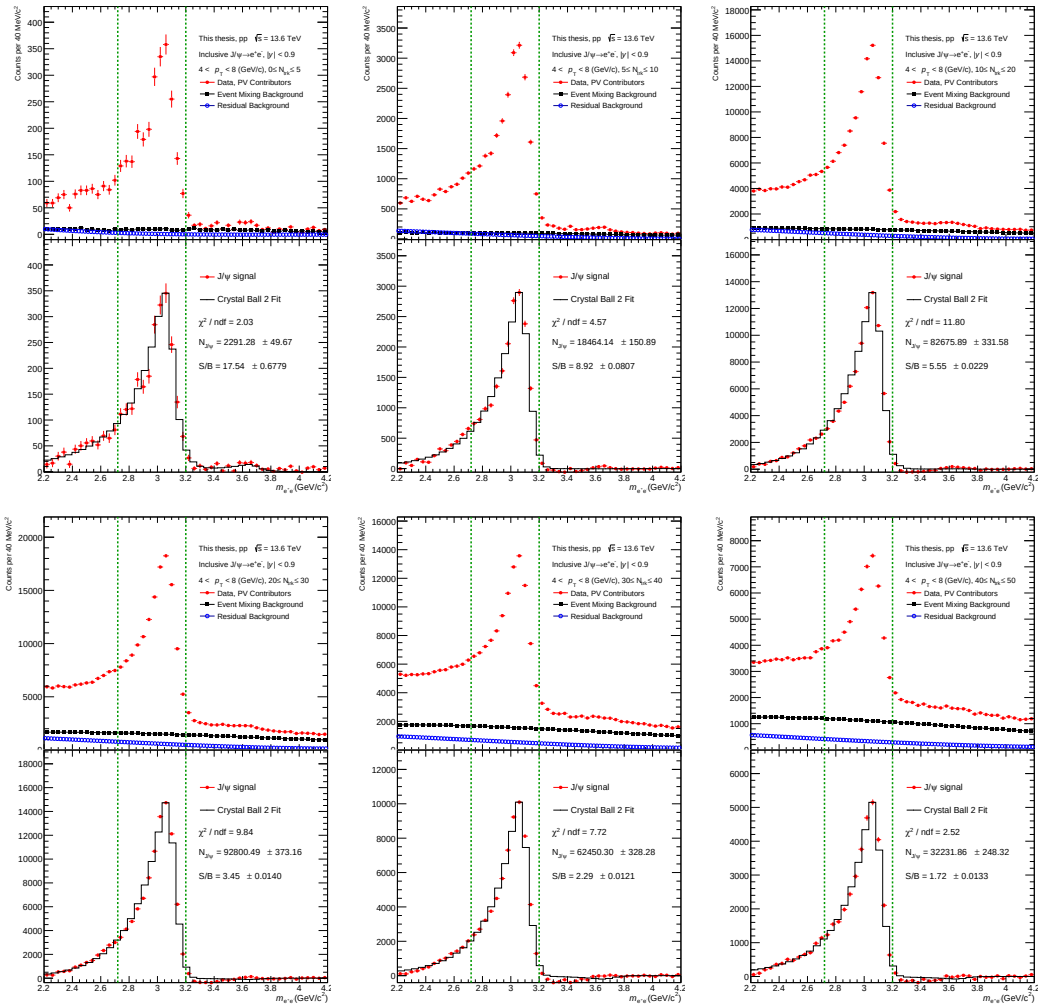

This thesis, pp $\sqrt{s}$ = 13.6 TeV
Inclusive J/ψ→e⁺e⁻, |y| < 0.9
p_T integrated, 50≤ N_{ch} ≤ 60
Data, PV Contributors
Event Mixing Background
Residual Background
J/ψ signal
Crystal Ball 2 Fit
χ^2 / ndf = 2.17
$N_{J/\psi}$ = 40189.52 ± 394.48
S/B = 0.35 ± 0.0034
Counts per 40 MeV/c²
$m_{e^+e^-}$(GeV/c²)
This thesis, pp $\sqrt{s}$ = 13.6 TeV
Inclusive J/ψ→e⁺e⁻, |y| < 0.9
p_T integrated, 60≤ N_{ch} ≤ 70
Data, PV Contributors
Event Mixing Background
Residual Background
J/ψ signal
Crystal Ball 2 Fit
χ^2 / ndf = 1.15
$N_{J/\psi}$ = 14528.60 ± 251.16
S/B = 0.30 ± 0.0052
Counts per 40 MeV/c²
$m_{e^+e^-}$(GeV/c²)
This thesis, pp $\sqrt{s}$ = 13.6 TeV
Inclusive J/ψ→e⁺e⁻, |y| < 0.9
p_T integrated, 70≤ N_{ch} ≤ 80
Data, PV Contributors
Event Mixing Background
Residual Background
J/ψ signal
Crystal Ball 2 Fit
χ^2 / ndf = 0.88
$N_{J/\psi}$ = 4040.25 ± 149.56
S/B = 0.23 ± 0.0085
Counts per 40 MeV/c²
$m_{e^+e^-}$(GeV/c²)
This thesis, pp $\sqrt{s}$ = 13.6 TeV
Inclusive J/ψ→e⁺e⁻, |y| < 0.9
p_T integrated, 80≤ N_{ch} ≤ 100
Data, PV Contributors
Event Mixing Background
Residual Background
J/ψ signal
Crystal Ball 2 Fit
χ^2 / ndf = 0.93
$N_{J/\psi}$ = 1172.37 ± 97.20
S/B = 0.17 ± 0.0138
Counts per 40 MeV/c²
$m_{e^+e^-}$(GeV/c²)
This thesis, pp $\sqrt{s}$ = 13.6 TeV
Inclusive J/ψ→e⁺e⁻, |y| < 0.9
p_T integrated, minimum bias
Data, PV Contributors
Event Mixing Background
Residual Background
J/ψ signal
Crystal Ball 2 Fit
χ^2 / ndf = 39.14
$N_{J/\psi}$ = 1026521.39 ± 1488.47
S/B = 0.88 ± 0.0013
Counts per 40 MeV/c²
$m_{e^+e^-}$(GeV/c²)

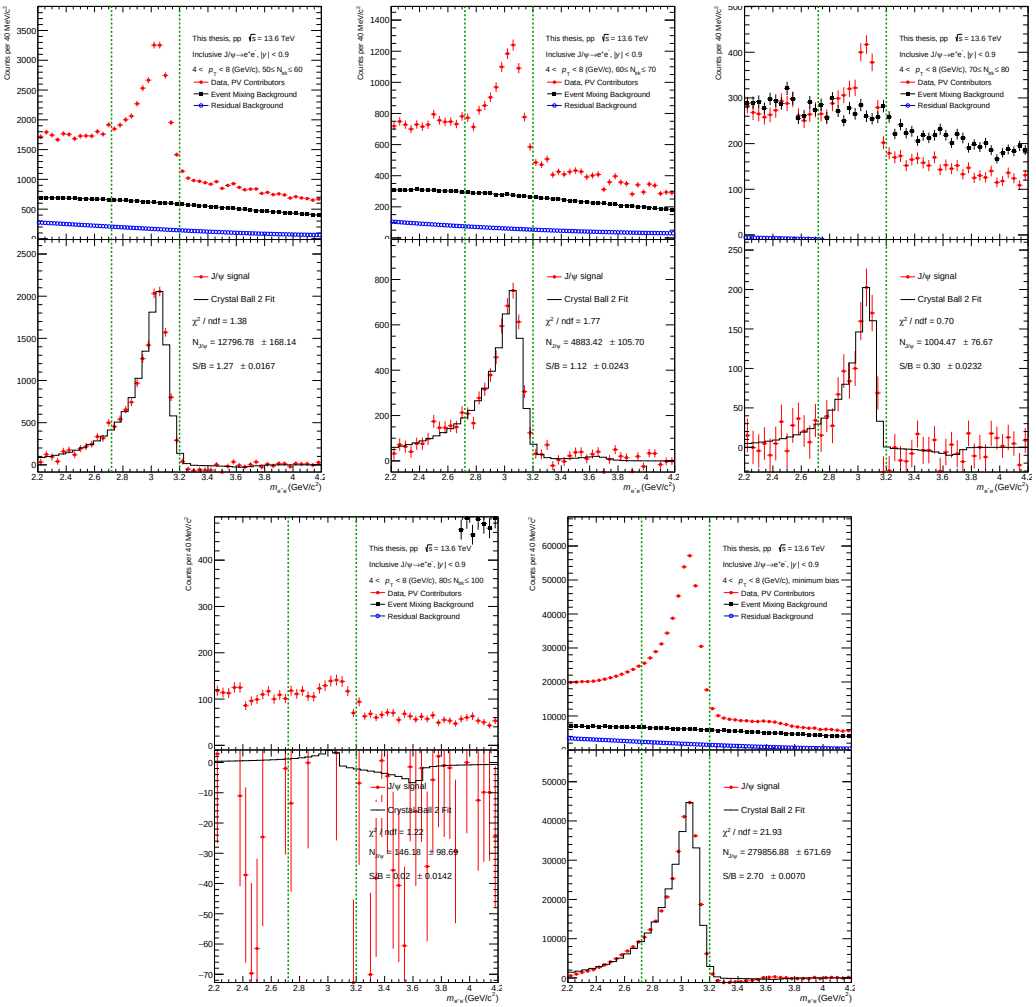
$0 < p_{\mathrm{T}} < 4\,\mathrm{GeV/c}$:



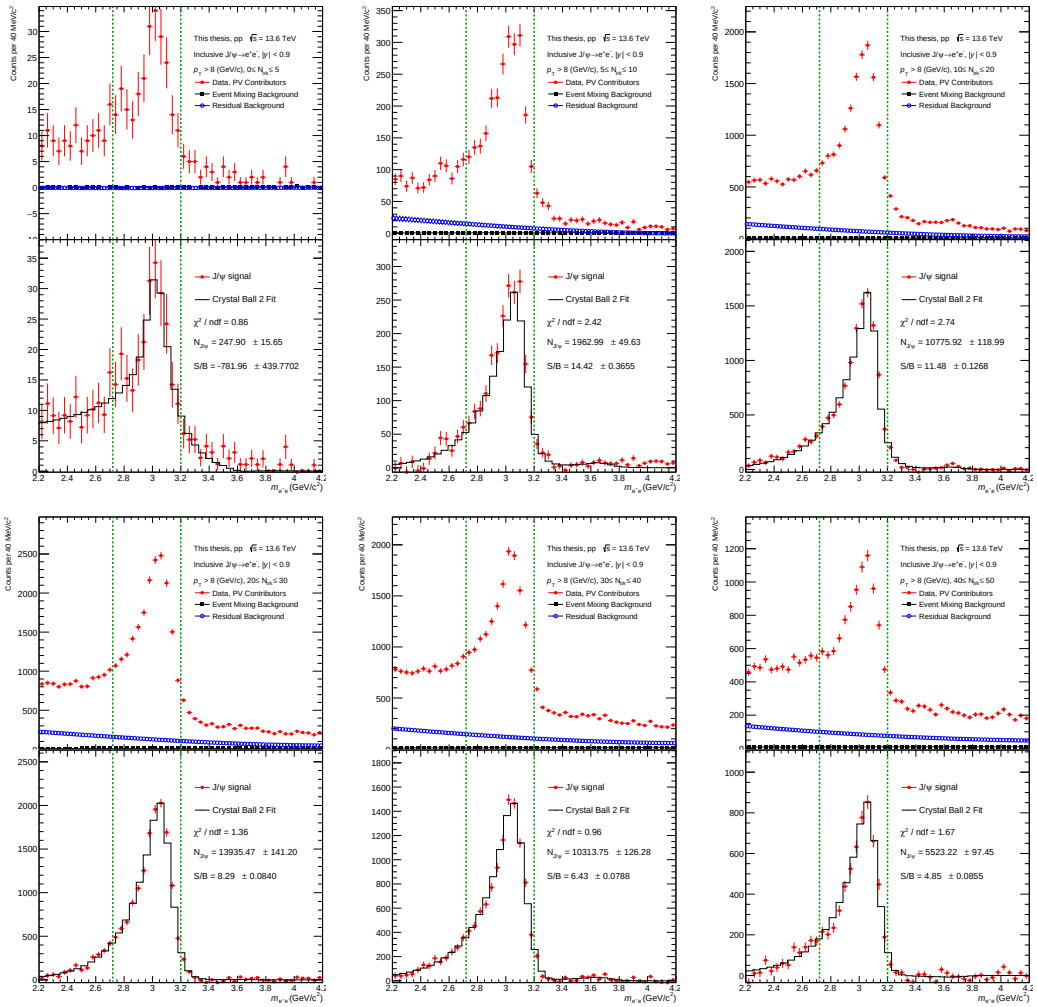

This thesis, pp $\sqrt{s}$ = 13.6 TeV
Inclusive J/ψ→e⁺e⁻, |y| < 0.9
0 < p_T < 4 (GeV/c), 50≤ N_{ch} ≤ 60
Data, PV Contributors
Event Mixing Background
Residual Background
J/ψ signal
Crystal Ball 2 Fit
χ^2 / ndf = 3.13
$N_{J/\psi}$ = 27637.86 ± 349.12
S/B = 0.33 ± 0.0041
Counts per 40 MeV/c²
$m_{e^+e^-}$(GeV/c²)
This thesis, pp $\sqrt{s}$ = 13.6 TeV
Inclusive J/ψ→e⁺e⁻, |y| < 0.9
0 < p_T < 4 (GeV/c), 60≤ N_{ch} ≤ 70
Data, PV Contributors
Event Mixing Background
Residual Background
J/ψ signal
Crystal Ball 2 Fit
χ^2 / ndf = 1.29
$N_{J/\psi}$ = 9891.28 ± 222.51
S/B = 0.28 ± 0.0063
Counts per 40 MeV/c²
$m_{e^+e^-}$(GeV/c²)
This thesis, pp $\sqrt{s}$ = 13.6 TeV
Inclusive J/ψ→e⁺e⁻, |y| < 0.9
0 < p_T < 4 (GeV/c), 70≤ N_{ch} ≤ 80
Data, PV Contributors
Event Mixing Background
Residual Background
J/ψ signal
Crystal Ball 2 Fit
χ^2 / ndf = 1.09
$N_{J/\psi}$ = 2757.22 ± 132.07
S/B = 0.22 ± 0.0104
Counts per 40 MeV/c²
$m_{e^+e^-}$(GeV/c²)
This thesis, pp $\sqrt{s}$ = 13.6 TeV
Inclusive J/ψ→e⁺e⁻, |y| < 0.9
0 < p_T < 4 (GeV/c), 80≤ N_{ch} ≤ 100
Data, PV Contributors
Event Mixing Background
Residual Background
J/ψ signal
Crystal Ball 2 Fit
χ^2 / ndf = 1.09
$N_{J/\psi}$ = 307.34 ± 117.51
S/B = 0.03 ± 0.0120
Counts per 40 MeV/c²
$m_{e^+e^-}$(GeV/c²)
This thesis, pp $\sqrt{s}$ = 13.6 TeV
Inclusive J/ψ→e⁺e⁻, |y| < 0.9
0 < p_T < 4 (GeV/c), minimum bias
Data, PV Contributors
Event Mixing Background
Residual Background
J/ψ signal
Crystal Ball 2 Fit
χ^2 / ndf = 34.97
$N_{J/\psi}$ = 733921.39 ± 1305.61
S/B = 0.85 ± 0.0015
Counts per 40 MeV/c²
$m_{e^+e^-}$(GeV/c²)

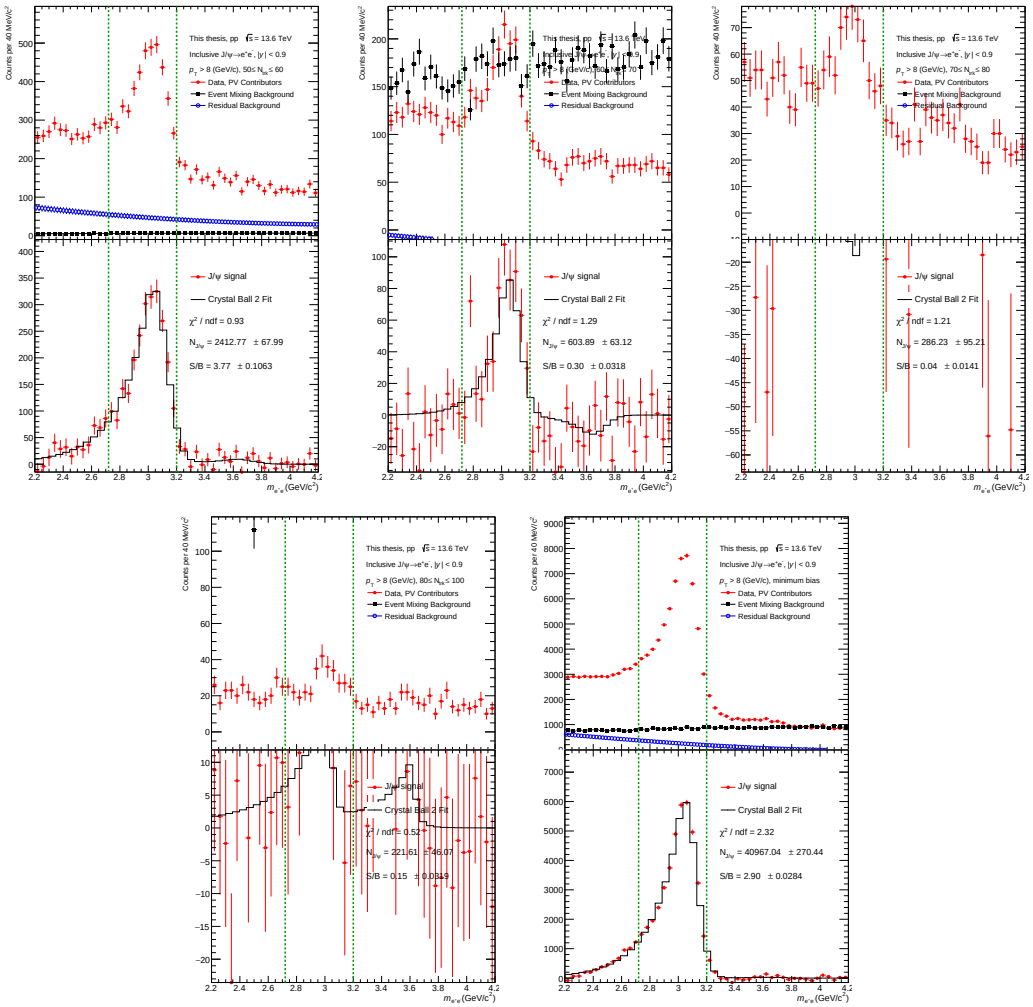
$4 < p_{\mathrm{T}} < 8\,\mathrm{GeV/c}$




This thesis, pp $\sqrt{s}$ = 13.6 TeV
Inclusive J/ψ→e⁺e⁻, |y| < 0.9
4 < p_T < 8 (GeV/c), 50≤ N_{ch} ≤ 60
Data, PV Contributors
Event Mixing Background
Residual Background
J/ψ signal
Crystal Ball 2 Fit
χ^2 / ndf = 1.38
$N_{J/\psi}$ = 12796.78 ± 168.14
S/B = 1.27 ± 0.0167
Counts per 40 MeV/c²
$m_{e^+e^-}$(GeV/c²)
This thesis, pp $\sqrt{s}$ = 13.6 TeV
Inclusive J/ψ→e⁺e⁻, |y| < 0.9
4 < p_T < 8 (GeV/c), 60≤ N_{ch} ≤ 70
Data, PV Contributors
Event Mixing Background
Residual Background
J/ψ signal
Crystal Ball 2 Fit
χ^2 / ndf = 1.77
$N_{J/\psi}$ = 4883.42 ± 105.70
S/B = 1.12 ± 0.0243
Counts per 40 MeV/c²
$m_{e^+e^-}$(GeV/c²)
This thesis, pp $\sqrt{s}$ = 13.6 TeV
Inclusive J/ψ→e⁺e⁻, |y| < 0.9
4 < p_T < 8 (GeV/c), 70≤ N_{ch} ≤ 80
Data, PV Contributors
Event Mixing Background
Residual Background
J/ψ signal
Crystal Ball 2 Fit
χ^2 / ndf = 0.70
$N_{J/\psi}$ = 1004.47 ± 76.67
S/B = 0.30 ± 0.0232
Counts per 40 MeV/c²
$m_{e^+e^-}$(GeV/c²)
This thesis, pp $\sqrt{s}$ = 13.6 TeV
Inclusive J/ψ→e⁺e⁻, |y| < 0.9
4 < p_T < 8 (GeV/c), 80≤ N_{ch} ≤ 100
Data, PV Contributors
Event Mixing Background
Residual Background
J/ψ signal
Crystal Ball 2 Fit
χ^2 / ndf = 1.22
$N_{J/\psi}$ = 146.18 ± 98.69
S/B = 0.02 ± 0.0142
Counts per 40 MeV/c²
$m_{e^+e^-}$(GeV/c²)
This thesis, pp $\sqrt{s}$ = 13.6 TeV
Inclusive J/ψ→e⁺e⁻, |y| < 0.9
4 < p_T < 8 (GeV/c), minimum bias
Data, PV Contributors
Event Mixing Background
Residual Background
J/ψ signal
Crystal Ball 2 Fit
χ^2 / ndf = 21.93
$N_{J/\psi}$ = 279856.88 ± 671.69
S/B = 2.70 ± 0.0070
Counts per 40 MeV/c²
$m_{e^+e^-}$(GeV/c²)

$p_{\mathrm{T}} > 8\,\mathrm{GeV/c}$:




This thesis, pp $\sqrt{s}$ = 13.6 TeV
Inclusive J/ψ→e⁺e⁻, |y| < 0.9
P_T > 8 (GeV/c), 50≤ N_{tks} ≤ 60
Data, PV Contributors
Event Mixing Background
Residual Background
J/ψ signal
Crystal Ball 2 Fit
χ² / ndf = 0.93
$N_{J/\psi}$ = 2412.77 ± 67.99
S/B = 3.77 ± 0.1063
P_T > 8 (GeV/c), 70≤ N_{tks} ≤ 80
χ² / ndf = 1.29
$N_{J/\psi}$ = 603.89 ± 63.12
S/B = 0.30 ± 0.0318
P_T > 8 (GeV/c), 80≤ N_{tks} ≤ 100
χ² / ndf = 1.21
$N_{J/\psi}$ = 286.23 ± 95.21
S/B = 0.04 ± 0.0141
P_T > 8 (GeV/c), 80≤ N_{tks} ≤ 100
χ² / ndf = 0.52
$N_{J/\psi}$ = 221.61 ± 46.07
S/B = 0.15 ± 0.0319
P_T > 8 (GeV/c), minimum bias
χ² / ndf = 2.32
$N_{J/\psi}$ = 40967.04 ± 270.44
S/B = 2.90 ± 0.0284
Counts per 40 MeV/c²
$m_{e^+e^-}$(GeV/c²)

A.6 Results for Different Production Years

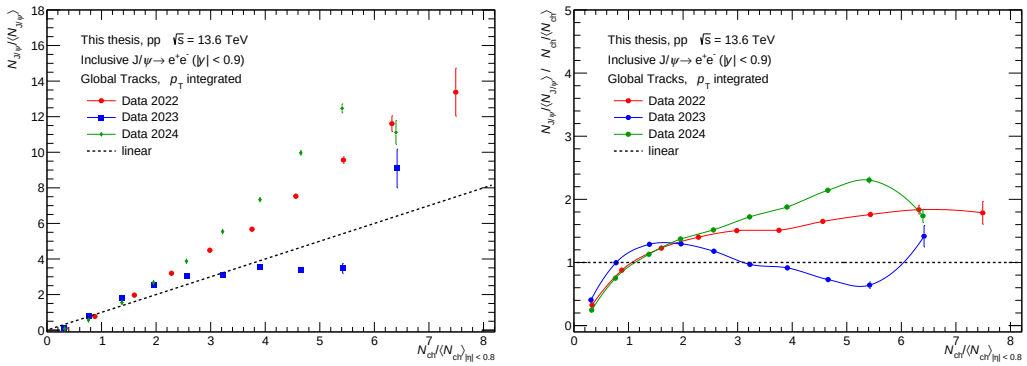


Figure A.3: Self-normalized, p_{T} integrated J/ψ yield as a function of the self-normalized charged-particle multiplicity, estimated from global tracks, for the three different run periods as well as the corresponding double ratio.

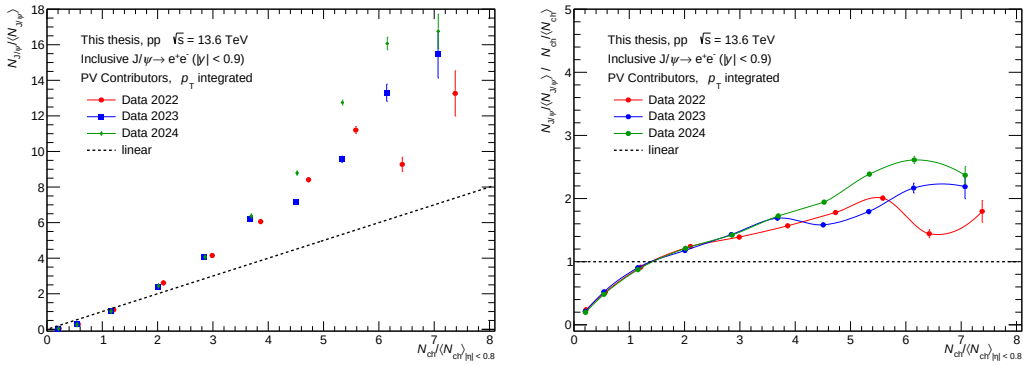


Figure A.4: Self-normalized, p_{T} integrated J/ψ yield as a function of the self-normalized charged-particle multiplicity, estimated from PV contributors, for the three different run periods as well as the corresponding double ratio.

Bibliography

[1] ALICE Collaboration. "Multiplicity dependence of inclusive J/ψ production at midrapidity in pp collisions at $\sqrt{s} = 13$ TeV". In: *Physics Letters B* 810 (Nov. 2020), p. 135758. ISSN: 0370-2693. DOI: 10.1016/j.physletb.2020.135758. URL: http://dx.doi.org/10.1016/j.physletb.2020.135758.

[2] Cush. *Standard model of elementary particles*. Sept. 2019. URL: https://en.wikipedia.org/wiki/File:Standard_Model_of_Elementary_Particles.svg (visited on 01/30/2025).

[3] KATRIN Collaboration. "Direct neutrino-mass measurement based on 259 days of KATRIN data". In: *Science* 388.6743 (2025), pp. 180–185. DOI: 10.1126/science.adq9592. eprint: https://www.science.org/doi/pdf/10.1126/science.adq9592. URL: https://www.science.org/doi/abs/10.1126/science.adq9592.

[4] Paul Langacker. "Structure of the Standard Model". In: (2003). arXiv: hep-ph/0304186 [hep-ph]. URL: https://arxiv.org/abs/hep-ph/0304186.

[5] T. S. van Albada et al. "Distribution of dark matter in the spiral galaxy NGC 3198." In: *Astrophysical Journal* 295 (Aug. 1985), pp. 305–313. DOI: 10.1086/163375.

[6] A. Pich. *Quantum Chromodynamics*. 1995. arXiv: hep-ph/9505231 [hep-ph]. URL: https://arxiv.org/abs/hep-ph/9505231.

[7] Mark Thomson. *Modern Particle Physics*. Cambridge University Press, 2013.

[8] David J. Gross and Frank Wilczek. "Ultraviolet Behavior of Non-Abelian Gauge Theories". In: *Phys. Rev. Lett.* 30 (26 June 1973), pp. 1343–1346. DOI: 10.1103/PhysRevLett.30.1343. URL: https://link.aps.org/doi/10.1103/PhysRevLett.30.1343.

[9] H. David Politzer. "Reliable Perturbative Results for Strong Interactions?" In: *Phys. Rev. Lett.* 30 (26 June 1973), pp. 1346–1349. DOI: 10.1103/PhysRevLett.30.1346. URL: https://link.aps.org/doi/10.1103/PhysRevLett.30.1346.

[10] Alekseev et al. "Observation of a $J^{\mathrm{PC}} = 1^{-+}$ Exotic Resonance in Diffractive Dissociation of $190\ \mathrm{GeV}/c\ \pi^-$ into $\pi^-\pi^-\pi^+$". In: *Phys. Rev. Lett.* 104 (24 June 2010), p. 241803. DOI: 10.1103/PhysRevLett.104.241803. URL: https://link.aps.org/doi/10.1103/PhysRevLett.104.241803.

[11] Jozef J. Dudek et al. "Toward the excited isoscalar meson spectrum from lattice QCD". In: *Phys. Rev. D* 88 (9 Nov. 2013), p. 094505. DOI: 10.1103/PhysRevD.88.094505. URL: https://link.aps.org/doi/10.1103/PhysRevD.88.094505.

[12] Particle Data Group Collaboration. "Review of Particle Physics". In: *Phys. Rev. D* 110 (3 Aug. 2024), p. 030001. DOI: 10.1103/PhysRevD.110.030001. URL: https://link.aps.org/doi/10.1103/PhysRevD.110.030001.

[13] Yuri L. Dokshitzer. "Calculation of the Structure Functions for Deep Inelastic Scattering and e+ e- Annihilation by Perturbation Theory in Quantum Chromodynamics." In: *Sov. Phys. JETP* 46 (1977), pp. 641–653.

[14] V. N. Gribov and L. N. Lipatov. "Deep inelastic e p scattering in perturbation theory". In: *Sov. J. Nucl. Phys.* 15 (1972), pp. 438–450.

[15] G. Altarelli and G. Parisi. "Asymptotic freedom in parton language". In: *Nuclear Physics B* 126.2 (1977), pp. 298–318. ISSN: 0550-3213. DOI: https://doi.org/10.1016/0550-3213(77)90384-4. URL: https://www.sciencedirect.com/science/article/pii/0550321377903844.

[16] Ball. "Parton distributions from high-precision collider data". In: *The European Physical Journal C* 77.10 (Oct. 2017), p. 663. ISSN: 1434-6052. DOI: 10.1140/epjc/s10052-017-5199-5. URL: https://doi.org/10.1140/epjc/s10052-017-5199-5.

[17] Ruth Pöttgen. "Proton-Proton Collisions". In: *Search for Dark Matter with ATLAS: Using Events with a Highly Energetic Jet and Missing Transverse Momentum in Proton-Proton Collisions at √s = 8 TeV* . Cham: Springer International Publishing, 2016, pp. 45–60. ISBN: 978-3-319-41045-6. DOI: 10.1007/978-3-319-41045-6_4. URL: https://doi.org/10.1007/978-3-319-41045-6_4.

[18] Jan Fiete Grosse-Oetringhaus and Klaus Reygers. *Charged-particle multiplicity in proton–proton collisions*. July 2010. DOI: 10.1088/0954-3899/37/8/083001. URL: http://dx.doi.org/10.1088/0954-3899/37/8/083001.

[19] A. L. I. C. E. Collaboration. "The ALICE experiment: a journey through QCD". In: *The European Physical Journal C* 84.8 (Aug. 2024), p. 813. ISSN: 1434-6052. DOI: 10.1140/epjc/s10052-024-12935-y. URL: https://doi.org/10.1140/epjc/s10052-024-12935-y.

[20] J. C. Collins and M. J. Perry. "Superdense Matter: Neutrons or Asymptotically Free Quarks?" In: *Phys. Rev. Lett.* 34 (21 May 1975), pp. 1353–1356. DOI: 10.1103/PhysRevLett.34.1353. URL: https://link.aps.org/doi/10.1103/PhysRevLett.34.1353.

[21] N. Cabibbo and G. Parisi. "Exponential hadronic spectrum and quark liberation". In: *Physics Letters B* 59.1 (1975), pp. 67–69. ISSN: 0370-2693. DOI: https://doi.org/10.1016/0370-2693(75)90158-6. URL: https://www.sciencedirect.com/science/article/pii/0370269375901586.

[22] Edward V. Shuryak. "Theory of Hadronic Plasma". In: *Sov. Phys. JETP* 47 (1978), pp. 212–219.

[23] E.V. Shuryak. “Quark-gluon plasma and hadronic production of leptons, photons and psions”. In: *Physics Letters B* 78.1 (1978), pp. 150–153. ISSN: 0370-2693. DOI: https://doi.org/10.1016/0370-2693(78)90370-2. URL: https://www.sciencedirect.com/science/article/pii/0370269378903702.

[24] John W. Harris and Berndt Müller. “”QGP Signatures” Revisited”. In: *Eur. Phys. J. C* 84.3 (2024), p. 247. DOI: 10.1140/epjc/s10052-024-12533-y. arXiv: 2308.05743 [hep-ph].

[25] ALICE Collaboration. “Measurement of transverse energy at midrapidity in Pb-Pb collisions at $\sqrt{s_{NN}} = 2.76$ TeV”. In: *Phys. Rev. C* 94 (3 Sept. 2016), p. 034903. DOI: 10.1103/PhysRevC.94.034903. URL: https://link.aps.org/doi/10.1103/PhysRevC.94.034903.

[26] Peter Braun-Munzinger and Johanna Stachel. “The quest for the quark–gluon plasma”. In: *Nature* 448.7151 (July 2007), pp. 302–309. ISSN: 1476-4687. DOI: 10.1038/nature06080. URL: https://doi.org/10.1038/nature06080.

[27] *The QCD Phase Diagram and Equation of State*. https://www.gauss-centre.eu/results/elementaryparticlephysics/the-qcd-phase-diagram-and-equation-of-state. Accessed: 11.03.2025.

[28] Taesoo Song, Kyong Chol Han, and Che Ming Ko. “Charmonium production in relativistic heavy-ion collisions”. In: *Phys. Rev. C* 84 (3 Sept. 2011), p. 034907. DOI: 10.1103/PhysRevC.84.034907. URL: https://link.aps.org/doi/10.1103/PhysRevC.84.034907.

[29] Louis Kluberg and Helmut Satz. “Color Deconfinement and Charmonium Production in Nuclear Collisions”. In: *Relativistic Heavy Ion Physics*. Ed. by R. Stock. 2010. DOI: 10.1007/978-3-642-01539-7_13. arXiv: 0901.3831 [hep-ph].

[30] Michael L. Miller et al. “Glauber Modeling in High-Energy Nuclear Collisions”. In: *Annual Review of Nuclear and Particle Science* 57.1 (Nov. 2007), pp. 205–243. ISSN: 1545-4134. DOI: 10.1146/annurev.nucl.57.090506.123020. URL: http://dx.doi.org/10.1146/annurev.nucl.57.090506.123020.

[31] “Studies of J/ψ production at forward rapidity in Pb–Pb collisions at $\sqrt{s_{\mathrm{NN}}} = 5.02$ TeV”. In: *Journal of High Energy Physics* 2020.2 (Feb. 2020). ISSN: 1029-8479. DOI: 10.1007/jhep02(2020)041. URL: http://dx.doi.org/10.1007/JHEP02(2020)041.

[32] CMS Collaboration. “Observation of long-range, near-side angular correlations in proton-proton collisions at the LHC”. In: *Journal of High Energy Physics* 2010.9 (Sept. 2010). ISSN: 1029-8479. DOI: 10.1007/jhep09(2010)091. URL: http://dx.doi.org/10.1007/JHEP09(2010)091.

[33] ALICE Collaboration. “Enhanced production of multi-strange hadrons in high-multiplicity proton–proton collisions”. In: *Nature Physics* 13.6 (Apr. 2017), pp. 535–539. ISSN: 1745-2481. DOI: 10.1038/nphys4111. URL: http://dx.doi.org/10.1038/nphys4111.

[34] Christian Bierlich. "Rope Hadronization and Strange Particle Production". In: *EPJ Web of Conferences* 171 (2018). Ed. by A. Mischke and P. Kuijer, p. 14003. ISSN: 2100-014X. DOI: 10.1051/epjconf/201817114003. URL: http://dx.doi.org/10.1051/epjconf/201817114003.

[35] A. Ortiz Velasquez et al. "Color Reconnection and Flowlike Patterns in pp Collisions". In: *Phys. Rev. Lett.* 111 (4 July 2013), p. 042001. DOI: 10.1103/PhysRevLett.111.042001. URL: https://link.aps.org/doi/10.1103/PhysRevLett.111.042001.

[36] Boris Blok et al. "Collectivity from interference". In: *Journal of High Energy Physics* 2017.12 (Dec. 2017). ISSN: 1029-8479. DOI: 10.1007/jhep12(2017)074. URL: http://dx.doi.org/10.1007/JHEP12(2017)074.

[37] Adrian Dumitru et al. "The ridge in proton–proton collisions at the LHC". In: *Physics Letters B* 697.1 (Feb. 2011), pp. 21–25. ISSN: 0370-2693. DOI: 10.1016/j.physletb.2011.01.024. URL: http://dx.doi.org/10.1016/j.physletb.2011.01.024.

[38] J. J. Aubert et al. "Experimental Observation of a Heavy Particle J". In: *Phys. Rev. Lett.* 33 (23 Dec. 1974), pp. 1404–1406. DOI: 10.1103/PhysRevLett.33.1404. URL: https://link.aps.org/doi/10.1103/PhysRevLett.33.1404.

[39] J. -E. Augustin et al. "Discovery of a Narrow Resonance in e^+e^- Annihilation". In: *Phys. Rev. Lett.* 33 (23 Dec. 1974), pp. 1406–1408. DOI: 10.1103/PhysRevLett.33.1406. URL: https://link.aps.org/doi/10.1103/PhysRevLett.33.1406.

[40] S. L. Glashow, J. Iliopoulos, and L. Maiani. "Weak Interactions with Lepton-Hadron Symmetry". In: *Phys. Rev. D* 2 (7 Oct. 1970), pp. 1285–1292. DOI: 10.1103/PhysRevD.2.1285. URL: https://link.aps.org/doi/10.1103/PhysRevD.2.1285.

[41] Eric Braaten. *Introduction to the NRQCD Factorization Approach to Heavy Quarkonium*. 1997. arXiv: hep-ph/9702225 [hep-ph]. URL: https://arxiv.org/abs/hep-ph/9702225.

[42] Harald Fritzsch. "Producing heavy quark flavors in hadronic collisions—' A test of quantum chromodynamics". In: *Physics Letters B* 67.2 (1977), pp. 217–221. ISSN: 0370-2693. DOI: https://doi.org/10.1016/0370-2693(77)90108-3. URL: https://www.sciencedirect.com/science/article/pii/0370269377901083.

[43] Yan-Qing Ma and Ramona Vogt. "Quarkonium production in an improved color evaporation model". In: *Phys. Rev. D* 94 (11 Dec. 2016), p. 114029. DOI: 10.1103/PhysRevD.94.114029. URL: https://link.aps.org/doi/10.1103/PhysRevD.94.114029.

[44] M. Krämer. "Quarkonium production at high-energy colliders". In: *Progress in Particle and Nuclear Physics* 47.1 (Jan. 2001), pp. 141–201. ISSN: 0146-6410. DOI: 10.1016/s0146-6410(01)00154-5. URL: http://dx.doi.org/10.1016/S0146-6410(01)00154-5.

[45] "Energy dependence of forward-rapidity J/ψ and $\psi(2\mathrm{S})$ production in pp collisions at the LHC". In: *The European Physical Journal C* 77.6 (June 2017). ISSN: 1434-6052. DOI: 10.1140/epjc/s10052-017-4940-4. URL: http://dx.doi.org/10.1140/epjc/s10052-017-4940-4.

[46] E. G. Ferreiro and C. Pajares. "High multiplicity pp events and J/ψ production at LHC". In: *Physical Review C* 86.3 (Sept. 2012). ISSN: 1089-490X. DOI: 10.1103/physrevc.86.034903. URL: http://dx.doi.org/10.1103/PhysRevC.86.034903.

[47] E. G. Ferreiro and C. Pajares. *Open charm production in high multiplicity proton-proton events at the LHC*. 2015. arXiv: 1501.03381 [hep-ph]. URL: https://arxiv.org/abs/1501.03381.

[48] B. Z. Kopeliovich et al. "J/ψ in high-multiplicity pp collisions: Lessons from pA". In: *Physical Review D* 88.11 (Dec. 2013). ISSN: 1550-2368. DOI: 10.1103/physrevd.88.116002. URL: http://dx.doi.org/10.1103/PhysRevD.88.116002.

[49] A. Andronic et al. "Heavy-flavour and quarkonium production in the LHC era: from proton–proton to heavy-ion collisions". In: *The European Physical Journal C* 76.3 (Feb. 2016). ISSN: 1434-6052. DOI: 10.1140/epjc/s10052-015-3819-5. URL: http://dx.doi.org/10.1140/epjc/s10052-015-3819-5.

[50] Yan-Qing Ma et al. "Event engineering studies for heavy flavor production and hadronization in high multiplicity hadron-hadron and hadron-nucleus collisions". In: *Physical Review D* 98.7 (Oct. 2018). ISSN: 2470-0029. DOI: 10.1103/physrevd.98.074025. URL: http://dx.doi.org/10.1103/PhysRevD.98.074025.

[51] B. Andersson et al. "Parton fragmentation and string dynamics". In: *Physics Reports* 97.2 (1983), pp. 31–145. ISSN: 0370-1573. DOI: https://doi.org/10.1016/0370-1573(83)90080-7.

[52] Christian Bierlich et al. *A comprehensive guide to the physics and usage of PYTHIA 8.3*. 2022. arXiv: 2203.11601 [hep-ph]. URL: https://arxiv.org/abs/2203.11601.

[53] S. G. Weber et al. "Elucidating the multiplicity dependence of J/ψ production in proton–proton collisions with PYTHIA8". In: *The European Physical Journal C* 79.1 (Jan. 2019). ISSN: 1434-6052. DOI: 10.1140/epjc/s10052-018-6531-4. URL: http://dx.doi.org/10.1140/epjc/s10052-018-6531-4.

[54] LEBC-EHS Collaboration. "Comparative properties of 400 GeV/c proton-proton interactions with and without charm production". In: *Zeitschrift für Physik C Particles and Fields* 41.2 (June 1988), pp. 191–196. ISSN: 1431-5858. DOI: 10.1007/BF01566916. URL: https://doi.org/10.1007/BF01566916.

[55] Shreyasi Acharya et al. "Multiplicity-dependent inclusive J/ψ production at forward rapidity in pp collisions at $\sqrt{\mathrm{s}} = \mathbf{13}$ TeV". In: (Apr. 2025). arXiv: 2504.00686 [hep-ex].

[56] Arpad Horvath and Jaybear. *LHC*. Licensed under CC BY-SA 3.0. 2012. URL: https://commons.wikimedia.org/wiki/File:LHC_02.svg (visited on 05/12/2025).

[57] "The ATLAS Experiment at the CERN Large Hadron Collider". In: *JINST* 3 (2008). Also published by CERN Geneva in 2010, S08003. DOI: 10.1088/1748-0221/3/08/S08003. URL: https://cds.cern.ch/record/1129811.

[58] "The CMS experiment at the CERN LHC. The Compact Muon Solenoid experiment". In: *JINST* 3 (2008). Also published by CERN Geneva in 2010, S08004. DOI: 10.1088/1748-0221/3/08/S08004. URL: https://cds.cern.ch/record/1129810.

[59] "The ALICE experiment at the CERN LHC. A Large Ion Collider Experiment". In: *JINST* 3 (2008). Also published by CERN Geneva in 2010, S08002. DOI: 10.1088/1748-0221/3/08/S08002. URL: https://cds.cern.ch/record/1129812.

[60] "The LHCb Detector at the LHC". In: *JINST* 3 (2008). Also published by CERN Geneva in 2010, S08005. DOI: 10.1088/1748-0221/3/08/S08005. URL: https://cds.cern.ch/record/1129809.

[61] "The TOTEM detector at LHC". In: *Nuclear Instruments and Methods in Physics Research Section A: Accelerators, Spectrometers, Detectors and Associated Equipment* 617.1 (2010). 11th Pisa Meeting on Advanced Detectors, pp. 62–66. ISSN: 0168-9002. DOI: https://doi.org/10.1016/j.nima.2009.08.083. URL: https://www.sciencedirect.com/science/article/pii/S0168900209017008.

[62] "The LHCf detector at the CERN Large Hadron Collider". In: *JINST* 3 (2008), S08006. DOI: 10.1088/1748-0221/3/08/S08006. URL: https://cds.cern.ch/record/1129808.

[63] James Pinfold et al. "Technical Design Report of the MoEDAL Experiment". In: (June 2009).

[64] Arturo Tauro. "ALICE Schematics". General Photo. 2017. URL: https://cds.cern.ch/record/2263642.

[65] *Technical Design Report for the Upgrade of the ALICE Inner Tracking System*. Tech. rep. 2014. DOI: 10.1088/0954-3899/41/8/087002. URL: https://cds.cern.ch/record/1625842.

[66] *Upgrade of the ALICE Time Projection Chamber*. Tech. rep. 2013. URL: https://cds.cern.ch/record/1622286.

[67] *ALICE Time-Of-Flight system (TOF): Technical Design Report*. Technical design report. ALICE. Geneva: CERN, 2000. URL: https://cds.cern.ch/record/430132.

[68] Sofia Strazzi. "15 years young: The ALICE TOF detector in the LHC Run 3". In: *Nucl. Instrum. Meth. A* 1077 (2025), p. 170521. DOI: 10.1016/j.nima.2025.170521.

[69] Wladyslaw Henryk Trzaska. "New Fast Interaction Trigger for ALICE". In: *Nuclear Instruments and Methods in Physics Research Section A: Accelerators, Spectrometers, Detectors and Associated Equipment* 845 (2017). Proceedings of the Vienna Conference on Instrumentation 2016, pp. 463–466. ISSN: 0168-9002. DOI: https://doi.org/10.1016/j.nima.2016.06.029. URL: https://www.sciencedirect.com/science/article/pii/S016890021630571X.

[70] David Rohr. *Global Track Reconstruction and Data Compression Strategy in ALICE for LHC Run 3*. 2019. arXiv: 1910.12214 [physics.ins-det]. URL: https://arxiv.org/abs/1910.12214.

[71] ALICE Collaboration et al. "ALICE: Physics Performance Report, Volume II". In: *Journal of Physics G: Nuclear and Particle Physics* 32.10 (Sept. 2006), p. 1295. DOI: 10.1088/0954-3899/32/10/001. URL: https://dx.doi.org/10.1088/0954-3899/32/10/001.

[72] Jubin Mitra et al. "Trigger and timing distributions using the TTC-PON and GBT bridge connection in ALICE for the LHC Run 3 Upgrade". In: *Nuclear Instruments and Methods in Physics Research Section A: Accelerators, Spectrometers, Detectors and Associated Equipment* 922 (Apr. 2019), pp. 119–133. ISSN: 0168-9002. DOI: 10.1016/j.nima.2018.12.076. URL: http://dx.doi.org/10.1016/j.nima.2018.12.076.

[73] Luigi Rolandi, Werner Riegler, and Walter Blum. *Particle Detection with Drift Chambers*. Particle Acceleration and Detection. Springer, 2008. ISBN: 978-3-540-76684-1. DOI: 10.1007/978-3-540-76684-1.

[74] Ivan Vorobyev. "Measurements of (anti)(hyper)nuclei with ALICE". In: *EPJ Web Conf.* 296 (2024), p. 12007. DOI: 10.1051/epjconf/202429612007. URL: https://cds.cern.ch/record/2921165.

[75] ALICE Collaboration. "Multiplicity dependence of charged-particle production in pp, p–Pb, Xe–Xe and Pb–Pb collisions at the LHC". In: *Physics Letters B* 845 (Oct. 2023), p. 138110. ISSN: 0370-2693. DOI: 10.1016/j.physletb.2023.138110. URL: http://dx.doi.org/10.1016/j.physletb.2023.138110.

[76] "The ALICE definition of primary particles". In: (2017). URL: https://cds.cern.ch/record/2270008.

[77] G. D'Agostini. *Improved iterative Bayesian unfolding*. 2010. arXiv: 1010.0632. URL: https://arxiv.org/abs/1010.0632.

[78] Tim Adye. *Unfolding algorithms and tests using RooUnfold*. 2011. arXiv: 1105.1160. URL: https://arxiv.org/abs/1105.1160.

[79] ALICE Collaboration. "Inclusive J/ψ production at midrapidity in pp collisions at $\sqrt{s} = 13$ TeV". In: *The European Physical Journal C* 81.12 (Dec. 2021). ISSN: 1434-6052. DOI: 10.1140/epjc/s10052-021-09873-4. URL: http://dx.doi.org/10.1140/epjc/s10052-021-09873-4.

[80] ALICE Collaboration. "J/ψ production as a function of charged particle multiplicity in pp collisions at $\sqrt{s} = 7$ TeV". In: *Physics Letters B* 712.3 (June 2012), pp. 165–175. ISSN: 0370-2693. DOI: 10.1016/j.physletb.2012.04.052. URL: http://dx.doi.org/10.1016/j.physletb.2012.04.052.

[81] Eugene Levin, Ivan Schmidt, and Marat Siddikov. "ThreePomeronCGC". In: *The European Physical Journal C* 80.6 (June 2020), p. 560. ISSN: 1434-6052. DOI: 10.1140/epjc/s10052-020-8086-4. URL: https://doi.org/10.1140/epjc/s10052-020-8086-4.

[82] K. Werner and B. Guiot. “Perturbative QCD concerning light and heavy flavor in the EPOS4 framework”. In: (2023). arXiv: 2306.02396 [hep-ph]. URL: https://arxiv.org/abs/2306.02396.

[83] K. Werner. “Core-corona procedure and microcanonical hadronization to understand strangeness enhancement in proton-proton and heavy ion collisions in the EPOS4 framework”. In: *Physical Review C* 109.1 (Jan. 2024). ISSN: 2469-9993. DOI: 10.1103/physrevc.109.014910. URL: http://dx.doi.org/10.1103/PhysRevC.109.014910.

[84] Jiaxing Zhao et al. *Heavy flavour hadron production in relativistic heavy ion collisions at RHIC and LHC in EPOS4HQ*. 2024. arXiv: 2401.17096 [hep-ph]. URL: https://arxiv.org/abs/2401.17096.

Declaration of Academic Integrity

I hereby confirm that this thesis, entitled *Multiplicity Dependence of J/ψ Production in pp Collisions at $\sqrt{s} = 13.6$ TeV*, is solely my own work and that I have used no sources or aids other than the ones stated. All passages in my thesis for which other sources, including electronic media and AI tools, have been used, be it direct quotes or content references, have been acknowledged as such and the sources cited. I am aware that plagiarism is considered an act of deception which can result in sanction in accordance with the examination regulations.

I consent having my thesis cross-checked with other texts to identify possible similarities and to having it stored in a database for this purpose.

I confirm that I have not submitted the following thesis in part or whole as an examination paper before.

Münster, 11th July 2025

Alexander Marco Tiekötter